Springer ThesesRecognizing Outstanding Ph.D. Research

Andrés de Bustos Molina

Kinetic Simulations of Ion Transport in Fusion Devices



Springer Theses

Recognizing Outstanding Ph.D. Research

For further volumes: http://www.springer.com/series/8790

Aims and Scope

The series "Springer Theses" brings together a selection of the very best Ph.D. theses from around the world and across the physical sciences. Nominated and endorsed by two recognized specialists, each published volume has been selected for its scientific excellence and the high impact of its contents for the pertinent field of research. For greater accessibility to non-specialists, the published versions include an extended introduction, as well as a foreword by the student's supervisor explaining the special relevance of the work for the field. As a whole, the series will provide a valuable resource both for newcomers to the research fields described, and for other scientists seeking detailed background information on special questions. Finally, it provides an accredited documentation of the valuable contributions made by today's younger generation of scientists.

Theses are accepted into the series by invited nomination only and must fulfill all of the following criteria

- They must be written in good English.
- The topic should fall within the confines of Chemistry, Physics, Earth Sciences, Engineering and related interdisciplinary fields such as Materials, Nanoscience, Chemical Engineering, Complex Systems and Biophysics.
- The work reported in the thesis must represent a significant scientific advance.
- If the thesis includes previously published material, permission to reproduce this must be gained from the respective copyright holder.
- They must have been examined and passed during the 12 months prior to nomination.
- Each thesis should include a foreword by the supervisor outlining the significance of its content.
- The theses should have a clearly defined structure including an introduction accessible to scientists not expert in that particular field.

Andrés de Bustos Molina

Kinetic Simulations of Ion Transport in Fusion Devices

Doctoral Thesis accepted by Universidad Complutense de Madrid, Madrid



Author
Dr. Andrés de Bustos Molina
Tokamaktheorie
Max Planck Institute für Plasmaphysik
Garching bei München
Germany

Supervisors
Dr. Víctor Martín Mayor
Departamento de Fisica Teorica I
Universidad Complutense de Madrid
Madrid
Spain

Dr. Francisco Castejón Magaña Fusion Theory Unit CIEMAT-Euraton Association Madrid Spain

ISSN 2190-5053 ISSN 2190-5061 (electronic) ISBN 978-3-319-00421-1 ISBN 978-3-319-00422-8 (eBook) DOI 10.1007/978-3-319-00422-8

Springer Cham Heidelberg New York Dordrecht London

Library of Congress Control Number: 2013940957

© Springer International Publishing Switzerland 2013

This work is subject to copyright. All rights are reserved by the Publisher, whether the whole or part of the material is concerned, specifically the rights of translation, reprinting, reuse of illustrations, recitation, broadcasting, reproduction on microfilms or in any other physical way, and transmission or information storage and retrieval, electronic adaptation, computer software, or by similar or dissimilar methodology now known or hereafter developed. Exempted from this legal reservation are brief excerpts in connection with reviews or scholarly analysis or material supplied specifically for the purpose of being entered and executed on a computer system, for exclusive use by the purchaser of the work. Duplication of this publication or parts thereof is permitted only under the provisions of the Copyright Law of the Publisher's location, in its current version, and permission for use must always be obtained from Springer. Permissions for use may be obtained through RightsLink at the Copyright Clearance Center. Violations are liable to prosecution under the respective Copyright Law. The use of general descriptive names, registered names, trademarks, service marks, etc. in this publication does not imply, even in the absence of a specific statement, that such names are exempt from the relevant protective laws and regulations and therefore free for general use.

While the advice and information in this book are believed to be true and accurate at the date of publication, neither the authors nor the editors nor the publisher can accept any legal responsibility for any errors or omissions that may be made. The publisher makes no warranty, express or implied, with respect to the material contained herein.

Printed on acid-free paper

Springer is part of Springer Science+Business Media (www.springer.com)

Supervisors' Foreword

This thesis deals with the problem of ion confinement in thermonuclear fusion magnetic confinement devices. It is of general interest to understand via numerical simulations the ion confinement properties in complex geometries, in order to predict their behavior and maximize the performance of future fusion reactors. So this research is inscribed in the effort to develop commercial fusion.

The main work carried out in this thesis is the improvement and exploitation of an existing simulation code called Integrator of Stochastic Differential Equations for Plasmas (ISDEP). This is a Monte Carlo code that solves the so-called ion collisional transport in arbitrary plasma geometry, without any assumption on kinetic energy conservation or on the typical radial excursion of particles, thus allowing the user the introduction of strong electric fields, which can be present in real plasmas, as well as the consideration of nonlocal effects on transport. In this sense, this work improves other existing codes. ISDEP has been used on the two main families of magnetic confinement devices, tokamaks and stellarators. Additionally, it presents outstanding portability and scalability in distributed computing architectures, as Grid or Volunteer Computing.

The main physical results can be divided into two blocks. First, the study of 3D ion transport in ITER is presented. ITER is the largest fusion reactor (under construction) and most of the simulations so far assume axisymmetry of the device. Unfortunately, this symmetry is only an approximation because of the discrete number of magnetic coils. ISDEP has shown, using a simple model of the 3D magnetic field, how the ion confinement is affected by this symmetry breaking. Moreover, ions will have so low collisionality that will be in the *banana regime* in ITER, i.e., a single ion will visit distant plasma regions with different collisionalities and electrostatic potential, which is not taken into account by conventional codes.

Second, ISDEP has been applied successfully to the study of fast ion dynamics in fusion plasmas. The fast ions, with energies much larger than the thermal energy, are result of the heating systems of the device. Thus, a numerical predictive tool is useful to improve the heating efficiency. ISDEP has been combined with the Monte Carlo code FAFNER2 to study such ions in stellarator (TJ-II in Spain and LHD in Japan) and tokamak (ITER) geometries. It has been also

validated with experimental results. In particular, comparisons with the Compact Neutral Particle Analyser (CNPA) diagnostic in the TJ-II stellarator are remarkable.

Madrid, Spain, June 2013

Dr. Francisco Castejón Magaña Dr. Víctor Martín Mayor

Acknowledgments

First, I must thank my supervisors Francisco Castejón Magaña and Víctor Martín Mayor for their time and efforts, and for giving me the opportunity to learn and work with them. Their patience and professionalism have been indispensable for the elaboration of this thesis.

I cannot forget many contributions and suggestions from Luis Antonio Fernández Pérez, José Luis Velasco, Jerónimo García, Masaki Osakabe, Josep Maria Fontdecaba y Maxim Tereshchenko, who were always available for help. I must also thank Tim Happel, Juan Arévalo, Teresa Estrada, Daniel López Bruna, Enrique Ascasíbar, Carlos Hidalgo, José Miguel Reynolds, Ryosuke Seki, José Guasp, José Manuel García Regaña, Alfonso Tarancón, Antonio López Fraguas, Edilberto Sánchez, Iván Calvo, Antonio Gómez, Emilia R. Solano, Bernardo Zurro, Marian Ochando, and many others for many scientific conversations and discussions. I really think that this kind of communication improves the scientific work.

Computer engineers have played a very important role in the results presented in this thesis. I have to mention Rubén Vallés, Guillermo Losilla, David Benito, and Fermín Serrano from BIFI and Rafael Mayo, Manuel A. Rodríguez, and Miguel Cárdenas from CIEMAT.

I must recognize that, although its vintage look and related problems, Building 20 in CIEMAT is a wonderful place to work. My officemates (Risitas, Tim, Coletas, José Manuel, and Labor) have contributed to create a nice work atmosphere, characterized sometimes by an excess of *breaks*. I have very good memories of the people that are or were in the 20: Rosno, Guillermo, David, Yupi, Arturo, el Heavy, Laurita, Dianita, Rubén, Álvaro, Josech, Ángela, Olga, Oleg, Marcos, Beatriz, and some already mentioned.

I also would like to thank my Japanese fellows, in particular to Dr. Masaki Osakabe, for inviting me to work a few weeks with them in their laboratory.

I really like to thank the Free Software Community for providing most of the software tools that I used to develop and execute the simulation code.

Moving to a more personal area, everybody knows that doing a doctorate has good, bad, and very bad moments. The support from family and friends is crucial in these cases. Here the list of people is too long to go into details, but I thank my parents, brother, grandmothers, uncles, aunts, cousins, friends from high school,

viii Acknowledgments

my pitbull friends, the guys from the Music School, people from Uppsala, the *jennies*, and people from 4 K for their help and good mood.

Finally, special thanks to María, for her patience and understanding during the last 2 years.

Andrés de Bustos Molina

Contents

1	Intr	oductio	on	1	
	1.1	1 Preamble			
	1.2	Ion Ti	ransport in Fusion Devices	3	
		1.2.1	Fundamental Concepts	3	
		1.2.2		5	
		1.2.3		7	
		1.2.4	Neoclassical Transport	9	
	1.3	Guidi	ng Center Dynamics	0	
		1.3.1	Movement of the Guiding Center	1	
		1.3.2	Collision Operator	3	
		1.3.3	Stochastic Equations for the Guiding Center	5	
	1.4	Stocha	astic Differential Equations	6	
		1.4.1	A Short Review on Probability Theory	6	
		1.4.2	The Wiener Process	8	
		1.4.3	Stochastic Differential Equations	2	
		1.4.4	Numerical Methods	5	
	Refe	rences		6	
2	ISD	EP		9	
	2.1	Introduction			
	2.2	Descr	iption of the Code	9	
		2.2.1	The Monte Carlo Method	1	
		2.2.2	ISDEP Architecture	3	
		2.2.3	Output Analysis: Jack-Knife Method	5	
		2.2.4	Computing Platforms	7	
		2.2.5	Steady State Calculations	8	
		2.2.6	NBI-Blip Calculations	9	
		2.2.7	Introduction of Non Linear Terms 4	0	
	2.3	Benchmark of the Code			
	2.4	Overview of Previous Physical Results			
		2.4.1	Thermal Ion Transport in TJ-II	5	
		2.4.2	CERC and Ion Confinement	5	
		2.4.3	Violation of Neoclassical Ordering in TJ-II 4	5	

x Contents

	2.4.4	Flux Expansion Divertor Studies	
Re	ferences	*	
3D	Transp	ort in ITER	
3.1	Introd	uction	
3.2	The I	TER Model	
3.3	Nume	rical Results	
	3.3.1	Confinement Time	
	3.3.2	Map of Escaping Particles	
	3.3.3	Outward Fluxes and Velocity Distribution	
	3.3.4	Influence of the Electric Potential	
3.4	Concl	usions	
Re			
		s of Fast Ions in Stellarators	
4.1		rators	
	4.1.1	LHD	
	4.1.2	TJ-II	
4.2	Fast I	ons in Stellarators	
	4.2.1	Ion Initial Conditions	
	4.2.2	Steady State Distribution Function	
	4.2.3	Fast Ion Dynamics: Rotation and Slowing	
		Down Time	
	4.2.4	Escape Distribution and Confinement	
4.3	Comp	arison with Experimental Results	
	4.3.1	Neutral Particle Diagnostics in TJ-II	
	4.3.2	Reconstruction of the CNPA Flux Spectra	
	4.3.3	Neutral Flux and Slowing Down Time	
4.4	Concl	usions	
Re			
		s of NBI Ion Transport in ITER	
5.1		on Initial Distribution	
5.2		on Dynamics in ITER	
	5.2.1	Inversion of the Current	
	5.2.2	Oscillations in <i>E</i>	
5.3		ng Efficiency	
5.4	Concl	usions	
Re	ferences		
		and Conclusions	
Re	ferences		

Contents	xi

Appendix A: Index of Abbreviations	115
Appendix B: Guiding Center Equations	117
Curriculum Vitae	125

Chapter 1 Introduction

1.1 Preamble

Nowadays the planet is experimenting a fast growth in energy consumption and, simultaneously, a reduction in the amount of natural resources, especially in fossil fuels. CO₂ and other greenhouse effect gasses coming from energy activities have deep impact on the environment, leading to the rising climate change that produces global warming among other effects. The development of alternative energy sources becomes necessary for the modern society. Fusion energy is a good candidate to supply a large fraction of the world energy consumption, with the added advantage of being respectful with the environment because radioactive fusion waste has lifetimes much shorter than fission long term radioactive waste. The future fusion reactors are intrinsically safe, and nuclear catastrophes like Chernobyl or Fukushima cannot happen. Thus, research and investments in fusion energy can play a crucial role in the sustainable development.

There are many different fusion processes, but in all of them several light nuclei merge together into heavier and more stable nuclei, releasing energy. The first fusion reaction discovered takes place in the Sun, where Hydrogen fuses into Helium and produces the energy needed to sustain life on Earth. A simplified description of this process is:

$$4H \rightarrow He + 2e^+ + 2\nu_e + 26.7 \,\text{MeV}.$$
 (1.1)

1

The presence of the electron neutrinos indicates that this reaction is ruled by the nuclear weak interaction. Even thought the cross section for this reaction is very small, the gravity forces in the Sun provides the high temperatures and densities that make the reaction possible. Unfortunately, it is very unlikely that this reaction will be reproduced in a laboratory because of the high pressure needed.

On Earth, laboratory fusion research has two different branches: inertial and magnetically confined fusion. The former one consists in compressing a small amount of fuel with lasers resulting in an implosion of the target [1]. The latter constitutes the global frame of this thesis. It is based in heating the fuel at high temperatures and

confine it a sufficient time to produce fusion reactions. At such high temperatures, the fuel (usually Hydrogen isotopes) is in plasma state so the confinement can be done with strong magnetic fields. Many fusion reactions can occur in a magnetically confined plasma. The one with the highest cross section is the Deuterium (D)-Tritium (T) reaction:

$$D + T \rightarrow He + n + 17.6 \,\text{MeV}.$$
 (1.2)

The magnetic field makes the plasma levitate and keeps it away from the inner walls of the machine. In this context we can say that the plasma is confined. Due to the well known *hairy ball theorem* by H. Poincaré, the confining magnetic field should lie in surfaces homeomorphic to thorii. It will be seen that the charged particles tend to follow the magnetic field lines if the magnetic field is strong enough. Then, the plasma tends to remain confined in this torus.

There is a whole area of Physics, called Plasma Physics, that studies the properties of this state of matter. Plasma Physics is a very complicated subject because of its non linear nature and the complexity of the equations involved. Even simple models can be often impossible to be studied analytically and has to be solved numerically. We now briefly recall the main levels of approximation. An accessible introduction to Plasma Physics can be found in Ref. [2] and a recent review in [3]. More advanced texts are Refs. [4, 5].

The first approach to a mathematical model of the plasma is the fluid model. In this model the plasma is considered as a fluid with several charged species. Effects like anisotropy, viscosity, sources and many others can be taken into account. The equations of fluids and electromagnetism have to be solved simultaneously. They form a coupled system of partial differential equations called the Magneto-Hydro-Dynamic (MHD) equations. In particular, most of the computer codes that calculate equilibrium for fusion devices use this approach.

A more detailed and fundamental description is given by the kinetic approach. Here the plasma is described by a distribution function that contains all the information in phase space. Recall that the phase space is the space of all possible states of the system. Usually it is the set of all possible values of position and velocity (or momentum). The main equation in this area is the Drift Kinetic Equation (DKE), a non linear equation in partial derivatives for the plasma distribution function. Once this function is calculated, we can find all the statistical properties of the system. A simplified version of the DKE is solved numerically in this thesis.

We solve the equations with an important purpose in mind because the device performance depends strongly on the dynamics of the plasma. The radial transport, i.e., outward particle and energy fluxes are responsible for particle and heat losses, so fusion devices must be optimized to reduce it as much as possible. Thus, the understanding of kinetic transport in fusion plasmas is a key issue to achieve fusion conditions in a future reliable reactor.

This thesis is focused on the development and exploitation of an ion transport code called ISDEP (Integrator of Stochastic Differential Equations for Plasmas). This code computes the distribution function of a minority population of ions (called test particles) in a fusion device. The exact meaning of *test particles* will be clarified

1.1 Preamble 3

in Sect. 1.3.2. ISDEP takes into account the interaction of the test particles with the magnetic field, the plasma macroscopic electric field and Coulomb collisions with plasma electrons and ions. The main advantage of ISDEP is that it avoids many customary approximations in the so called Neoclassical transport, allowing the detailed study of different physical features.

On the other hand, ISDEP does not deal with any kind of turbulent or non-linear transport. Other simulation codes, like GENE [6], solve the turbulent transport, but are much more complex and expensive in term of computation time.

We will see along this report that ISDEP can contribute to the comprehension and development of Plasma Physics applied to fusion devices. The layout of this thesis is organized as follows: This chapter is an introduction to ion transport in fusion devices, with special emphasis in single particle motion. The ion equations of motion turn to be a set of stochastic differential equations that must be solved numerically. In Chap. 2 the characteristics of the ISDEP code are described, together with a *benchmark* with the MOHR code. Chapters. 3 and 4 explain the numerical results obtained with ISDEP: simulations of 3D transport in ITER, ¹ of fast ions in stellarators² and also in ITER geometry. Finally, Chap. 6 is devoted to the conclusions and future work.

We have included two appendixes in the report: a table with abbreviations (A) and the derivation of the equations of motion (B).

1.2 Ion Transport in Fusion Devices

The scope of this chapter is to recall the physical models that are behind the original results presented in this thesis. We will introduce the notation and coordinates systems used, followed by the steps needed to reach the ion equations of motion using the Guiding Center approximation. It will be seen that this approximation reduces the dimensionality and computing requirements of the problem. We finish with a small introduction to stochastic differential equations and their numerical solution.

Note that this chapter does not intend to be a complete and self-contained review on the topic because Plasma Physics is a very wide and multidisciplinary science. In many cases we will summarize the main results and refer to articles or textbooks for further reading.

1.2.1 Fundamental Concepts

In this section we remind the basic concepts of magnetically confined plasmas. In a magnetized plasma one or several ion species coexist with electrons and a small

¹ ITER is an experimental fusion device in construction, see Chap. 3.

² Stellarators are a family of fusion devices, see Chap. 4.

amount of impurities and neutral atoms. Usually the ion species are light nuclei, like Hydrogen, Deuterium, Tritium or Helium. Globally the plasma has zero electric charge, but locally it may be charged and create an electric field. The dynamic of the plasma is strongly correlated with this electric field, and usually it induces a poloidal rotation (see Sect. 1.3) and enhances the confinement.

We always assume that the magnetic force dominates the dynamics and that the magnetic field time independent, or at least that time variations are slow compared with the test particle lifetime. The last assumption is valid when the electric currents in the plasma do not change in time very much. By strong magnetic field we mean that it dominates the movement of charged particles in the fusion device. We will deal with magnetic fields, **B**, of order 1–6 T.

It is important to remark that in fusion science there are mainly two families of experimental devices: **tokamaks** and **stellarators**. Tokamaks are approximately axysimmetric devices where the magnetic field is created by external coils and the plasma itself. A very intense plasma current is induced with a central solenoid, creating around 10–20% of the total magnetic field. On the other hand, stellarators are 3D complex devices where the magnetic field is completely external. Tokamaks are generally more advanced than stellarators, both from the Physics and Engineering points of view, but stellarators are much more stable and suitable for a future steady state operation. In Fig. 1.1 we sketch these two devices, and in Sects. 3.1 and 4.1 we explain their characteristics in more detail.

Most of the fusion devices, especially stellarators, allow for a variation of the current in the coils. Therefore, the same machine can have quite different plasmas depending on the magnetic field created by the coils. We will name this set of coil parameters as **magnetic configuration**. All plasma transport properties rely strongly on the magnetic configuration of the machine.

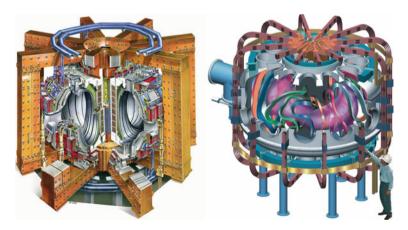


Fig. 1.1 Examples of tokamak (*left*) and stellarator (*right*). The tokamak usually presents rotation symmetry, while the stellarators are always 3D. Since the Physics and Engineering of tokamaks are simpler, tokamaks are more advanced than stellarators

Most of the ion population in the plasma compose the bulk. The bulk is the core of the plasma and in many situations it can be described by the MHD equations. Impurities, neutral atoms and supra-thermal ions and electrons are also present in the plasma, but in smaller quantities. Despite these low concentrations, they can affect the confinement properties and the global plasma parameters. The impurities are caused by the interaction of the plasma with the walls and other objects inside the vacuum vessel of the device. Plasma ions have energies that range from hundreds of eV in middle size devices to keV in large machines, so when an ion hits the wall it sputters several wall atoms which may become part of the plasma. Since the impurities are usually very heavy, they cause the plasma to cool down by radiation, affect the transport parameters and then set aside from fusion conditions. Some devices are equipped with a divertor to diminish the plasma wall interaction and hence the impurity presence and to prevent wall damage. A divertor is a system that concentrates the particle losses in a region of the vacuum vessel and minimizes the impurity disengaging [7]. It is clear then that a study of the ion loss distribution can play an important role in the design of a fusion device.

Suprathermal ions (also called fast ions in this thesis) have much more energy than bulk ions and are produced by the heating systems of the device and, in the future, by fusion reactions. Physically, they usually behave in a different way than thermal ions. The basic understanding of fast particle transport in the plasma is necessary to improve the efficiency of the heating systems and their effects on the plasma confinement. Moreover, a future self-sustained fusion reaction will rely on the production and confinement of α particles, which behave similarly to the fast ions. In this thesis we will deal with a heating system called Neutral Beam Injection (NBI). NBI ions are high energy ions that deliver their energy to the plasma by collisions with other ions and electrons, heating and fueling the plasma bulk.

1.2.2 Geometrical Considerations

We shall work with several coordinate systems depending on the geometry of the confining device. Cartesian and cylindrical coordinates are widely used, as well as toroidal coordinates. Figure 1.2 (left) shows the convention for the two angles of the toroidal coordinates.

Additionally to these coordinates there are several specific coordinate systems for magnetically confined plasmas, called magnetic coordinates [8]. As examples, Boozer and Hamada coordinates are magnetic coordinates commonly used in the plasma literature. Many plasma equations have a simple form in magnetic coordinates, but they have a serious limitation: they are only well defined when the magnetic field forms a set of nested toroidal surfaces and there are no magnetic islands or ergodic volumes. This topological restriction limits the application of magnetic coordinates.

In particular, a very important magnetic coordinate is the effective radius. The effective radius, usually denoted by ρ , is a reparametrization of the toroidal magnetic

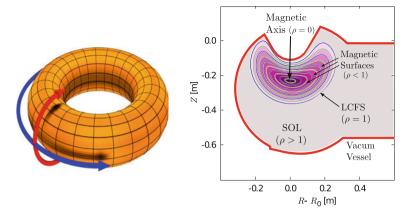


Fig. 1.2 (*Left*) Toroidal coordinate system: poloidal (*red*) and toroidal (*blue*) directions. *Source www.wikipedia.org*. (*Right*) Different regions of a fusion device: magnetic axis, magnetic surfaces, Last Closed Flux Surface (LCFS) and Scrape-Off-Layer (SOL) for TJ-II. The surface integral in Eq. 1.3 is limited by the magnetic surfaces (in pink color-scale)

flux and plays an important role in the symmetry of the plasma equilibrium. Defining the toroidal flux as:

$$\Psi = \int d\mathbf{S}_{\varphi} \cdot \mathbf{B},\tag{1.3}$$

where φ is the toroidal angle, **B** the magnetic field and the integration takes place in a toroidal cross section of the plasma. The integration limits are determined by the magnetic surfaces in a toroidal cut (see Fig. 1.2, right). Then, the effective radius is defined as:

$$\rho = \sqrt{\frac{\Psi}{\Psi_{\text{LCFS}}}},\tag{1.4}$$

where Ψ_{LCFS} is the magnetic flux at the Last Closed Flux Surface (LCFS). It can be shown that the effective radius labels correctly the magnetic surfaces of the device. The effective radius varies from 0 to 1, although it is necessary to extrapolate it to describe the region in between the plasma and the vacuum vessel, called Scrape-Off-Layer (SOL). The boundary between the plasma and the SOL is the LCFS and corresponds to $\rho=1$. Places with $\rho>1$ have open magnetic field lines and the magnetic surfaces intersect the vacuum vessel of the device in some points. Figure 1.2 (right) shows these regions in a toroidal cut of a TJ- Π^3 plasma.

Particle transport presents two well separate timescales according to the movement in a magnetic surface: fast dynamics on the surface, and slow perpendicular transport between two magnetic surfaces. In a first approximation, we shall treat the transport tangent to a magnetic surface as infinitely fast. Thus, in this approximation, the

³ TJ-II is an experimental device built at CIEMAT, see Sect. 4.1.2.

plasma is uniform at each surface and quantities like temperature, density, pressure and electric potential will depend only on the effective radius ρ and are called *flux quantities*. More detailed studies may require poloidal and toroidal asymmetries on the plasma equilibrium profiles, but they are out of the scope of this work.

The last quantity that we introduce in this section is the safety factor q or its inverse, called rotational transform: $\iota = q^{-1}$. They give a measure of the twist of the magnetic field lines [1, 6] and play a crucial role in plasma equilibrium criteria. The safety factor q is defined as the average quotient between the poloidal and toroidal angles turned by the field line:

$$q = \left\langle \frac{\mathrm{d}\varphi}{\mathrm{d}\theta} \right\rangle, \quad \iota = \left\langle \frac{\mathrm{d}\theta}{\mathrm{d}\varphi} \right\rangle.$$
 (1.5)

The average is taken on a magnetic surface, so q and ι are flux quantities. The factor q is generally used in tokamak like devices while ι is reserved for stellarators. The principal significance of q is that if $q \leq 2$ at the plasma edge, the plasma is MHD unstable [6]. Rational values of q imply that the field lines would closed in a particular magnetic surface and instabilities and resonances may arise [6]. Resonances modify the magnetic topology and can facilitate the appearance of islands or ergodic volumes in their neighborhood.

1.2.3 The Distribution Function

In this subsection we remind the concept of distribution function [9] and we introduce the notation used along this thesis report. The distribution function is the most important concept in statistical mechanics because it contains all the physical information of the system. We will denote it by $f(\mathbf{x}, t)$, where t is the time and \mathbf{x} are the coordinates in the p-dimensional phase space. For instance, the phase space of a single particle is, in general, $\mathbf{x} = (x, y, z, v_x, v_y, v_z)$. In Sect. 1.3 we will reduce the dimensions of this space to 5. Additionally, we may deal with 1D phase spaces, like the energy distribution function, denoted by f(t, E).

The distribution function represents the number of particles per unit volume in phase space that are located in the surroundings of the point \mathbf{x} at time t. It is usually normalized as follows:

$$N(t) = \int f(\mathbf{x}, t) \cdot J(\mathbf{x}) \cdot d\mathbf{x}, \qquad (1.6)$$

where $J(\mathbf{x})$ is the Jacobian of the coordinate system and N the total number of particles of the system. One can find the average of any magnitude $A(t, \mathbf{x})$ of the system using f:

$$\langle A(t) \rangle = \frac{1}{N(t)} \int d\mathbf{x} f(\mathbf{x}, t) J(\mathbf{x}) A(t, \mathbf{x}). \tag{1.7}$$

We can find the velocity and the average kinetic energy using the first and the second moments of the distribution:

$$\langle \mathbf{v}(t) \rangle = \frac{1}{N(t)} \int d\mathbf{x} f(\mathbf{x}, t) J(\mathbf{x}) \mathbf{v}. \tag{1.8}$$

$$\langle E(t) \rangle = \frac{1}{N(t)} \int d\mathbf{x} f(\mathbf{x}, t) J(\mathbf{x}) \frac{mv^2}{2}.$$
 (1.9)

One of the main results of this thesis is the explicit calculation of the distribution function of a minority population of particles in a fusion plasma (see Chap. 4). We will not calculate the whole distribution function because it is very expensive in terms of CPU time: we will compute a marginal distribution function. This means that we integrate in one or more coordinates in phase space, losing information but reducing the number of calculations needed.⁴

A very important instance is the Maxwell-Boltzmann distribution, denoted by f_M . In terms of the particle energy E and density n it is expressed as:

$$f_M(E) = \frac{n}{T} \sqrt{\frac{E}{\pi T}} e^{\left(-\frac{E}{T}\right)}.$$
 (1.11)

Note that T is the system temperature measured in energy units. This distribution is very important in Physics and in particular in Plasma Kinetic Theory. We often assume that the confined plasma is locally Maxwellian, in the sense that the v^2 dependence is ruled by f_M , according to the temperature at each point in the space.

There is a useful quantity, called the Binder cumulant, which measures deviations of any distribution function from f_M . It is defined as:

$$\kappa = \frac{\langle v^4 \rangle}{\langle v^2 \rangle^2}.\tag{1.12}$$

It is straightforward to show that for a Maxwellian distribution we have $\kappa_M = 5/3$. The Binder cumulant is useful to obtain a criterium for the amount of suprathermal particles in a system. If we find that our system has $\kappa < \kappa_M$, it indicates that we have a lack of suprathermal particles, referred to the temperature of Eq. 1.11; while if $\kappa > \kappa_M$ we have a surplus.

$$f(t, x_1) = \int dx_2 dx_3 J(x_2, x_3) f(t, x_1, x_2, x_3).$$
 (1.10)

⁴ For example, in a 3D phase space:

1.2.4 Neoclassical Transport

Neoclassical (NC) transport [2, 10, 17] is a linear theory which models the transport of particles, momentum and energy in a magnetized plasma under several assumptions. NC theory is a basic transport theory used in fusion science and many fusion devices are optimized according to its predictions. Unfortunately it presents several major limitations: it does not consider any turbulent effects, has restrictions in the particle orbit shape and assumes the conservation of the kinetic energy for a single particle. In many situations turbulence dominates the transport and the NC theory is not appropriate anymore (i.e., the NC ordering is violated). In these cases NC theory only provides a lower bound of the total plasma transport.⁵

The goal of Neoclassical transport is to write and solve a closed set of equations for the time evolution of the firsts moments of the distribution function of each plasma specie: particle density; particle and energy fluxes; pressure and stress tensors. Neoclassical transport takes into account the real 3D geometry of the plasma, particle drifts due to the complex magnetic and electrostatic fields and it is valid for all collisionality regimes (although some minimum level of collisionality must be satisfied).

Neoclassical theory assumes a small deviation from the Maxwellianity in the plasma distribution, a geometry composed of fixed nested magnetic geometry, static plasma (or quasi-static), locality in the transport coefficients and Markovianity in the particle motion. Only binary collisions between particles are considered, and all complex collective aspects of the plasma are disregarded. As a result, all processes considered are radially local, i.e., the plasma quantities depend only on the effective radius and NC theory is diffusive.

This model is the basis of plasma transport and it is accurate in several plasma regimes, leading to predictions that have been confirmed experimentally, like the Bootstrap current [13] or the ambipolar radial electric field. On the other hand, in certain circumstances experimental values of the plasma transport parameters can exceed neoclassical estimates by an order of magnitude or more.

In many situations, like turbulent regimes, devices with large radial particle excursions, time dependent magnetic field or strong radial electric field, the Neoclassical theory is not appropriate to describe the system. However, even if they are not dominant, the mechanisms of Neoclassical transport are always present and should be studied and understood.

In particular, we will apply the ISDEP code (see Chap. 2) in two situations where the NC theory can be inappropriate: thermal transport in ITER and fast ion dynamics. In both cases the test particle may present wide orbits and violate the NC ordering, so a more complete model becomes necessary.

⁵ The most promising theory to explain turbulence in plasmas is the Gyrokinetic Theory [12].

1.3 Guiding Center Dynamics

In this section we review the reduction of the equations of movement of a charged particle in a strong magnetic field. This common procedure in Plasma Physics is called the Guiding Center (GC) approximation and is very useful in the conditions of most fusion devices. There are several textbooks where this theory is developed and applied to Plasma Physics: [2, 3, 10].

In the GC paradigm the movement of a charged particle in a magnetic field may be divided into the fast gyration around a magnetic field line and the movement of the gyration center. This situation is sketched in Fig. 1.3. If the gyroradius, i.e., the Larmor radius, is much smaller than any other characteristic length of the system, an average in the gyromotion can simplify substantially the dynamics of the particle. The phase space is reduced from 6 to 5 dimensions and the gyromotion, a small scale and high frequency motion, disappears. Usually the ion Larmor radius in fusion devices is $r_L \sim 1$ mm for bulk particles, much smaller than any other characteristic length. On the whole, the GC approximation can be trusted in most situations concerning fusion plasmas.

This approximation reduces the 6D phase space of a single particle to a 5D space and eliminates a high frequency and short scale movement, making the numerical integration of the particle trajectories much easier and less expensive in terms of computational resources. The disadvantage of this approximation is that the equations of movement become more complex than the standard Lorentz force, involving spatial derivatives of the magnetic field.

The basic idea is to divide the particle movement in parallel movement along the **B** line and the perpendicular drift. Ignoring the rotation of the particle, also called gyromotion, its velocity has two components: $\mathbf{v} = \mathbf{v}_{||} + \mathbf{v}_{D}$, parallel and

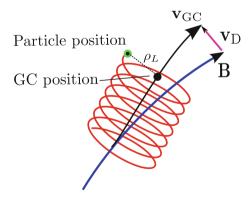


Fig. 1.3 The GC approximation substitutes the helical movement of a charged particle around a magnetic field line for the movement of the center of this helix, the guiding center. The GC velocity is mostly parallel to the magnetic field but there is a non zero perpendicular velocity responsible for particle drifts, due to inhomogeneities of the magnetic field or the presence of a small electric field. The vector \mathbf{v}_D is over-sized in the drawing, usually $v_D/v_{GC} \ll 1$

perpendicular to the magnetic field. The drift velocity \mathbf{v}_D is usually smaller than $\mathbf{v}_{||}$ by two orders of magnitude or more and it depends on the macroscopic electric field and inhomogeneities in the magnetic field. Figure 1.3 shows schematically the GC approximation.

There are several GC coordinates but all of them refer to a 3D point in position space, the GC position, and reduce the velocity space from 3D to 2D. The most common coordinate systems are (x, y, z, v^2, λ) and $(x, y, z, v_{||}, v_{\perp})$. The vector (x, y, z) is the position of the GC; v^2 is the normalized kinetic energy; λ is the pitch, defined as $\lambda = \mathbf{v} \cdot \mathbf{B}/vB$; and $v_{||}$ and v_{\perp} are the parallel and perpendicular components of the velocity referred to the magnetic field. In the GC frame the perpendicular component v_{\perp} is a positive number because we are ignoring the gyromotion.

In the subsequent sections we will describe the GC equations of motion for a single particle. When collisions are included, the final expression is a set of five coupled stochastic differential equations [14] for the GC coordinates. In Sect. 1.4 the main characteristics of this family of equations are shown. As a first approach, a stochastic differential equation (SDE) is denoted as:

$$dx^{i} = F^{i}(x, t) dt + G^{i}_{j}(x, t) dW^{j}, \quad i, j = (x, y, z, v^{2}, \lambda).$$
 (1.13)

Note that we use the Einstein summation convention all along this report.⁶ The motion due to the magnetic configuration, electric fields and the geometry of the plasma are included in the tensor F^i . The effect of the collisions is naturally divided into a deterministic part in F^{v^2} , F^{λ} and a stochastic part in G^{ij} ($i, j = v^2, \lambda$). The stochastic differentials dW^j are random numbers responsible for diffusion in velocity space. In the collision operator used in ISDEP, G^{ij} is diagonal in (v^2, λ) -space: $G^{v^2\lambda} = G^{\lambda v^2} = 0$.

The GC equations can be divided into two groups according to their physical sense. A first group concerning the movement of a charged particle in an electromagnetic field is discussed in Sect. 1.3.1 and Appendix B. The second group is related to the interaction of the test particle with the plasma background (Sect. 1.3.2).

1.3.1 Movement of the Guiding Center

In this section we merely indicate the procedure to apply the GC approximation to the movement of a charged particle and show the final equations. The deduction of those equations can be found in the Appendix B.

The reduction of the dimensionality of the system is done in two steps:

⁶ When an index variable appears twice (as a subscript and a superscript) in the same expression it implies that we are summing over all of its possible values. For instance: $a^ib_i = \sum_i a^ib_i$. Partial derivatives are denoted by a comma: $f(\mathbf{x})_{,i} = \partial f(\mathbf{x})/\partial x^i$. See [1] for the covariant and contravariant character of the tensors.

1. First, we separate, the particle movement in the GC movement and the fast gyration around a **B** field line: $\mathbf{x} = \mathbf{X}_{GC} + \vec{\rho}$. The vector $\vec{\rho}$ is perpendicular to **B** and has length equal to the particle Larmor radius. We must expand in Taylor series any field or quantity, using the Larmor radius as parameter.

2. Then we average all expanded quantities in the gyroangle:

$$\langle A \rangle = \frac{1}{2\pi} \int A(\theta, \ldots) d\theta.$$
 (1.14)

The final differential equations for the GC position \mathbf{X} are much more complicated than the classical Lorentz force, but the spatial and time scales of the solution are much larger, reducing computational costs; and the phase space dimension is reduced by one. The GC evolution is divided into parallel and perpendicular to the magnetic field. The perpendicular velocity is generally called drift velocity \mathbf{v}_D .

We write below the general form of the GC equations, used for tokamaks, in $(\mathbf{r}, v^2, \lambda)$ coordinates. Since in stellarators the magnetic field satisfies $\nabla \times \mathbf{B} = \vec{0}$, the GC equations admit some further simplification. Table 1.1 shows the notation used in this thesis for the different physical quantities.

$$\frac{\mathrm{d}\mathbf{r}}{\mathrm{d}t} = v\lambda \frac{\mathbf{B}}{B} + \frac{mv^2(1-\lambda^2)}{eB^3} \left(\mathbf{B} \cdot (\nabla \times \hat{\mathbf{b}}) \right) \cdot \mathbf{B} + \mathbf{v}_D = \mathbf{v}. \tag{1.15}$$

$$\mathbf{v}_{D} = \frac{\mathbf{E} \times \mathbf{B}}{B^{2}} + \frac{mv^{2}}{2eB^{3}}(1 - \lambda^{2})\left(\mathbf{B} \times \nabla B\right) + \frac{mv^{2}\lambda^{2}}{eB^{2}}\left(\frac{\mathbf{B} \times \mathbf{R}_{c}}{R_{c}^{2}}\right). \tag{1.16}$$

$$\frac{\mathrm{d}v^2}{\mathrm{d}t} = -\frac{2e}{m}\frac{\mathrm{d}\Phi}{\mathrm{d}t} = -\frac{2e}{m}\left(\nabla\Phi\frac{\mathrm{d}\mathbf{r}}{\mathrm{d}t}\right) = \frac{2e}{m}\mathbf{E}\cdot\mathbf{v}.$$
(1.17)

$$\frac{\mathrm{d}\lambda}{\mathrm{d}t} = \frac{1 - \lambda^2}{2} \left(\frac{2e}{mv} E_{||} - \frac{\lambda}{B^3} \mathbf{E} \cdot (\mathbf{B} \times \nabla B) + \frac{2\lambda}{B^2} \mathbf{E} \cdot \left(\frac{\mathbf{B} \times \mathbf{R}_c}{R_c^2} \right) \right)$$

$$-\frac{v}{B}(\nabla B)_{||} - \frac{m\lambda v^2}{eB^3} \nabla B \left(\frac{\mathbf{B} \times \mathbf{R}_c}{R_c^2} \right) \right). \tag{1.18}$$

Table 1.1	l Notation o	of the physica	I quantities in the	e equations of motion
-----------	--------------	----------------	---------------------	-----------------------

r	Guiding center position	ρ	Effective radius
v	GC velocity, normalized to c	m	Proton mass
λ	Particle pitch = $\mathbf{v} \cdot \mathbf{B}/vB$	c	Speed of light
v^2	Particle velocity square	e	Elementary charge
\mathbf{v}_{D}	GC drift velocity	V, \mathbf{E}	Plasma potential and electric field
$\mathbf{v}_{ }$	GC parallel velocity	n	Plasma density
В	Confining magnetic field	T_i, T_e	Ion and electron temperatures
\mathbf{R}_c	Curvature radius of B	v_{th}	Ion Thermal velocity

1.3.2 Collision Operator

A collision operator is the RHS of the continuity equation in phase space for the distribution function. Assuming binary collisions and neglecting two-body correlations this equation is named Boltzmann equation [9]. The Boltzmann equation is valid to describe plasmas because the density is very low ($n \sim 10^{-19} \, \mathrm{m}^{-3}$) and there is a strong Debye screening. Mathematically:

$$\frac{\partial f}{\partial t} + v \frac{\partial f}{\partial x} + \dot{v} \frac{\partial f}{\partial v} = \frac{\partial f}{\partial t}|_{coll} = C(f). \tag{1.19}$$

Generally the collision operator C(f) is an integro-differential operator, highly non linear in f, and very difficult to deal with. The collision operator used in ISDEP is a linearization of the Landau collision operator for pitch angle and energy scattering. Linearization means that the whole system function is divided into a known fixed background distribution and an unknown test particle population, which is the subjet of study:

$$f = f_{BG} + f_{test}. (1.20)$$

In is assumed that the number of particles in the background is much larger than the test particle number and that the background is stationary and not modified at all by f_{test} . In this way C(f) becomes simpler because it only depends of the test particle speed and the background temperature and density.

Under the test particle approximation, the Boltzmann equation becomes a Fokker-Planck equation that can be transformed into a Langevin or SDEs set. Thus the operator C(f) is used in the stochastic differential Eq. 1.13 describing the interaction of a test particle with the background plasma. First, Boozer and Kuo-Petravic found this collision operator for the GC [15] for one plasma species. Later, Chen [16] extended this operator for several plasma species allowing a more realistic implementation of the collisional processes.

In this report we only show the final equations of the collision operator, referring to the bibliography for the derivation. The main features of C(f) are:

- It assumes a locally Maxwellian distribution for all background species.
- There are only collisions of test particles with background plasma, without collisions between test particles. This is a very important characteristic for the performance of ISDEP in distributed computing platforms.
- The test particle suffers pitch angle and velocity diffusion, so thermalization and deflection are allowed.
- We assume that the effect of the collisions is small, i.e., there are many particles inside the Debye sphere and the electromagnetic interaction is strongly shielded.
- C(f) is a linear operator. Thus there is no global conservation of energy and momentum because the plasma background is not modified by the test particles.
 In other words, the background plasma is a thermal bath with infinite specific heat.

Now we present the explicit form of C(f). Let b = e, i, referring to the plasma background ions and electrons. It is necessary to introduce the notation:

$$\Phi(x) = \int_0^x dy \frac{2}{\sqrt{\pi}} e^{-y^2}, \quad \Psi(x) = \frac{\Phi(x) - x\Phi'(x)}{2x^2}, \quad (1.21)$$

$$\mathbf{x}_b = v/v_{th}(b). \tag{1.22}$$

Usually $\Phi(x)$ is called the error function. The factor x_b is the ratio of the test particle speed and the thermal speed of the plasma particle b. Usually b stands for background electrons and protons, but it can be any other ion or heavy impurity. We shall need as well of the Braginskii deflection and energy slowing down frequencies for ions and electrons. In the following expressions the plasma background profiles n, T_e and T_i are measured in units of m^{-3} and eV, the particle mass m is in kg and all the frequencies in s^{-1} , respectively.

$$\nu_{\rm B}(e) = \frac{4}{3} \sqrt{\frac{2\pi}{m_e}} \frac{e^4 n \ln \Lambda}{T_e^{\frac{3}{2}}}, \qquad \nu_{\rm B}(i) = \frac{4}{3} \sqrt{\frac{\pi}{m_i}} \frac{e^4 n \ln \Lambda}{T_i^{\frac{3}{2}}}, \tag{1.23}$$

$$\nu_d(i) = \frac{3}{2} \sqrt{\frac{\pi}{2}} \nu_{\rm B}(i) \frac{\Phi(x_i) - \Psi(x_i)}{x_i^3}, \qquad \nu_E(i) = 3 \sqrt{\frac{\pi}{2}} \nu_{\rm B}(i) \frac{\Psi(x_i)}{x_i}, \tag{1.24}$$

$$\nu_d(e) = \frac{3}{4} \sqrt{\pi} \nu_{\rm B}(e) \frac{m_e^2}{m_i^2} \frac{\Phi(x_e) - \Psi(x_e)}{x_e^3}, \qquad \nu_E(e) = \frac{3}{2} \sqrt{\pi} \nu_{\rm B}(e) \frac{m_i}{m_e} \frac{\Psi(x_e)}{x_e},$$
(1.25)

where $\ln \Lambda$ is the Coulomb logarithm for ions:

$$\ln \Lambda = \ln \frac{3}{2} \frac{1}{\sqrt{\pi n} e^3} T_i^{3/2}.$$
 (1.26)

The Coulomb logarithm is a slow varying quantity, with typical values of 15–25 in fusion plasmas. Then the collision part in the Fokker-Planck equation is:

$$C(f) = \sum_{b} \frac{\nu_d(b)}{2} \frac{\partial}{\partial \lambda} \left((1 - \lambda^2) \frac{\partial f}{\partial \lambda} \right) + \sum_{b} 2 \frac{\partial}{\partial v^2} \left(v^2 \nu_E(b) \left(f + v v_{\text{th}}^2 \frac{\partial}{\partial v^2} \left(\frac{f}{v} \right) \right) \right), \tag{1.27}$$

where the index *b* labels all plasma background species. Considering the equivalence between FP and Langevin equations (using Itô's algebra, see Sect. 2.2.1):

$$\frac{\partial f}{\partial t} = -(F^{\mu}f)_{,\mu} + \frac{1}{2}(G^{\mu}_{\eta}G^{\eta\nu}f)_{,\mu\nu}, \qquad (1.28)$$

$$\mathrm{d}x^{\mu} = F^{\mu}\mathrm{d}t + G^{\mu}_{\nu}\mathrm{d}W^{\nu},\tag{1.29}$$

and identifying terms, F and G become:

$$F_{v^2} = -\sum_b \nu_E(b) \left(x_i^2 - \frac{x_b}{\sqrt{\pi}} \frac{e^{-x_b^2}}{\Psi(x_b)} \frac{T_b}{T_i} \right), \quad F_{\lambda} = -\sum_b \lambda \nu_d(b), \quad (1.30)$$

$$G_{v^2v^2} = 2x_i \sqrt{\sum_b v_E(b) \frac{T_b}{T_i}}, \qquad G_{\lambda\lambda} = \sqrt{\sum_b (1 - \lambda^2) v_d(b)}.$$
 (1.31)

Most of these formulas have been taken from [16]. Information about the momentum conservation can be found in [18]. The collision frequencies are functions of the plasma background temperature and density and, as a result, they only depend on the effective radius (see Eq. 1.4) and are uniform in a magnetic surface.

1.3.3 Stochastic Equations for the Guiding Center

Writing together the results from Sects. 1.3.1 and 1.3.2, the general Langevin equations for a test particle moving in a static background plasma are:

$$d\mathbf{r} = (\mathbf{v}_{||} + \mathbf{v}_{D}) dt, \qquad (1.32)$$

$$\mathbf{v}_{||} = v\lambda \frac{\mathbf{B}}{B} + \frac{mv^{2}c^{2}(1 - \lambda^{2})}{eB^{3}} \mathbf{B} \cdot \left(\nabla \times \frac{\mathbf{B}}{B}\right) \mathbf{B}, \qquad (1.33)$$

$$\mathbf{v}_{D} = \frac{mv^{2}c^{2}(1 - \lambda^{2})}{2eB^{3}} \mathbf{B} \times \nabla B + \frac{\mathbf{E} \times \mathbf{B}}{B^{2}} + \frac{mv^{2}c^{2}\lambda^{2}}{eB^{3}} \left(\frac{\mathbf{B} \times \mathbf{R}_{c}}{R_{c}^{2}}\right), \qquad (1.34)$$

$$dv^{2} = \left(\frac{2e}{m}(\mathbf{E} \cdot \mathbf{v}_{D}) - \sum_{b} v_{E}(b) \left(x_{i}^{2} - \frac{x_{b}}{\sqrt{\pi}} \frac{e^{-x_{b}^{2}}}{\Psi(x_{b})} \frac{T_{b}}{T_{i}}\right)\right) dt$$

$$+ 2x_{i} \sqrt{\sum_{b} v_{E}(b) \frac{T_{b}}{T_{i}}} dW^{v^{2}}, \qquad (1.35)$$

$$d\lambda = \left(\frac{1 - \lambda^{2}}{2} \left(\frac{2ev_{||}}{mv^{3}} \mathbf{E} \cdot \mathbf{v}_{||} - \frac{\lambda}{B^{3}} \mathbf{E} \cdot (\mathbf{B} \times \nabla B)\right)$$

$$+ \frac{2}{B^{3}} \mathbf{E} \cdot \left(\frac{\mathbf{B} \times \mathbf{R}_{c}}{R^{2}}\right)\right)$$

$$-\frac{v_{||}}{vB}\nabla B \cdot \mathbf{v}_{||} - \frac{m\lambda v^{2}}{eB^{3}}\nabla B \cdot \left(\frac{\mathbf{B} \times \mathbf{R}_{c}}{R_{c}^{2}}\right) dt$$
$$-\sum_{b} \lambda v_{d}(b)dt + \sqrt{\sum_{b} (1 - \lambda^{2})v_{d}(b)} dW^{\lambda}, \tag{1.36}$$

where the frequencies v_d and v_E depend only on the background plasma composition and the test particle energy (see Table 1.1 for the notation used). They form a set of 5 coupled stochastic differential equations with two Wiener processes. For a stellarator geometry, these equations are simplified setting $\nabla \times \mathbf{B} = \vec{0}$. A short overview on stochastic differential equations and numerical methods to solve them can be found in Sect. 1.4.

1.4 Stochastic Differential Equations

In this section we introduce briefly the stochastic analysis applied to fusion plasmas. This in necessary to obtain numerical solutions of the stochastic equations from previous sections. We will deal with equations with random variables that represent the diffusion processes that take place in the plasma. A simple numerical scheme in 1D that represents diffusion is the following.

Consider the time parameter $t \in [0, 1]$ and the time discretization as $t_n = n/N = n\epsilon$, $\epsilon = 1/N$, with n = 0, ..., N. The model for the evolution of the position x_n includes a deterministic force, represented by F(x, t) and a diffusion term, denoted by G(x, t):

$$x_{n+1} = x_n + F(x_n, t_n)\epsilon + G(x_n, t_n)\sqrt{\epsilon}\,\eta,\tag{1.37}$$

where η is a random number with normal distribution (see Sect. 1.4.1). We will sketch in this section what happens when $\epsilon \to 0$ and Eq. (1.37) becomes a Stochastic Differential Equation:

$$dx = F(x, t)dt + B(x, t)dW. \tag{1.38}$$

We will formalize the stochastic factor dW, called the Wiener process, and remind mathematical and numerical tools to manage this kind of equations. A general and rigorous review on this topic can be found in [14] and in [19].

We start with the basic definitions of probability theory, followed by the Stochastic Differential Equations (SDE) basic notions and ending with numerical techniques to solve them.

1.4.1 A Short Review on Probability Theory

Let us very briefly recall some basic concepts of probability theory. The triplet $(\Omega, \mathcal{U}, \mathcal{P})$ is called a probability space, where Ω is an arbitrary set, \mathcal{U} is a σ -algebra

of Ω and $\mathcal{P}: \mathcal{U} \to [0, 1]$ is a probability measure. The sets $A \in \mathcal{U}$ are called events and are the subsets of Ω with a defined probability. The probability measure is a measure with the following normalization constrain: $\mathcal{P}(\Omega) = 1$.

A random variable is a map of the set Ω in the real space: $\mathbf{X}: \Omega \to \mathbb{R}^n$. When a collection of random variables depend on a real parameter $t \geq 0$, then $\mathbf{X}(t)$ is called a stochastic process in which t plays the role of time. As an example, in plasma kinetic theory, the σ -algebra \mathcal{U} can be the set of all possible open sets of the 5D coordinate space of the test particle. Imagine a particle moving in this phase space. Let us formulate it in plain words: if the question what is the probability of the particle to be inside certain hypercube in phase space? has an answer for all times, the trajectory of the particle is a stochastic process.

The distribution and density functions are two fundamental concepts in probability theory and statistical mechanics. The distribution function of the random variable \mathbf{X} is a function $F: \mathbb{R}^n \to [0, 1]$ such that $F(\mathbf{x}) = \mathcal{P}(\mathbf{X} \le \mathbf{x}), \ \forall \mathbf{x} \in \mathbb{R}^n$. If there exists a non negative and integrable function $f: \mathbb{R}^n \to \mathbb{R}$ satisfying $F(\mathbf{x}) = \int_0^{\mathbf{x}} d\mathbf{y} f(\mathbf{y})$ then f is the density distribution function of \mathbf{X} . In probability theory the density distribution function is normalized in the sense $\int dx f(x) = 1$. Usually $f(\mathbf{X})$ is called the distribution function of \mathbf{X} . We will use this notation in the following chapters of this thesis.

The mean, average value or expected value of any function A(X) is an integral with measure f(x) dx:

$$\langle A \rangle = \int \mathrm{d}x f(x) A(x).$$
 (1.39)

In addition, we call $M^k = \langle x^k \rangle = \int x^k f(x) dx$ the *k*th-moments of the distribution. The most important are the first and the second moments, which define the mean and the variance:

$$m = \langle X \rangle = \int \mathrm{d}x f(x) x,$$
 (1.40)

$$\sigma^{2} = \langle (x - m)^{2} \rangle = \int dx f(x) x^{2} - m^{2}.$$
 (1.41)

In this work the 1D Gaussian distribution function of mean m and standard deviation σ is widely used. It is denoted by $N(m, \sigma)$ and its density function is:

$$f_N(x) = \frac{1}{\sqrt{2\pi\sigma^2}} \exp{-\frac{(x-m)^2}{2\sigma^2}}.$$
 (1.42)

The Wiener process increment that appears in Eq. 1.13 has this distribution with m = 0 and " $\sigma = \sqrt{dt}$ ".

The basic theorem in Monte Carlo methods is the central limit theorem. It requires the introduction of independent events. Two events A and B are independent if the

⁷ In Physics it is usual to normalize f to the total number of particles of the system: $\int dx f(x) = N$.

probability of A given B is equal to the probability of A:

$$P(A|B) = P(A) \Leftrightarrow A, B \text{ independent.}$$
 (1.43)

The central limit theorem requires a sequence X_i , i = 1, ..., n of independent and identically distributed variables with average m and variance σ^2 . We define the new random variable Z_n as

$$Z_n = \frac{S_n - nm}{\sigma \sqrt{n}} = \frac{\langle \hat{X} \rangle - m}{\sigma / \sqrt{n}},$$
(1.44)

where $S_n = \sum_{i=1}^n X_i$ and $\langle \hat{X} \rangle = \frac{1}{n} S_n$ is the sample mean. This theorem states that the variable Z_i will converge to the standard normal distribution N(0, 1) as n tends to infinity (2 of probability convergence, see [19]):

$$f_{Z_n} \to f_{N(0,1)}$$
 as $n \to \infty$. (1.45)

A Monte Carlo method consists in obtaining N independent realizations or measurements of a physical quantity \mathbf{X} and apply statistical techniques to extract information. The average value of the sample is the most usual estimator, and it can be shown that its error is given by:

$$\Delta \langle X \rangle = \frac{\sigma_X}{\sqrt{N}}.\tag{1.46}$$

This shows that the accuracy of $\langle X \rangle$ scales with $N^{-1/2}$. A more advanced technique [20] used to calculate the statistical error of any function of **X** is shown in Sect. 2.2.3. Reference [14] includes extensive information related to MC procedures.

In our case, we can say that the statistical accuracy of the simulation scales with $N^{-1/2}$ being N the number of trajectories integrated.

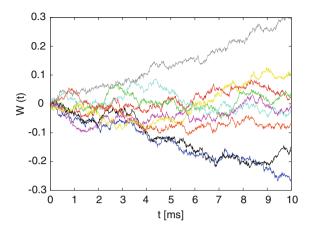
1.4.2 The Wiener Process

When dealing with stochastic equations there is a particular stochastic process with special interest: the Wiener process. We can find two Wiener processes in the equations solved in ISDEP (Eqs. (1.34)–(1.36)). They represent the random evolution of a particle in phase space due to collisions with the plasma background.

A real valued stochastic process W(t) is called a Wiener process (also called Brownian motion) when:

- 1. W(0) = 0.
- 2. W(t) W(s) is $N(0, t s) \forall t \ge s \ge 0$.
- 3. For all times $0 < t_1 < t_2, \ldots, < t_k$ the random variables $W(t_1), W(t_2) W(t_1), \ldots, W(t_k) W(t_{k-1})$ are independent (independent increments).

Fig. 1.4 Examples of the Wiener process W(t). Although the average value of several Wiener processes is always zero, the width of the distribution scales with time as $W^2(t) \sim t$. The time discretization in this examples is $dt = 10^{-5}$ s, so the increment dW is $N(0, \sqrt{10^{-5}})$



It can be shown mathematically that W(t) is not differentiable, but the notation dW(t) is widely used in SDE theory. Figure 1.4 shows examples of Wiener processes.

From a physicist point of view, we can say that " $dW^2 = dt$ ", but it is not exactly true from a mathematician perspective. Let us explain and clarify this concept.

First note that it is clear form the definition that $\langle W(t_b) - W(t_a) \rangle = 0$, $t_a < t < t_b$. We can show that " $dW^2 = dt$ " integrating both sides of the expression between t_a and t_b . The RHS integral is trivial:

$$\int_{t_a}^{t_b} \mathrm{d}t = t_b - t_a. \tag{1.47}$$

In order to calculate the LHS integral we need a partition of the interval:

$$\int_{t_a}^{t_b} dW^2 = \lim_{N \to \infty} \sum_{i}^{N} (W(t_{i+1}) - W(t_i))^2 = \lim_{N \to \infty} I_N,$$
 (1.48)

$$t_i = t_a + i/N(t_b - t_a). (1.49)$$

Since I_N are random variables, we must consider a statistical definition of the equality " $dW^2 = dt$ ". We will show that in the limit $N \to \infty$, I_N is no longer a stochastic variable and converges to $t_b - t_a$ in quadratic average. First, it is easy to show that the average $\langle I_N \rangle$ is equal to $t_b - t_a$.

$$\langle I_N \rangle = \langle \Delta W^2 \rangle$$

$$= \langle (W(t_b) - W(t_a))^2 \rangle$$

$$= \left\langle \sum_{i}^{N} (W(t_{i+1}) - W(t_i))^2 \right\rangle$$

$$= \sum_{i}^{N} \langle (W(t_{i+1}) - W(t_i))^2 \rangle$$

$$= \sum_{i}^{N} (t_{i+1} - t_i)$$

$$= t_b - t_a. \tag{1.50}$$

With this result and using the independence properties of the Wiener process, we can see that:

$$\lim_{N \to \infty} \langle (I_N - (t_b - t_a))^2 \rangle = 0. \tag{1.51}$$

Let us sketch the demonstration of this property. We will use the notation $W_k = W(t_k)$ for simplicity. After some straightforward algebra and using the basic properties of the Wiener process, we can see that:

$$\lim_{N \to \infty} \langle (I_N - (t_b - t_a))^2 \rangle = \lim_{N \to \infty} \left\langle \sum_{k=1}^{N} \sum_{j=1}^{N} (W_{k+1} - W_k)^2 (W_{j+1} - W_j)^2 - (t_b - t_a)^2 \right\rangle. \tag{1.52}$$

The independence of the Wiener processes allows us to simplify the double sum:

$$\lim_{N \to \infty} \langle (I_N - (t_b - t_a))^2 \rangle = \lim_{N \to \infty} \left\langle \sum_{k=0}^{N} (W_{k+1} - W_k)^4 - (t_b - t_a)^2 \right\rangle.$$
 (1.53)

Defining $Y_k = \frac{W_{k+1} - W_k}{\sqrt{t_{k+1} - t_k}}$ and noting that $Y_k = N(0, 1)$ and $\langle (Y_k^2 - 1)^2 \rangle = \langle Y_k^4 \rangle - 1$ we have:

$$\lim_{N \to \infty} \langle (I_N - (t_b - t_a))^2 \rangle = \lim_{N \to \infty} \left\langle \sum_{k=0}^{N} (Y_k^2 - 1)^2 (t_{k+1} - t_k)^2 \right\rangle.$$
 (1.54)

Since all the moments of the normal distribution are finite, the previous sum has an upper boundary:

$$\lim_{N \to \infty} \langle (I_N - (t_b - t_a))^2 \rangle \le C \lim_{N \to \infty} (t_{k+1} - t_k)^2, \qquad C = \text{constant.}$$
 (1.55)

If we consider that the partition of the interval (t_b, t_a) is uniform and $t_k = k(t_b - t_a)/N$ we find:

$$\lim_{N \to \infty} \langle (I_N - (t_b - t_a))^2 \rangle \le C \sum_{b=1}^{N} \left(\frac{t_b - t_a}{N} \right)^2 (t_b - t_a)^2$$
 (1.56)

$$= C(t_b - t_a)^4 \lim_{N \to \infty} \sum_{b}^{N} \left(\frac{1}{N}\right)^2 \to 0.$$
 (1.57)

Thus, we can say that $dW^2 = dt$ in quadratic average since I_N does not fluctuate when $N \to \infty$. For practical purposes, we will generate the random numbers ΔW as $N(0, \Delta t)$ in the numerical algorithms.

Once we have the Wiener process defined, we may ask ourselves how stochastic integrals like $\int dW g(t, x(W, t))$ are defined. The basic definition is the Itô integral:

$$\int_{t_a}^{t_b} dW \, g(t, x(W, t)) = \lim_{N \to \infty} \sum_{i}^{N} (W(t_{i+1}) - W(t_i)) \, g(t_i), \tag{1.58}$$

where we have introduced the notation $g(t_i) = g(t_i, x(t_i, W(t_i)))$. This definition has many mathematical advantages (as Markovianity) and it is used in the theory of SDEs, despite not being very appropriated for practical purposes. Itô's formalism in SDE is based in evaluating the function g(t) in the beginning in the Riemann sum of $\int g(t) dW$, but there are many other possibilities.

The same Riemann sum, but evaluating g(t) in the interval midpoint leads to the Stratonovich integral, denoted by the symbol \circ :

$$\int_{t_a}^{t_b} dW \circ g(t, x(W, t)) = \lim_{N \to \infty} \sum_{i}^{N} (W(t_{i+1}) - W(t_i)) \frac{g(t_{i+1}) + g(t_i)}{2}, \quad (1.59)$$

Let us illustrate these two definitions with an example solving the stochastic integral with g(t) = W(t):

$$\int_0^t W dW. \tag{1.60}$$

According to the Itô definition:

$$\int_0^t W dW = \lim_{N \to \infty} \sum_k W(t_k) \left(W(t_{k+1}) - W(t_k) \right). \tag{1.61}$$

Using that $W(t_{k+1}) = 1/2 (W(t_{k+1}) - W(t_k) - (W(t_{k+1}) - W(t_k)))$

$$\int_{0}^{t} W dW = \lim_{N \to \infty} \sum_{k} \frac{\left(W^{2}(t_{k+1}) - W^{2}(t_{k})\right)}{2} - \lim_{N \to \infty} \sum_{k} \frac{\left(W(t_{k+1}) - W(t_{k})\right)^{2}}{2}$$

$$= \frac{W^{2}(t)}{2} - \frac{t}{2}.$$
(1.62)

On the other hand, the Stratonovich algebra considers that the integrand in Eq. (1.60) is evaluated in the midpoint of the partition interval.

$$\int_{0}^{t} W \circ dW = \lim_{N \to \infty} \sum_{k} \frac{W(t_{k+1}) + W(t_{k})}{2} (W(t_{k+1}) - W(t_{k})).$$

$$= \frac{1}{2} \sum_{k} W^{2}(t_{k+1}) - W^{2}(t_{k})$$

$$= \frac{W^{2}(t)}{2}.$$
(1.63)

These two examples have shown that the solution to a stochastic integral depends on the algebra chosen and that the Stratonovich convention is simpler for practical cases. Fortunately, it is possible to obtain the Itô solution from the Stratonovich solution and vice-versa [14, 19].

In this thesis we will find cases with several Wiener processes involved. They will be labeled with a superscript and are taken to be statistically independent: dW^j (0) = 0, $\langle dW^j(t) \rangle = 0$, $\langle dW^j(t) \rangle dW^k(t) \rangle = \delta^{jk} dt$.

A set of trajectories in a fusion device that are obtained integrating Eqs. (1.34)–(1.36) is a set of independent random variables. The reason is that test particles do not interact with each other and all the Wiener processes that appear are independent. Therefore the Central Limit Th. can be applied to the set of trajectories, using Monte Carlo techniques to procure physical results. Chapter 2 contains more information about how these methods are implemented in the simulation code ISDEP.

1.4.3 Stochastic Differential Equations

SDEs are differential equations that include random terms with certain probability distribution. They are commonly used in Physics to model diffusive transport processes [21]. A 1D Stochastic Differential Equation is an equation with the form:

$$dX = F(X, t)dt + G(X, t)dW, \tag{1.64}$$

being dW an infinitesimal increment, differential, of the Wiener process: $\langle dW \rangle = 0$, $\langle dW^2 \rangle = dt$.

Since $\mathrm{d}W \approx \sqrt{\mathrm{d}t}$ in stochastic analysis, most theorems and techniques used in regular calculus are modified. The chain rule in ordinary calculus, i.e., finding

dY(X, t) given dX, is named Itô's rule in stochastic calculus. It is obtained expanding Y(X, t) in Taylor series up to first order, taking into account that " $dW^2 = dt$ ":

$$Y(X(t + \Delta t), t + \Delta t) = Y(X(t) + F(t)\Delta t + G(t)\Delta W, t + \Delta t)$$

$$= Y(X(t), t) + \frac{\partial Y}{\partial t}\Delta t$$

$$+ \frac{\partial Y}{\partial X}(F(t)\Delta t + G(t)\Delta W)$$

$$+ \frac{1}{2}\frac{\partial^2 Y}{\partial X^2}G(t)^2\Delta W^2 + O(\Delta t^{3/2}). \tag{1.65}$$

Grouping terms:

$$d(Y(X,t)) = \frac{\partial Y}{\partial t}dt + \frac{\partial Y}{\partial X}dX + \frac{1}{2}\frac{\partial^2 Y}{\partial X^2}G^2dt + O(dt^{3/2}). \tag{1.66}$$

For example, X = W, $dX = dW \Rightarrow d(X^2) = d(W^2) = 2WdW + dt$.

A more general case is the SDE in n dimensions (using the Einstein summation convention):

$$dX^{i} = F^{i}(\mathbf{X}, t)dt + G^{i}_{i}(\mathbf{X}, t)dW^{j}, \qquad (1.67)$$

$$d(Y(\mathbf{X})) = \frac{\partial Y}{\partial t} dt + \frac{\partial Y}{\partial X^i} dX^i + \frac{1}{2} \frac{\partial^2 Y}{\partial X^i \partial X^j} G_l^i G^{jl} dt.$$
 (1.68)

Moreover, in stochastic analysis the product rule is modified:

$$dX^{1} = F^{1}dt + G_{k}^{1}dW^{k}$$

$$dX^{2} = F^{2}dt + G_{k}^{2}dW^{k} \Rightarrow d(X^{1}X^{2}) = X^{1}dX^{2} + X^{2}dX^{1} + G^{1k}G_{k}^{2}dt. \quad (1.69)$$

Concerning the integration of differential equations, a stochastic process $\mathbf{X}(t)$ is a solution of the SDE:

$$d\mathbf{X} = \mathbf{F}(\mathbf{X}, t)dt + \mathbf{G}(\mathbf{X}, t)d\mathbf{W}, \tag{1.70}$$

$$\mathbf{X}(0) = \mathbf{X}_0,\tag{1.71}$$

when

$$\mathbf{X}(t) = \mathbf{X}_0 + \int_0^t \mathbf{F}(\mathbf{X}(s), s) ds + \int_0^t \mathbf{G}(\mathbf{X}(s), s) d\mathbf{W}.$$
 (1.72)

The solution of the SDE is formulated using the integral because, as we said, the Wiener process is not differentiable. The existence and uniqueness of the solution is guaranteed provided some general conditions to F and G. As an example, let us check that the solution to the differential equation:

$$dX = q(t)XdW, (1.73)$$

$$X(0) = 1, (1.74)$$

is

$$X(t) = \exp\left(-\frac{1}{2} \int_0^t g^2(s) ds + \int_0^t g(s) dW\right).$$
 (1.75)

Call $dZ = -\frac{1}{2}g^2dt + gdW$, so $X(t) = \exp(Z(t))$. Using the chain rule: $dX = X(-\frac{1}{2}g^2dt + gdW) + X\frac{1}{2}g^2dW = gXdW$.

Many analytical and numerical methods for solving SDE use the Stratonovich convention. Under general differentiability requirements for F and G it is equivalent to Itô's convention. The transformation from a Stratonovich SDE to an Itô SDE is:

$$dX^{i} = \hat{F}^{i}(\mathbf{X}, t)dt + G^{i}_{i}(\mathbf{X}, t) \circ dW^{j}, \tag{1.76}$$

$$\hat{F}^{i}(\mathbf{X},t) = F^{i}(\mathbf{X},t) - \frac{1}{2} \frac{\partial G_{k}^{i}(\mathbf{X},t)}{\partial X^{j}} G^{jk}(\mathbf{X},t). \tag{1.77}$$

The diffusion tensor G^{ij} is not changed. The main advantage of the Stratonovich convention is that the ordinary chain rule holds formally:

$$d(Y(\mathbf{X},t)) = \frac{\partial Y}{\partial t} dt + \frac{\partial Y}{\partial X^i} \hat{F}^i dt + \frac{\partial Y}{\partial X^j} G_k^j \circ dW^k, \tag{1.78}$$

and this is the reason why it is generally used in numerical methods for SDE.

We can solve again the integral $\int dWW(t)$ using both chain rules, as we did in Eqs. (1.62) and (1.63) using the Riemann sums. Differentiating W^2 in Itô's sense:

$$d(W^2) = 2WdW + dt \Rightarrow WdW = d(W^2) - dt.$$
 (1.79)

Integrating in both sides of the last equation we get:

$$\int_0^t W dW = \frac{W^2(t) - t}{2}.$$
 (1.80)

On the other hand, we can solve this integral directly in the Stratonovich formulation:

$$\int_0^t W \circ dW = \frac{W^2(t)}{2}.$$
 (1.81)

1.4.4 Numerical Methods

ISDEP has several numerical methods to solve the SDE system, with different properties and convergence orders. When dealing with numerical solution of SDEs one has to distinguish two types of convergence, strong and weak convergence [14]. Strong convergence is a concept similar to the usual convergence in ordinary differential equations, related to a particular realization of the Wiener process and a single trajectory. Weak convergence is related to averages and statistical quantities of a set of solutions.

Since most of the ISDEP results are statistical functions of the particle orbits, weak convergence is the leading criteria for the numerical methods used. As an example, an order one weak algorithm is the Euler-Maruyama scheme:

$$x_{n+1}^{i} = x_n^{i} + F^{i}(\mathbf{x}_n) \, \Delta t + G_{j}^{i}(\mathbf{x}_n) \, \Delta W^{j}.$$
 (1.82)

The superscript *i* refers to the components of the vector **x** while *n* is the time index. Note that this algorithm is very similar to the numerical model of the diffusion process in Eq. (1.37). An order two weak algorithm is the Klauder-Petersen method (note that $\Delta W = \sqrt{\Delta t} \, \eta, \, \eta = N(0, 1)$):

$$x_{n+1}^{i} = x_{n}^{i} + \frac{1}{2} \left(F^{i}(\mathbf{x}_{n}) + F^{i}(\mathbf{x}^{1}) \right) \Delta t + \frac{1}{2} \left(G_{j}^{i}(\mathbf{x}^{2}) + G_{j}^{i}(\mathbf{x}^{3}) \right) \sqrt{\Delta t} \, \eta_{0}^{j},$$
(1.83)

$$x^{1i} = x_n^i + F^i(\mathbf{x}_n) \,\Delta t + G_i^i(\mathbf{x}_n) \,\sqrt{\Delta t} \,\eta_0^j, \tag{1.84}$$

$$x^{2i} = x_n^i + G_i^i(\mathbf{x}_n) \sqrt{\Delta t/2} \, \eta_1^j, \tag{1.85}$$

$$x^{3i} = x_n^i + F^i(\mathbf{x}_n) \, \Delta t + G_i^i(\mathbf{x}_n) \, \sqrt{\Delta t/2} \, \eta_1^j, \tag{1.86}$$

$$\eta_0^j = N(0, 1), \tag{1.87}$$

$$\eta_1^j = N(0, 1). \tag{1.88}$$

In this method the vectors \mathbf{x}^1 , \mathbf{x}^2 and \mathbf{x}^3 have components x^{1i} , x^{2i} and x^{3i} . Additionally, the Kloeden-Pearson algorithm is valid for a Stratonovich SDE:

$$x_{n+1}^{i} = x_n^{i} + \frac{1}{2} \left(\hat{F}^{i}(\mathbf{x}_n) + \hat{F}^{i}(\mathbf{x}_p) \right) \Delta t + \frac{1}{2} \left(G_j^{i}(\mathbf{x}_n) + G_j^{i}(\mathbf{x}_p) \right) \sqrt{\Delta t} \, \eta^{j}, \tag{1.89}$$

$$x_p = x_n^i + \hat{F}^i(\mathbf{x}_n) \,\Delta t + G_i^i(\mathbf{x}_n) \,\sqrt{\Delta t} \,\eta^j, \tag{1.90}$$

$$\eta^j = N(0, 1). \tag{1.91}$$

26 1 Introduction

This also presents order two weak convergence. The numerical method may be chosen according to the parameters of a particular simulation. In a high collisionality regime a high order method in the stochastic part should be used. In low collisionality cases a first order method in the stochastic part combined with a fourth order Runge-Kutta for the deterministic part can produce excellent results.

Evidently, we must make sure that our time discretization interval Δt is small enough to assure convergence of the solution (within the statistical error-bars). All other numerical parameters must also be small enough to not affect the results. For example, the functions F^i and G^{ij} depend on a tabulated the magnetic field whose discretization length must be much smaller than any other typical length of the system.

In general, the numerical methods for SDE must satisfy two general consistency conditions:

$$\lim_{\Delta t \to 0} \left\langle \frac{x_{n+1}^i - x_n^i}{\Delta t} \right\rangle = F^i, \tag{1.92}$$

$$\lim_{\Delta t \to 0} \left\langle \frac{(x_{n+1}^i - x_n^i)(x_{n+1}^j - x_n^j)}{\Delta t} \right\rangle = G_k^i G^{kj}, \tag{1.93}$$

where, again, we make use of the Einstein summation convention.

All the numerical methods we use in SDE are numerically stable, in the sense that small deviations from the initial condition do not cause the solution to diverge rapidly from the original solution. These properties can be found in [14], with examples and formal theorems.

The next chapter is devoted to a description of the ISDEP code. Then we will show the original scientific results obtained with the code, using the techniques and tools previously described.

References

- 1. Hasegawa A et al (1986) Phys Rev Lett 56:139
- 2. Goldston RJ, Rutherford PH (1995) Introduction to plasma physics. Taylor and Francis, London
- 3. Boozer AH (2005) Rev Mod Phys 76:1071
- Helander P, Sigmar DJ (2001) Collisional transport in magnetized plasmas. Cambridge University Press, Cambridge
- 5. Hazeltine RD, Meiss JD (2003) Plasma confinement. Dover Publications, USA
- 6. Goerler T et al (2011) Journal of Computational Physics 230:7053
- 7. Pitcher CS, Stangeby PC (1997) Plasma Phys Controlled Fusion 39:779
- 8. D'Haeseleer W, Hitchon W, Callen J, Shohet J (2004) Flux coordinates and magnetic field structure. Springer-Verlag, Berlin
- 9. Balescu R (1975) Equilibrium and nonequilibrium statistical mechanics. Wiley, USA
- Balescu R (1988) Transport processes in plasmas: neoclassical transport theory. Elsevier Science Ltd, The Netherlands
- 11. Hinton FL, Hazeltine RD (1976) Rev Mod Phys 48:239

References 27

- 12. Brizard AJ, Hahm TS (2007) Rev Mod Phys 79:421
- 13. Peeters AG (2000) Plasma Phys Controlled Fusion 42:B231
- Kloeden PE, Platen E (1992) Numerical solution of stochastic differential equations. Springer-Verlag, Berlin
- 15. Boozer A, Kuo-Petravic G (1981) Phys Fluids 24(5):851
- 16. Chen T (1988) A general form of the coulomb scattering operators for monte carlo simulations and a note on the guiding center equations in different magnetic coordinate conventions (Max Planck Institute fur Plasmaphisik. 0/50, Germany
- 17. Velasco J et al (2008) Nucl Fusion 48:065008
- 18. Christiansen JP, Connor JW (2004) Plasma Phys Controlled Fusion 46:1537
- 19. Evans L (2000) An introduction to stochastic differential equations. UC Berkeley, Department of Mathematics. http://math.berkeley.edu/~evans/SDE.course.pdf
- Amit D, Martin-Mayor V (2005) Field theory the renormalization group and critical phenomena, 3rd edn. World Scientific Publishing, Singapore
- Kampen NV (2007) Stochastic processes in physics and chemistry, 3rd edn. North-Holland Personal Library, Amsterdam

Chapter 2 ISDEP

2.1 Introduction

As we said in previous chapters, Integrator of Stochastic Differential Equations for Plasmas (ISDEP) is a code devoted to solve the dynamics of a minority population of particles in a complex 3D fusion device. ISDEP is becoming a rather complex code, with more than 10⁴ lines. It is adapted to four different fusion device geometries (two stellarators and two tokamaks). In this Chapter we discuss the basic structure of the code and the tools used to analyze the data in Sect. 2.2 and *benchmark* the code in Sect. 2.3. With *benchmark* we mean the comparison of the ISDEP results with another similar code, in order to assure that ISDEP is free of programming errors. We end this Chapter with an overview of the previously published results in Sect. 2.4.

The main improvements of the code performed during the elaboration of this thesis are related with the measurements and analysis of the particle distribution function (Sects. 2.2.5 and 2.2.6) and its adaptation to three new fusion devices (in Sect. 2.3 for the *benchmark* and in Chaps. 3 and 4).

We start with a description of the code.

2.2 Description of the Code

ISDEP was created under the CIEMAT¹-BIFI²-UCM³ collaboration in 2007 and is in continuous development and improvement. From a physical point of view, ISDEP solves the Neoclassical (NC) transport avoiding several common approximations of the standard NC theory implemented in existing transport codes.

¹ Centro de Investigaciones Energéticas, Medio Ambientales y Tecnológicas, Madrid, Spain.

² Instituto de Biocomputación y Física de los Sistemas Complejos, Zaragoza, Spain.

³ Universidad Complutense de Madrid, Madrid, Spain.

As an example, it makes use of the Cartesian coordinates instead of the Boozer coordinates [1], generally used in this code class. Boozer coordinates are specific coordinates for magnetically confined plasmas, but they do not allow the representation of magnetic islands, ergodic zones in the magnetic field or points in space outside the plasma boundary, where the field lines are open. Boozer and magnetic coordinates are only well defined for nested magnetic surfaces but not for those topologies. Therefore, Cartesian coordinates are better suited for our goal. Other common approximations that we can avoid with ISDEP are related to the typical radial width of the particle orbits in the device and the diffusive nature of the transport processes. The particle orbit width is usually assumed to be small compared with the typical distances of the problem, but in many real situations this is not actually the case. Finally, the kinetic energy of the studied particles does not need to be conserved in ISDEP, oppositely to the neoclassical approximation. This allows us the inclusion of strong electric fields and study their effects on ion dynamics. In addition, this code was designed to run on grid architectures, propelling the development of this computing platforms.

As we previously said, ISDEP considers a minority population of test particles, for which we may choose among several options. This minority population can be thermal particles, obtaining then specific information for the plasma bulk that is not given by the plasma equilibrium. The test particle can also be fast particles coming from heating systems, studying then their interaction with thermal particles. Furthermore, although we have not considered the case yet, ISDEP has the potential to handle impurity dynamics.

There exist many computer codes devoted to solve the Neoclassical transport. For example, the codes DKES, NEO-MC and MOCA study similar physics, but with some peculiarities and different approximations. Some of these neoclassical codes have been *benchmarked* and compared in Ref. [2].

• Drift Kinetic Equation Solver (DKES) [3] is a well established code that solves the linearized Drift Kinetic Equation using a functional minimization method. It takes the effective radius and the particle energy as input parameters and then solves the transport equations in the remaining three dimensions.

DKES solves a FP type equation and computes the whole transport matrix [2] using Boozer coordinates, calculating also the *Bootstrap* current and the parallel conductivity. Unfortunately it presents some drawbacks that ISDEP avoids. It assumes diffusive nature in the transport, infinite fast parallel transport, conservation of kinetic energy and narrow radial excursions of the particle. Moreover, it neglects the poloidal component of the ∇B drift and approximates

$$\frac{\mathbf{E} \times \mathbf{B}}{B^2} \sim \frac{\mathbf{E} \times \mathbf{B}}{\langle B^2 \rangle}.$$
 (2.1)

The use of Boozer coordinates means that the code can be used only when one has nested magnetic surfaces and cannot be used in the scrape-off-layer.

Computationally, it scales unfavorably with the number of magnetic field Fourier modes, but it is very fast in high collisionality regimes. This code gives large errorbars for the transport coefficients in the long mean free path regime for complex magnetic configurations. Indeed it is not adequate to study complex 3D devices in a low collisionality regime.

- NEO-MC [4] solves the same equations as DKES but using a Monte Carlo method instead. NEO-MC has been designed to specifically calculate the *Bootstrap* current in 3D fusion devices. The main advantage of NEO-MC is that it reduces strongly the errorbars of the transport coefficients for any collisional regime. In order to improve the accuracy of the code to estimate the *Bootstrap* current, the effect of trapped and barely trapped particles is considered specifically. The velocities of two particles that are moving in opposite directions are subtracted, thus creating a quasi-particle and the number of test particles is increased in the barely trapping regions. Most of the computing time is devoted to follow particles. This improves the scalability, although this code is more expensive in computing resources than DKES. Like DKES, NEO-MC is subjected to the neoclassical ordering. Thus, NEO-MC cannot avoid such approximations that are not present in ISDEP. On the other hand, NEO-MC calculates also for the electrons and, hence, allows one to estimate the self-consistent radial electric field from the ambipolar condition. NEO-MC, like DKES, also assumes nested magnetic surfaces.
- MOCA [5] is another Monte Carlo code developed at CIEMAT ten years ago. MOCA is an evolution of the MCT code [6] and it calculates the radial diffusion coefficients (diagonal part of the transport matrix), using Boozer coordinates for the spatial position and Coulomb collisions for the interaction between particles. It usually scales better than DKES, but it does not allow for the bootstrap current calculation in its first version. Opposite to ISDEP, MOCA works in Boozer coordinates and is subjected to the neoclassical ordering, but calculates for both ions and electrons.
- MOHR [7] is another guiding center orbit code that solves the Fokker-Planck equation for ions. MOHR is a very similar code to ISDEP indeed. The main differences rely on the statistical error calculation.

Once we have the mathematical model of the particle dynamics from Chap. 1, we describe the Monte Carlo method used in ISDEP, the architecture of the code and the statistical techniques needed to obtain global results from a set of independent trajectories. Then we present an overview of previous ISDEP results and, finally, the ISDEP code is *benchmarked* with MORH in Sect. 2.3.

2.2.1 The Monte Carlo Method

The basis of the Monte Carlo method used in ISDEP relies on the equivalence between the Fokker-Planck and Langevin equations [8]. The Fokker-Planck equation is a linear partial differential equation for a distribution function of a minority population of

particles (called test particles) that interact with a static background. The Langevin approach is equivalent to this description, but providing Stochastic Differential Equations (SDE) [8] for a single test particle motion (see Sect. 1.4). Integrating many test particle trajectories and analyzing the results is mathematically equivalent to obtain the solution to the original Fokker-Planck equation.

ISDEP integrates the trajectories taking into account collisions with ions and electrons from the background, the electrostatic potential and the confining magnetic field. The statistical analysis of many test particles allows the measurements of different plasma parameters, like average energy, confinement time or even the marginal distribution function of the test particle population.

In order to reduce computational requirements, the Guiding Center (GC) approximation, described in Sect. 1.3, is used in the code. The GC coordinates chosen are (x, y, z, v^2, λ) , where (x, y, z) are the guiding center space coordinates, v^2 is the normalized particle kinetic energy and

$$\lambda = \mathbf{v} \cdot \mathbf{B}/(B \, v) \tag{2.2}$$

is the pitch. In the Fokker-Planck description, the time evolution of the distribution function f(x,t) is given by the convective $(F^i(x,t))$ and the diffusive transport $(G^i_j(x,t))$ in the 5D phase space:

$$\frac{\partial f(x,t)}{\partial t} = \frac{\partial}{\partial x^i} \left(-F^i(x,t) + \frac{1}{2} \frac{\partial}{\partial x^j} G^i_k(x,t) G^{kj}(x,t) \right) f(x,t) . \tag{2.3}$$

The equivalent set of Stochastic Differential Equations (SDE) in Itô's sense [8] (i.e. Langevin equations) is:

$$dx^{i} = F^{i}(x, t) dt + G^{i}_{j}(x, t) dW^{j}.$$
 (2.4)

The explicit form of F_i and G_{ij} has been discussed in Eqs. (1.34), (1.35) and (1.36). Now the coordinates in phase space x^i refer to the movement of a single particle, whose trajectory is determined by the background via F^i and G^i_j . The Wiener process, $\mathrm{d}W^j(t)$ (see Sect. 1.4) represents the random part of the interaction with the plasma.

In the case of interest, the problem consists of a SDE system of five equations with two Wiener processes. The SDEs can be transformed to the Stratonovich convention because it is more suitable for several numerical methods. In Sect. 1.4 the reader can find a short review of probability theory and stochastic calculus, which provide the necessary tools for the calculations of this thesis.

Once *N* trajectories are integrated and stored, we can reconstruct the distribution function accumulating the particle path in phase space:

$$f(\mathbf{x},t) \propto \frac{1}{N} \sum_{i=1}^{N} \delta(\mathbf{x} - \mathbf{x}(t)).$$
 (2.5)

Since ISDEP calculates f according to the time that the particles spend in a given point of the phase space, the Jacobian of the coordinates \mathbf{x} is included in $f(\mathbf{x},t)$. In addition, due to the linear nature of ISDEP, $f(\mathbf{x},t)$ is not exactly a distribution function because all its results have implicit a normalization constant. This means that ISDEP can calculate the intensive properties of the test particles (average energy, average lifetime, etc), but needs some extra information to compute the extensive properties (total energy contained, total electric current, etc).

With the proper normalization, $f(\mathbf{x}, t)$ can be taken as a probability density of the test particle ensemble in phase space.

2.2.2 ISDEP Architecture

ISDEP is programmed in C to maximize its performance and portability and was designed to scale perfectly in distributed computing platforms such as grid or volunteer computing architectures. It does not require external libraries other than the standard C libraries. Consequently, the scaling in massive parallel computers is almost linear. The operation of the code is briefly summarized in the following steps:

Initialization

After compiling, a copy of the executable and the input files are sent to each computing node, or copied into a file-system common to all nodes. The input files contain the plasma background data, the confining magnetic field and trajectory details (time step, numerical algorithm chosen, etc). The first stages of the execution of the code are invested in initializing the random number generator, the magnetic field array and the trajectory itself. The magnetic field array contains all the information related to the magnetic configuration of the device. Part of this array is read from a file (e.g., **B**) and the remaining is calculated (e.g., ∇B) in order to save CPU time in the next steps. The interpolations in this array are linear, provided that the spatial grid is dense enough. The typical distance between two nodes in the magnetic grid is <1% of the size of the device so the magnetic field is smooth enough. The size of the magnetic array may be \sim 400 MB, representing most of the memory that ISDEP uses.

The trajectories are initialized according to a given distribution. If one deals with bulk ions, the spatial distribution is given by the plasma density. In velocity space the distribution is locally Gaussian in v^2 and uniform in λ . Alternatively, when dealing with suprathermal ions, ISDEP can read the output of a neutral beam injection code, like FAFNER2 [9], to calculate the initial test particle distribution (see Chap. 4).

Orbit Iintegration

After the initialization routines, every node starts to integrate trajectories independently of each other. The statistical independence is guaranteed reading the random

seed locally in the node. Then the orbits are integrated and the data written in a file. A description of the numerical methods used in ISDEP can be found in Sect. 1.4.4. This is the most CPU time consuming stage.

There are two main output files in ISDEP: trajectory files (OUT.DAT) and histogram files (OUT.HIS). In the former the 5D position in phase space is stored for each trajectory at selected times. Since we are interested in the plasma evolution time scales, the measurement times are chosen to be approximately equidistant in logarithmic scale. The latter contains histograms of different particle quantities (energy, distribution function, rotation velocity, radial flux, ...). In order to increase statistics the following technique is applied in the histograms: assuming that the evolution of the system is slow, one may take all the measurements at times $t \in (0.9 t_0, 1.1 t_0)$ belonging to t_0 . In this way the statistical errors are significantly reduced.

Analysis

The output of each node is stored in a particular node and is analyzed with the ISDEP analysis tools. Many physical quantities are calculated in this stage, like average energy, velocity profiles, steady state distribution function and escape points. ISDEP uses the jack-knife method for all statistical error estimation [10], described in Sect. 2.2.3. Some output analysis, related to Sects. 2.2.5 and 2.2.6 is done using the Python programming language.

Table 2.1 summarizes the profiles measured with ISDEP, as functions of the effective radius and time. In addition, ISDEP calculates the global average of all these magnitudes as a function of time. Finally, the distribution function of the test particles is obtained, but averaging in the magnetic surfaces: $f(t, \rho, v_{\parallel}, v_{\perp})$.

The particle escape distribution is presented as a list of points in phase space: $(t_i, x_i, y_i, z_i, v_i^2, \lambda_i)$, being t_i the escape time of the *i*th particle. A lot of information can be extracted from this list with little effort. For example, accumulation of losses in a region of the device can produce severe damage to the device, and ISDEP can help to prevent this effect.

It is essential to mention that ISDEP requires some feedback to determine the time discretization parameter Δt . The usual procedure to determine Δt requires at least two simulations with ISDEP. First one must decide what statistical accuracy in the output is needed, usually around 5 %. This errorbars can be diminished knowing that they scale with $N^{-1/2}$, being N the total number of trajectories integrated. Then, starting with some reasonable value of Δt , ISDEP is run for $\Delta t/2$, $\Delta t/5$, $\Delta t/10$... until the results are the same within the statistical errorbars. This procedure must be done for each simulation to ensure that the statistical errors are always larger than the discretization errors.

Figure 2.1 shows the workflow of ISDEP in a distributed computing architecture like the grid.

Table 2.1 ρ -dependent profiles calculated with ISDEP. Each one is presented as a function of time

1D profile observable	meaning
-----------------------	---------

ρ	Average effective radius	
$(\rho - \rho_0)^2$	Deviation from the initial position	
θ	Poloidal angle	
E	Total energy [units of $mc^2/2$]	
v^2	Normalized kinetic energy	
κ_v	Binder cumulant of v : $\kappa_v = \langle v^4 \rangle / \langle v^2 \rangle^2$	
λ	Pitch angle	
v_b	Parallel velocity, in units of c	
v_h^2	Parallel kinetic energy	
κ_{v_b}	Binder cumulant of v_b	
v_{arphi}	Toroidal velocity	
$egin{array}{c} v_{arphi} \ v_{arphi}^2 \end{array}$	Normalized toroidal kinetic energy	
$\kappa_{v_{arphi}}$	Binder cumulant of v_{φ}	
$v_{ heta}$	Poloidal velocity	
v_{θ}^2	Normalized poloidal kinetic energy	
$\kappa_{v_{ heta}}$	Binder cumulant of v_b	
v_r	Radial velocity	
v_r^2	Normalized radial kinetic energy	
κ_{v_r}	Binder cumulant of v_r	
Γ	Radial particle flux	
Q	Radial energy flux	
z	Average z coordinate	

2.2.3 Output Analysis: Jack-Knife Method

ISDEP incorporates the Jack-Knife method [10] for output analysis. This method is a robust and simple algorithm for the statistical error calculation.

Let us consider a set of N independent, identically distributed vector random variables, \mathbf{X}_i , $i=1,\ldots,N$, and a nonlinear function f of the expectation values $\langle \mathbf{X} \rangle$. By a vector random variable, we intend a set of M physical quantities that are measured on the same experiment (or numerical simulation) $\mathbf{X}_i = (X_i^{(1)}, X_i^{(2)}, \ldots, X_i^{(M)})$. Of course, the components of \mathbf{X}_i can be statistically correlated, but they are independent in the subscript i.

The problem that the Jack-Knife method solves is that of computing the statistical error for our estimator of $f(\langle \mathbf{X} \rangle)$. The procedure takes care at once of two problems: (i) it treats correctly the statistical correlations among the components of \mathbf{X}_i and (ii) it avoids the instabilities caused by the non-linear nature of the function f.

As an example, we may think of $X_i^{(m)}$ as the energy of the *i*th particle at time t_m . Even thought there will be no correlation between particles, obviously the energy of a given particle is correlated in time with itself. Thus, the calculation of the time

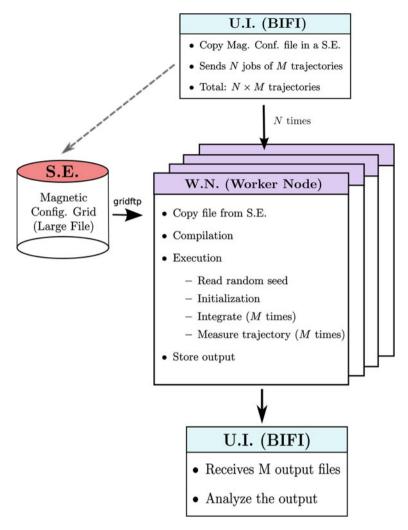


Fig. 2.1 ISDEP workflow on the grid. First, the magnetic field file is copied to a Storage Element (SE) and the jobs submitted to the Worker Nodes (WN). The WN retrieve copies of the magnetic field file from the SE, integrate a certain number of trajectories specified by the user and compress the result. When finished, all output files are copied back to the User Interface (UI) and then locally analyzed

differences in the kinetic energy requires a method that includes correlations between measurements.

The Jack-Knife procedure is as follows:

We first compute the average of the random variables as

$$\overline{\mathbf{X}} = \frac{1}{N} \sum_{i=1}^{N} \mathbf{X}_i, \tag{2.6}$$

and construct the estimator for $f(\langle \mathbf{X} \rangle)$

$$\overline{f} = f(\overline{\mathbf{X}}). \tag{2.7}$$

A direct computation of the statistical error using the random variables $f_i = f(\mathbf{X}_i)$ would be impractical (unless f is nearly a linear function). On the other hand, an error propagation computation requires to take into account the statistical correlations of the different components of \mathbf{X}_i . A simple alternative procedure consist in the following. First define the (non independent) random variables

$$\mathbf{X}_{i}^{\text{JK}} = \frac{1}{N-1} \sum_{j=1; j \neq i}^{N} \mathbf{X}_{j},$$
 (2.8)

and

$$f_i^{\text{JK}} = f(\mathbf{X}_i^{\text{JK}}),\tag{2.9}$$

then compute the Jack-Knife estimate for the statistical error of \overline{f}

$$\Delta_{\overline{f}} = \sqrt{(N-1) \left[\sum_{i=1}^{N} \frac{(f_i^{\text{JK}})^2}{N} - \left(\sum_{i=1}^{N} \frac{f_i^{\text{JK}}}{N} \right)^2 \right]}.$$
 (2.10)

Note that the error is proportional to the square root of the number of blocks, rather than to $\frac{1}{\sqrt{N}}$. The number of blocks should be large enough, say 50, so this technique works properly. It is straightforward to show that the Jack-Knife method gives the same results as Eq. (2.11) for linear functions.

$$\overline{f} = \frac{1}{N} \sum_{1}^{N} f_i, \qquad \Delta_{\overline{f} \text{ Linear-only}} = \sqrt{\frac{\overline{f^2} - \overline{f}^2}{N - 1}}.$$
 (2.11)

2.2.4 Computing Platforms

Since the communication between nodes is zero, ISDEP is able to run in several computing platforms: high performance computing (HPC) and distributed platforms. The scaling with the number of nodes is, in all cases, almost linear as we mentioned above.

In distributed platforms there is no fast communication between the nodes. On the contrary, a huge number of nodes are available. These nodes are very inhomogeneous

in performance and characteristics, so ISDEP should be as stable as possible to minimize the problems caused by this fact. Grid and volunteer computing are the main resources used. Grid is provided by the Fusion Virtual Organization (EGEE⁴ [11] and EGI-InSPIRE⁵ projects). The volunteer computing projects Ibercivis [12] and its precursor Zivis [13] have provided hundreds of thousands of CPU hours. Moreover, they had an important role in the divulgation of fusion science in Spain and Portugal. ISDEP was designed from the early steps to run on Grid architectures, but it had to be adapted to volunteer computing.

High Performance Computing (HPC) consists of a set of nodes (cluster) located in the same facility, characterized by fast communication between nodes. In this work, HPC time is provided by the EULER cluster at CIEMAT. EULER is formed by 1,152 Xeon cores (13.8 Tflops), connected with Infiniband.

2.2.5 Steady State Calculations

The steady state of a system is a time-invariant state in which the particle and heat sources and sinks are in equilibrium with each other. The sinks in ISDEP are caused by the lost particles that escape from the plasma and hit the vacuum vessel. In ISDEP we calculate the steady state of the test particle distribution, using the Green function's formalism, following Ref. [14]. Let f(x, t) be the distribution function of our system, t the time, t the coordinates in phase space, t a differential operator over t and t and t are source term. With this notation, the problem is expressed as:

$$\mathcal{L}(f(x,t)) = S(x,t). \tag{2.12}$$

In the case of interest f(x,t) is the minority particle distribution function, \mathcal{L} is the Fokker Planck operator for the guiding center and Boozer-Kuo-Petravic collision operator and the source is the continuous injection of particles into the plasma, computed with other MC codes. The Green function $G(x,t;x_0)$ is defined such that

$$\mathcal{L}(G(x,t;x_0)) = \delta(x - x_0)\,\delta(t),\tag{2.13}$$

with x_0 playing the role of initial position. Then:

$$f(x,t) = \int dt_0 dx_0 G(x, t - t_0; x_0) S(x_0, t_0), \qquad (2.14)$$

because

$$\mathcal{L}(f(x,t)) = \int dt_0 dx_0 \mathcal{L}(G(x,t-t_0;x_0)) S(x_0,t_0) = S(x,t).$$
 (2.15)

⁴ Project number EGEE-III INFSO-RI-222667, http://public.eu-egee.org/.

⁵ Project number EGI-InSPIRE RI-261323, www.egi.eu.

Note that the only contribution to this integral comes when $t = t_0$. In the systems studied here the source is assumed to be constant in time. This is in agreement with the linear description of the problem because the background plasma is kept constant. Thus, this technique should not be used in combination with the inclusion of nonlinear terms (see Sect. 2.2.7) neither for time varying plasmas. Then S(x, t) = S(x) and:

$$f(x,t) = \int dt_0 dx_0 G(x,t-t_0;x_0) S(x_0)$$
 (2.16)

$$= \int dt_0 \int dx_0 G(x, t - t_0; x_0) S(x_0).$$
 (2.17)

Defining

$$H(x, t - t_0) = \int dx_0 G(x, t - t_0; x_0) S(x_0), \qquad (2.18)$$

the distribution function becomes a time integral:

$$f(x,t) = \int_0^t dt_0 H(x,t-t_0) = \int_0^t dt_0 H(x,t_0).$$
 (2.19)

Except for a multiplicative constant, the function H(x,t) is calculated by ISDEP after integrating 10^5-10^6 test particle trajectories and analyzing the results. Furthermore, H(x,t) is the solution to Eq. 2.15 using $S(x,t)=S(x)\,\delta(t)$ as a source term. Finally, with a 1D numerical integration, f(x,t) can be easily found. In fact, for sufficient large times, it is expected that f(x,t) is constant in time, becoming f(x), because of the balance between continuous injection and particle losses (the number of the test particles always goes to zero if the source is a delta in time). Using the Jack-Knife method [10], one can estimate the average and statistical error of any plasma magnitude.

Due to its linear nature, ISDEP cannot provide absolute values of f, so the results are usually presented normalized. Nevertheless, real values can be calculated multiplying f times the incoming flux of particles.

2.2.6 NBI-Blip Calculations

NBI-Blip experiments are plasma discharges in which the NBI heating system is switched on for a small period of time in the discharge duration [15]. This injector pulse, with length $t_B > 0$, is represented mathematically with the Heaviside function in the source term:

$$S(x,t) = S(x) \left(\Theta(t) - \Theta(t - t_B)\right). \tag{2.20}$$

Then, using the formalism introduced in the previous section:

$$f(x,t) = \int dt_0 \int dx_0 G(x, t - t_0, x_0) S(x) (\Theta(t) - \Theta(t - t_B)) = f_1(x, t) + f_2(x, t).$$
(2.21)

The first term in Eq. 2.21 is:

$$f_1(x,t) = \int_{-\infty}^t dt_0 \int dx_0 G(x,t-t_0,x_0) S(x)\Theta(t)$$
 (2.22)

$$= \int_0^t dt_0 \int dx_0 G(x, t - t_0, x_0) S(x)$$
 (2.23)

$$= \int_0^t dt_0 H(x, t - t_0). \tag{2.24}$$

This is the usual procedure to calculate the steady state of $f_1(x, t)$. When t is large, f_1 becomes independent of t. The second term is then:

$$f_2(x,t) = -\int_{-\infty}^t dt_0 \int dx_0 G(x,t-t_0,x_0) S(x) \Theta(t_0-t_B)$$
 (2.25)

$$= -\int_{t_B}^t dt_0 \int dx_0 S(x, t - t_0, x_0) S(x)$$
 (2.26)

$$= -\int_{t_B}^t dt_0 H(x, t - t_0). \tag{2.27}$$

Adding both expressions together:

$$f(x,t) = f_1(x,t) + f_2(x,t)$$
(2.28)

$$= \int_0^t dt_0 H(x, t - t_0) - \int_{t_B}^t dt_0 H(x, t - t_0)$$
 (2.29)

$$= \int_0^{t_B} dt_0 H(x, t - t_0). \tag{2.30}$$

Notice that it is implicit in the equations that $t_0 < t$. Keeping this in mind, two extreme cases are:

- \bullet $t_B = 0 \Rightarrow f(x,t) = 0.$
- $t_B = t \implies f(x, t) \rightarrow f_1(x, t)$, the very same one from previous section. When t_B is very large, then f(x, t) = f(x).

2.2.7 Introduction of Non Linear Terms

The physical description of the plasma implemented in ISDEP is a linear theory so, in principle, the background plasma is not modified. But here we propose a method to modify the background profiles, i.e. including some non-linearities. As of yet, only modifications in the background temperature are considered through

an iterative process. The developed procedure can be applied to the density or any quantity estimated as a moment of the distribution function.

For the test particles ensemble, the temperature profile is taken to be the average kinetic energy in an interval of $\Delta \rho = 0.1$ centered in ρ at a time t: $v^2(\rho, t)$. Let q_i be the quotient of the average kinetic energy in the ith iteration (v_i^2) and the original energy profile (v_0^2) :

$$q_i(\rho, t) = \frac{v_i^2(\rho, t)}{v_0^2(\rho)}. (2.31)$$

Then, in the iteration i + 1 we take as temperature the initial profile, multiplied by q_i :

$$T_{i+1}(\rho, t) = T_0(\rho, t) q_i(\rho, t).$$
 (2.32)

Since the coordinates (ρ, t) are discretized, a linear interpolation is done to obtain $T(\rho, t)$ at arbitrary position and time. We stop iterating when $T_{i+1}(\rho, t) = T_i(\rho, t)$ within error bars, which is the final self-consistent profile. This method has been used in [16] and will be shown in Sect. 2.4. An example of this procedure can be found in Fig. 2.2, where the test particle energy profile is plotted for a simple tokamak with ICRH heating assuming a Gaussian power deposition profile. In the figure, the energy profile increases due to the external energy input and converges to a stable value after 6 iterations.

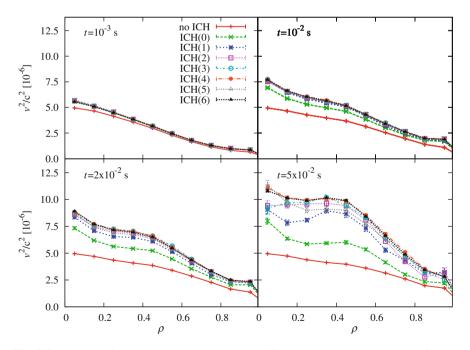


Fig. 2.2 Example of the iterative procedure. We modify the background temperature of a test tokamak with ICRH. The profile converges after 6 iterations

2.3 Benchmark of the Code

The *benchmark* of ISDEP is performed in different tests to check the validity of the results presented in this thesis and related works. First, the guiding center motion without collisions is compared with another orbit code [17] with a nice coincidence of the results. Then the collision operator is tested by estimating the energy slowing down time and comparing it with the standard theory. Finally, the particle diffusion in a circular tokamak geometry is compared with the one estimated by the code MORH (Monte-Carlo code based on Orbit following in the Real coordinates for Helical devices) [7].

In the first step a proton trajectory in the Stellarator TJ-II (see Chap. 4 for more details on the device) is compared with the calculated by means of the code used in [17]. Both trajectories start at the same initial point and for the first times the agreement is good, as can be seen in Fig. 2.3. After some toroidal turns around TJ-II the numerical errors in the interpolation of **B** accumulate and the trajectories start to differ. These results show that this module of ISDEP is validated.

The collision operator is validated in a small circular tokamak with characteristics $R_0 = 1 \text{ m}$, a = 0.2 m, $B \sim 1 \text{ T}$. We consider flat profiles to avoid the influence of the transport, and only one background species ($T_i = 100 \text{ eV}$, $n_i = 10^{20} \text{ cm}^{-3}$). A population of test particles with $T(t = 0) \neq T_i$ is evolved with ISDEP in velocity

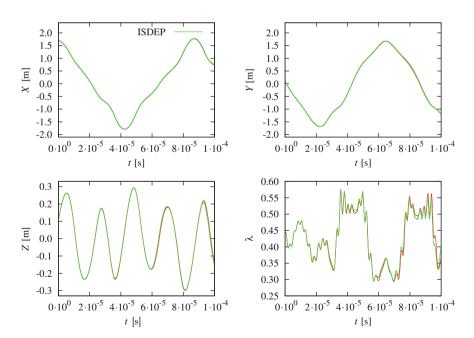
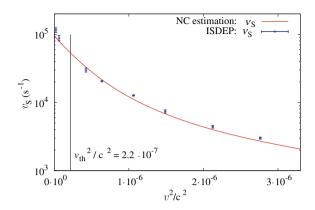


Fig. 2.3 Same trajectory in TJ-II calculated with ISDEP (*green line*) and the code in [17] (*red line*). The initial point is $(x, y, z, v^2, \lambda) = (1.7, 0.1, 0.1, 10^{-6}c^2, 0.44)$. The energy is conserved in all the trajectory

Fig. 2.4 Comparison of the energy slowing down frequency v_S calculated with ISDEP and the NC prediction. The vertical line corresponds to the ion thermal velocity



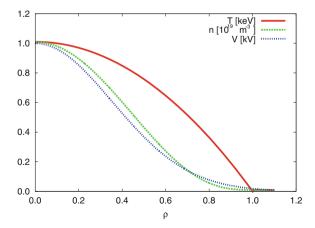
space but not in position. In this way the effect of the collision operator is isolated. These test particles tend to thermalize with certain frequency depending on the initial temperature. Fitting the test particle temperature with $T(t) = T_i + Ae^{-t/\nu_S}$ we can calculate the slowing down frequency and compare with the theory [18]. The theoretical expression of ν_S is:

$$\nu_S = \frac{8\pi e^4 n \ln \Lambda \Psi(x)}{m^2 v^3},\tag{2.33}$$

with the notation of Sect. 1.3.2. A good agreement between our calculations and the theory is found, as can be seen in Fig. 2.4, so we also consider the collision operator validated.

As a final test, both ISDEP and the Monte Carlo code MORH [7] are adapted to the small tokamak used here, but with more realistic profiles and including a radial electric field (see Fig. 2.5). In order to include 3D features a small ripple (1%) is considered, following [19] (this will also be used in Chap. 3). In addition, test particles collide with ions and electrons of the background plasma, taking $T_i = T_e$, $n_i = n_e$.

Fig. 2.5 Plasma profiles of the tokamak used in the *benchmark*



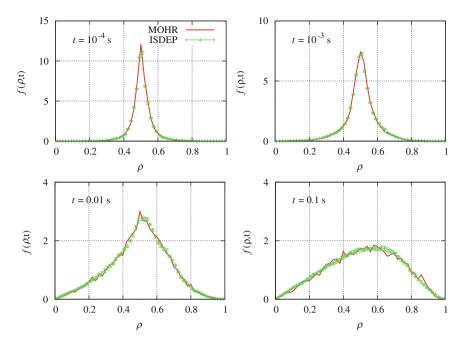


Fig. 2.6 Diffusion of particles in a circular tokamak geometry calculated with ISDEP (*green*) and MORH (*red*). The initial state in both cases is $f(\rho, t = 0 \text{ s}) = \delta(\rho - 0.5)$

In both simulations a population of test particles is launched from $\rho=0.5$ in position and with a Maxwellian distribution in velocity space. The 1D test particle distribution function $f(\rho,t)$ is plotted in Fig. 2.6 for several times, comparing the results of both codes. Also the average radial velocity $\langle v_\rho \rangle$ and the persistence P(t) are plotted in Fig. 2.7. The persistence is defined as the fraction of surviving particles. The two codes present a general good agreement. In Fig. 2.6 ISDEP and MORH reproduce the same dynamics of $f(\rho,t)$, both in the width and in the asymmetry. The differences in v_ρ are due to the different integrators used in the two codes, but they are not statistically significant. The accumulation of numerical errors cause a discrepancy in the persistence for t>0.01 s (see Fig. 2.7). The particle loss conditions are much more sensitive to numerical errors than other quantities of the plasma. The average radial velocity calculated with ISDEP is compatible with MOHR, although it is a very noisy quantity (Fig. 2.7).

As a conclusion, we consider that the ISDEP code is benchmarked.

2.4 Overview of Previous Physical Results

Previously to the elaboration of this thesis, ISDEP has been already used in fusion science for the following purposes.

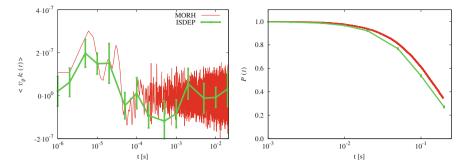


Fig. 2.7 Average radial velocity and test particle persistence calculated with ISDEP (green) and MORH (red)

2.4.1 Thermal Ion Transport in TJ-II

ISDEP has been mainly applied to the TJ-II stellarator [20]. A first work calculating the transport of thermal ions in ECRH plasmas was published in [21]. The thermal ion transport in absence of ion-electron collisions was calculated in that paper, where the violation of the Neoclassical local ansatz was explicitly shown. Additionally, this work estimated the poloidal accumulation of particles and deviation of the test-particle distribution function from de Maxwellian. From these data, a first estimate of the ion contribution to the bootstrap current was provided.

2.4.2 CERC and Ion Confinement

A particular effect, known as the Core Electron Root Confinement (CERC) was simulated in [16], exploring its influence on ion confinement. CERC means the enhancement of the electron heat confinement with the onset of a strong positive radial electric field. Collisions with electrons and the self consistent scheme for plasma temperature modification was implemented here with a complex workflow on the Fusion Virtual Organization of the EGEE Grid. The conditions of the plasma before and after the transition to CERC were simulated. The variation of the radial electric field and the rising of the electron temperature were the ingredients required to reproduce the experimentally observed rise of the ion temperature.

2.4.3 Violation of Neoclassical Ordering in TJ-II

Non-diffusive features of the radial transport in TJ-II can be found in [22], showing that even this linear collisional model is enough to find non-diffusive transport in plas-

mas. The radial transport was estimated for ions at different radial locations and different plasma regimes. A rough estimate of the Hurst exponent (which quantifies the diffusivity of transport) was extracted from the simulations. The local ansatz was shown to be approximately fulfilled for plasmas heated by Neutral Beam Injection (NBI).

2.4.4 Flux Expansion Divertor Studies

The last previous paper on TJ-II included a detailed study of escape particles and divertor effects [23]. The 3D fluxes on the plasma wall were calculated in several configurations in order to exploit their potential as flux expansion divertor. The toroidal and poloidal resolution available in ISDEP was a key factor in the proposal of a new divertor at TJ-II.

References

- 1. Boozer AH (2005) Rev Mod Phys 76:1071
- 2. Beidler C et al (2011) Nucl Fusion 51:076001
- 3. Hirshman S et al (1986) Phys Fluids 29:2951
- 4. Allmaier K, Kasilov S, Kernbichler W, Leitold GO (2008) Phys Plasmas 15:072512
- 5. Tribaldos V (2001) Phys Plasmas 8:1229
- 6. Lotz W, Nührenberg J (1988) Phys Fluids T31:2984
- 7. Seki R et al (2010) Plasma Fusion Res 5:014
- Kloeden PE, Platen E (1992) Numerical solution of stochastic differential equations. Springer-Verlag, Berlin
- 9. Teubel J (1994) Monte carlo simulations of NBI into the TJ-II helical axis stellarator. Max planck institute fur plasmaphisik. 4/268, Germany
- 10. Amit D, Martin-Mayor V (2005) Field theory the renormalization group and critical phenomena, 3rd edn. World Scientific Publishing, Singapore
- 11. Castejón F et al (2008) Comput Inf 27:261
- 12. Benito D et al (2008) In: Proceedings for 2008 ibergrid meeting, Porto, Portugal, p 273
- Antolí B et al (2007) In: Proceedings of the CEDI, II congreso espanol de informática conference, Zaragoza, p 523
- 14. Murakami S et al (2006) Nucl Fusion 46:S425
- 15. Osakabe M et al (2010) Plasma Fusion Res 5:014
- 16. Velasco J et al (2008) Nucl Fusion 48:065008
- 17. Castejón F et al (2006) Fusion Sci Technol 50:412
- 18. Huba J (2009) NRL plasma formulary. Taylor and Francis, USA
- 19. Boozer A, Kuo-Petravic G (1981) Phys Fluids 24(5):851
- 20. Alejaldre C et al (1990) Fusion Technol 17:131
- 21. Castejón F et al (2007) Plasma Phys Controlled Fusion 49:753
- 22. Velasco J, Castejón F, Tarancón A (2009) Phys Plasmas 16:052303
- 23. Castejón F et al (2009) Nucl Fusion 49:085019

Chapter 3 3D Transport in ITER

3.1 Introduction

The International Tokamak Experimental Reactor (ITER) [1] is an international project devoted to prove the feasibility of the thermonuclear fusion as a new energy source. It will be the largest fusion device in the world and the first one to control D-T fusion reactions. Although it is not designed to produce electricity it is expected to produce 5–10 times the energy needed to heat the plasma. Typical values for the injected power are \sim 75 and \sim 500 MW for the fusion power produced.

ITER implies a great development in engineering and industry: remote handling, material resistance, control systems, tritium breeding, neutron shielding, etc. The complexity of this device can be inferred from Fig. 3.1. It is being built at Cadarache (France) and will produce its first plasmas in 2020, although the exact date depends on the invested money and, hence, on the economical situation. This device will be the largest tokamak ever built, overcoming the performance of all existing tokamaks.

ITER is a tokamak fusion reactor. The magnetic field in these machines has two main sources. The most important source is the set of toroidal field coils, responsible of $\sim 90\,\%$ of the total magnetic field. In ITER there are 18 Li-Nb superconducting toroidal coils, refrigerated by liquid He, that create a $B_{\varphi}\sim 6\,\mathrm{T}$ magnetic field. The central superconductor solenoid induces an intense current in the plasma: $I_P=15\,\mathrm{MA}$. As a consecuence, the plasma itself creates a poloidal magnetic field: $B_{\theta}\sim 1\,\mathrm{T}$. Figure 3.2 shows the direction of these components and the resulting helical magnetic field. In addition to this two sources, a small vertical field is created by a set of circular coils for MHD stabilization purposes. The result is a 2D configuration with a characteristic D shaped plasma (see Fig. 3.3).

The plasma parameters in ITER will be outstanding. In a standard scenario the density can be $n \sim 10^{20} \, \mathrm{m}^{-3}$, the temperatures around $10^4 \, \mathrm{eV}$ and the plasma volume of $V \sim 800 \, \mathrm{m}^3$. The pulses will be very long, $\sim 1 \, \mathrm{h}$, and it is foreseen to have steady state discharges half an hour long.

Several heating methods will be available in ITER: Electron Cyclotron Resonance Heating (ECRH), Ion Cyclotorn Resonant Heating (ICRH) and Low Hybrid Current

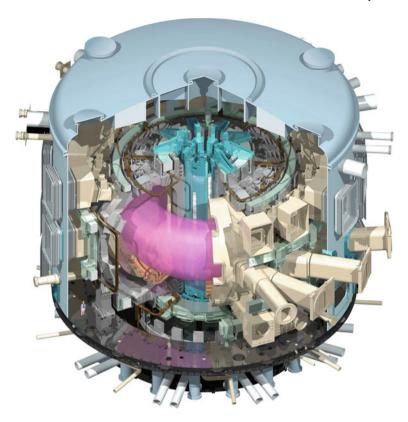


Fig. 3.1 ITER representation. The torus is inside a cryostat, where 18 superconducting toroidal field coils and 6 vertical field coils produce the confining magnetic field. The main parameters of the device are: $R_0 \sim 6.5 \,\mathrm{m}$, $a_0 \sim 2 \,\mathrm{m}$, $T \sim 20 \,\mathrm{KeV}$, $n \sim 10^{20} \,\mathrm{m}^{-3}$. There is a person in the lower left part of the machine, giving an idea of the size of this huge device. *Source* www.iter.org

Drive (LHCD) [2]. It is not clear whether ITER would have Neutral Beam Injection (NBI) in its first stage, due to budget reductions.

In this chapter we will study a particular effect in a standard MHD equilibrium. Most of the literature, models and codes concerning ITER transport consider toroidal symmetry in the device, but in the real machine this symmetry will be broken. The toroidal asymmetry in the system is called *toroidal magnetic ripple*. This perturbation is caused by the finite number of toroidal field coils and the magnetic response of the Test Blanket Modules (the bricks that form the inner part of the vacuum vessel). ¹

The study of the influence of the ripple on the plasma is important because it may modify the transport parameters. Since ISDEP is a 3D code, one can solve the collisional transport and compare the results within and without magnetic ripple.

¹ In fact, ripple is a term that refers to the variation of the magnetic field modulus. There are two other ripples in fusion devices: the poloidal ripple, responsible of the banana orbits, and the helical ripple in stellarators.

3.1 Introduction 49

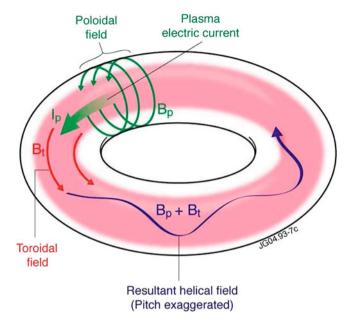


Fig. 3.2 Tokamak scheme. In a tokamak the external coils and the plasma current create the toroidal and poloidal magnetic fields respectively, resulting in a helical field on a magnetic surface. *Source* www.jet.efda.org

In this case the test particle distribution represents the whole plasma population in these simulations. Several simulations of the collisional ion transport in ITER are performed comparing the results obtained for different ripple intensities. It will be shown that the ripple, even for small values, has a non negligible effect on transport and confinement properties.

The remaining part of this chapter is organized as follows: firstly, we discuss the 3D ITER model in Sects. 3.2 and 3.3 we show the main numerical results and in Sect. 3.4 we present the conclusions. Most of the CPU time was provided by the Ibercivis [3] Volunteer Computing Platform.²

3.2 The ITER Model

ISDEP needs a background magnetic equilibrium and plasma profiles to integrate the ion trajectories. The terms that appear in the drift velocities and on the collision operator depend on this quantities.

The 2D ITER magnetic configuration was calculated using the HELENA MHD equilibrium code [4] which is integrated in the CRONOS suite of codes [5]. Then the

² www.ibercivis.es.

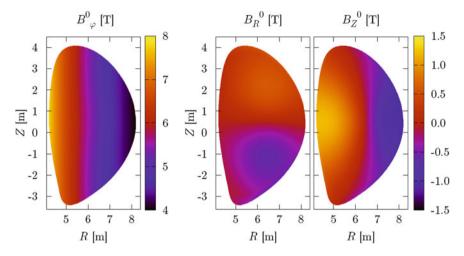


Fig. 3.3 ITER 2D magnetic field (no ripple considered) in cylindrical coordinates: $\mathbf{B} = \mathbf{B}_{\varphi} + \mathbf{B}_{R} + \mathbf{B}_{Z}$. Eighteen superconducting coils create this strong toroidal field (4 T < B_{φ} < 8 T for 4 m < R < 8 m). This magnetic field is procured by the equilibrium code HELENA

ripple is introduced as a small perturbation. In this model the unique cause for the ripple is the finite number of toroidal field coils. Let ${\bf B}^0(R,Z)$ be the 2D magnetic field in cylindrical coordinates (R,Z,φ) , provided by HELENA (see Fig. 3.3). Following Ref. [6], the magnetic field and the scalar magnetic potential in a plasma confined by a set of N_c circular coils are:

$$\Phi(R,\varphi) = \frac{\mu_0 I}{2\pi} \left(\varphi + \left(\frac{R}{R_r} \right)^{N_c} \frac{\cos N_c \, \varphi}{N_c} \right), \quad \mathbf{B} = \nabla \Phi. \tag{3.1}$$

Then the magnetic field is:

$$B_{\varphi} = \frac{\mu_0 I}{2\pi R} \left(1 - \left(\frac{R}{R_r} \right)^{N_c} \sin N_c \varphi \right)$$

$$= B_{\varphi}^0 \left(1 - \left(\frac{R}{R_r} \right)^{N_c} \sin N_c \varphi \right), \qquad (3.2)$$

$$B_R = \frac{\mu_0 I}{2\pi R} \left(\frac{R}{R_r} \right)^{N_c} \cos N_c \varphi$$

$$= B_{\varphi}^0 \left(\frac{R}{R_r} \right)^{N_c} \cos N_c \varphi. \qquad (3.3)$$

Note that in the expressions above **B** is created by the toroidal field coils, so it has no poloidal component and if the ripple is zero $\mathbf{B} = B\hat{\varphi}$. We have separated

3.2 The ITER Model 51

conveniently the axisymmetric part of **B** and the ripple-dependent part. The parameter R_r gives the strength of the ripple and I provides the intensity of the total magnetic field. In this model, the smaller R_r , the larger the perturbation. Usually we take values of R_r close to 10 m to have ripples of a few percents of intensity and when $R_r \to \infty$ the ripple tends to zero.

The 2D ITER magnetic field is extended to a 3D magnetic field with ripple using this sinusoidal perturbation. As has been said before, the number of coils in ITER is $N_c = 18$ and, finally, the perturbed magnetic field is:

$$B_R(R, Z, \varphi) = B_R^0(R, Z) + B_{\varphi}^0(R, Z) \left(\frac{R}{R_r}\right)^{N_c} \cos N_c \, \varphi,$$
 (3.4)

$$B_Z(R, Z, \varphi) = B_Z^0(R, Z),$$
 (3.5)

$$B_{\varphi}(R,Z,\varphi) = B_{\varphi}^{0}(R,Z) \left(1 - \left(\frac{R}{R_{r}} \right)^{N_{c}} \sin N_{c} \varphi \right). \tag{3.6}$$

The toroidal flux and, hence, the effective radius are also modified in this model in a similar way as the magnetic field:

$$\Psi(R, Z, \varphi) = \int \mathbf{B} \cdot d\mathbf{S}_{\varphi}$$

$$\approx \Psi_{o}(R, Z) \left(1 - \left(\frac{R}{R_{r}} \right)^{N_{c}} \sin N_{c} \varphi \right), \tag{3.7}$$

$$\rho(R, Z, \varphi) = \rho_o(R, Z) \sqrt{1 - \left(\frac{R}{R_r}\right)^{N_c} \sin N_c \varphi}.$$
 (3.8)

We will perform several simulations with ISDEP for different configurations, scanning R_r , the ripple parameter. The criteria we use to denote the ripple intensity is the strength of the ripple in the border of the plasma in the low field side.

The axisymmetrical case and five different ripple intensities have been chosen: (0, 1, 2, 3, 5 and 10%), corresponding to

$$R_r[m] = (\infty, 10.85, 10.43, 10.21, 9.92, 9.55).$$
 (3.9)

Its toroidal maximum is plotted in Fig. 3.4 (right, downwards) versus the major radius, showing that the ripple is more significant for the outer positions of the torus, where the toroidal field coils are well separated.

The radial profiles of the plasma (n, T_i, T_e, V) are plotted in Fig. 3.4 (right, upwards) as functions of the effective radius ρ . Only electrons and one ion species (protons) compose the plasma. The ion and electron temperatures are equal in this equilibrium. HELENA cannot calculate the electrostatic potential, so we estimate it using the simplest MHD approximation and the perfect gas equation: $V[V] \approx T[eV]$ [7]. In principle, in this 3D tokamak the transport should not be ambipolar anymore,

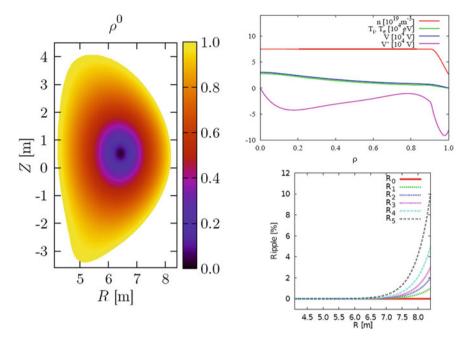


Fig. 3.4 Unperturbed effective radius ρ^0 (*left*), 1D plasma profiles (*right*, *up*) and ripple strength (*right*, *down*). The magnetic axis is located at R = 6.42 m. The density profile is almost constant and the ion and electron temperatures are equal. The electric field is $\mathbf{E} = V'(\rho)\nabla\rho$. The labels $(R_1, R_2, R_3, R_4, R_5)$ denote the ripple intensity, corresponding to (0, 1, 2, 3, 5, 10%) respectively

since the axisymmetry is broken by the presence of the ripple. One has to consider the difference between ion and electron fluxes. As the last one is unknown, a sensitivity study with respect to the electric potential is performed in Sect. 3.3.4.

3.3 Numerical Results

The use of a code like ISDEP instead of the standard neoclassical transport codes is mandatory since the plasma under study is in the banana or low collisionality regime [8], as will be shown below. This fact casts doubts on the validity of the standard NC theory in ITER. The violation of the NC assumptions has been studied numerically [9] in TJ-II.

The system of 5 SDEs formed by Eqs. (1.34), (1.35) and (1.36) in Chap. 1 describes the motion of ions embedded in a thermal bath in a 3D tokamak geometry using the guiding-center approximation. Recall that we do not consider turbulent effects.

In our simulation, the initial state of the particles follows $n(\rho)$ in real position, is locally Maxwellian in velocity according to $T_i(\rho)$ and uniformly distributed in the pitch angle. When a particle reaches the last closed magnetic surface $(\rho = 1)$ we consider that it escapes the plasma and stop the simulation for that particle.

3.3 Numerical Results 53

With these plasma conditions the thermal ions have a mean free path $\sim 10^4$ m $\gg qR \sim 25$ m, being q the safety factor of the magnetic configuration. Since the bounce frequency ($\omega_b \sim 10^5 \, {\rm s}^{-1}$) is also much larger than the parallel collision frequency ($\nu_{||} \sim 10^2 \, {\rm s}^{-1}$) the ions are in the banana regime [8]. ISDEP works properly in this regime, since no approximation is made in the poloidal or radial excursions of the particles. Several Neoclassical codes may fail in this regime because the Neoclassical ordering can be violated.

ISDEP integrates a sample of proton trajectories and extracts statistical information of the ensemble. As has been stated above, most of the CPU time (\approx 2/3) was taken from the Ibercivis computing desktop grid, which is a recently developed volunteer computing platform based on Berkeley Open Infrastructure for Network Computing (BOINC). The ISDEP code had to be modified in order to fulfill the requirements of the Ibercivis Cluster. As an example, the RAM memory is limited to \sim 400 MB and all the simulations are split in small jobs less than 30 minutes long. Additional computer resources have been provided by the Fusion Virtual Organization in the EGEE Project and the EULER cluster at CIEMAT.

The numerical method chosen is a 2nd order method for SDEs (see Eq. (1.88) and Ref. [10]). With $\Delta t = 5 \cdot 10^{-8}$ s one trajectory takes an average of 17 minutes in a single CPU, and we use around 125,000 trajectories for each simulation to reach our precision requirements. Making use of the fact that ITER has 18 periods, we can increase the number of samples, having the equivalent of 18×125 , 000 trajectories. The computing time employed in this work is equivalent to 30 years in a single CPU. With the number of trajectories chosen, the statistical errors in the measurements are larger than the errors induced by the numerical integration. The time discretization Δt chosen ensures that the CPU per trajectory does not surpass the Ibercivis \sim 30 min limit.

We divide the numerical results in three groups: results on ion confinement time, escape points distribution and results on radial fluxes and velocity distribution.

3.3.1 Confinement Time

The ion confinement time is the average lifetime of an ion in the plasma. It is measured using the persistence of the test particle population, i.e. the fraction of surviving particles as a function of time, denoted by P(t). The persistence of the test particles is plotted in Fig. 3.5 (left) for the different values of the ripple (see Fig. 3.5 (right) for the color scale).

It is possible to estimate the particle confinement time, τ , from the persistence of test particles, assuming that the decay of the persistence with time is exponential $(P(t) = e^{-t/\tau})$. Nevertheless, the fit to the exponential fails the χ^2 test [11] because P(t) shows strong deviations from the purely exponential.³ We need to change the exponential definition of this characteristic time to a new definition that shows the different time scales that appear in the system.

³ In these fits the χ^2 per degree of freedom (dof) is around 10^3 , when it should $\chi^2/dof \sim 1$ with deviations of order $\sqrt{2/dof}$ to be a correct fit.

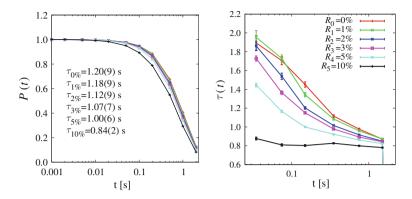


Fig. 3.5 Persistence of the test particles and estimation of the average confinement time (*left*). The statistical error in the fit to purely exponential decay is indicated in parenthesis. On the right plot, the evolution in time of the confinement time (Eq. 3.10) is plotted for different ripple intensities

Let us start defining a time dependent confinement time such that $P(t) = e^{-t/\tau(t)}$. We can estimate $\tau(t)$ as:

$$\tau|_{\frac{t_i + t_{i+1}}{2}} \approx \left(\frac{\ln P_i - \ln P_{i+1}}{t_{i+1} - t_i}\right)^{-1}.$$
 (3.10)

In Fig. 3.5 (right) it is seen that, in fact, the particle confinement time depends on time, showing the different time scales that appear in our problem. The general behavior is that the ripple tends to reduce the time dependency of $\tau(t)$. This fact can be understood considering that the characteristic loss time is decreased and the transport mechanisms have stronger influence along the whole life of the particle. In the low ripple cases, $\tau(t)$ changes drastically with time and it is reduced to the 50%, while in the large ripple case $\tau(t)$ is almost constant, which shows that the persistence fits better the exponential decay.

It has been numerically studied in Ref. [9] that the collisional transport may present several time scales in stellarators. In this ITER model, Fig. 3.5 (right) shows that for times of the order of the collision time $t \sim \tau_c = 1/\nu_{||} \sim 0.03$ s the transport parameters differ from those obtained when $t \sim \tau$. The parallel collision frequency $\nu_{||}$ is the typical collision frequency considering the parallel movement of the ion [12]. This makes necessary a new definition of the confinement time including all timescales rather than the exponential one. Let us consider the following integrals:

$$I_k = \int_0^\infty P(t)t^k \, \mathrm{d}t, \qquad k \in \mathbb{N}, \tag{3.11}$$

and define a family of confinement times:

$$\tau_k = \frac{I_k}{k \, I_{k-1}}.\tag{3.12}$$

3.3 Numerical Results 55

Fig. 3.6 Comparison of τ and τ_1 . The former is calculated with a fit to $P(t) = e^{-t/\tau}$ and the latter with Eq. (3.12)

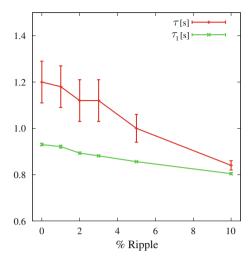


Table 3.1 Comparison of τ and τ_1

Ripple (%)	τ [s]	τ_1 [s]
0	1.20 (9)	0.930 (5)
1	1.18 (9)	0.921 (6)
2	1.12 (9)	0.893 (4)
3	1.07 (7)	0.881(3)
5	1.00(6)	0.856(2)
10	0.84(2)	0.804 (4)

It can be easily shown that if $P(t) = \mathrm{e}^{-t/\tau}$ then $\tau_k = \tau$, $\forall k$. The quantity τ_1 can be interpreted as the average value of t, taking P(t) as the probability measure: $\tau_1 = \langle t \rangle$. As k increases, τ_k is more influenced by the tails of P(t). The simulations performed in this work do not reach the whole tail of P(t) so only τ_1 is considered. The comparison between this new definition of the confinement time and the exponential one is plotted in Fig. 3.6. The error in τ_1 is much smaller than in $\tau(t)$ because it is calculated with an integral, usually less noisy than derivatives. Table 3.1 shows the values of τ and τ_1 for each ripple intensity.

Since the ripple is appreciable for $\rho > 0.5$ (see Fig. 3.4), the external particles are more easily lost, causing the ion average effective radius $\langle \rho \rangle(t)$ to decrease when the ripple increases (see Fig. 3.7).

3.3.2 Map of Escaping Particles

The use of this 5D Monte Carlo code allows one the study of the map of particle losses both in the 3D space and in the 2D velocity space. In particular, it is possible to estimate the hit points on the vacuum vessel together with the velocity components of the lost ions. This can be helpful to predict accumulation of ion losses and avoid

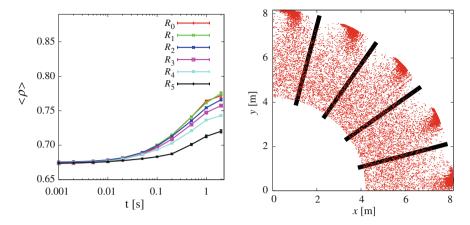


Fig. 3.7 Simulated evolution of the average effective radius (left) and upper view of the escape points for the simulation R_2 (right). The positions of the toroidal field coils are indicated with thick black lines

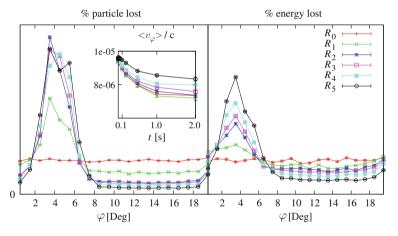


Fig. 3.8 Toroidal distribution of particle losses and fraction of heat load that escapes thought the LCFS. The toroidal field coil is located at 15° , as can be deduced from Eq. (3.1)

vessel deterioration [13] and minimize sputtering [14]. Recall that in this model the vacuum vessel is set at the last closed flux surface (LCFS) but, with the appropriate numerical description, it could be set at any position. Figure 3.7 shows the direction of the escaping particles, viewed from the top of the torus, pointing out the toroidal asymmetry. Not surprisingly, the larger fraction of escaping particles corresponds to the toroidal areas between the toroidal field coils, since at those points the radial drift of trapped particles is larger. This result can be used to estimate the 3D map of heat loads on the vacuum vessel.

Figure 3.8 shows the toroidal distribution of the particle and average energy deposition at the LCFS for all the ripples considered. The latter is estimated assuming that

3.3 Numerical Results 57

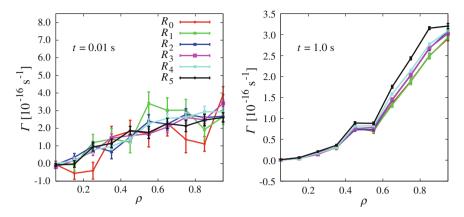


Fig. 3.9 Radial particle fluxes at t = 0.01 s (*left*) and t = 1.0 s (*right*) for different values of the ripple. We can see that, for long enough times, the ripple raises particle fluxes and consequently the confinement becomes worse

all the ion kinetic energy is transferred in the hit point. It is seen that a local maximum of the particles appears and it is toroidally shifted from the position of the coils. This shows that, due to the total plasma current, ions are toroidally drifting. These fluxes give a lower boundary of the thermal ion fluxes that will be suffered routinely by the device walls, since some extra diffusion can be expected from anomalous transport that is not taken into account in ISDEP. Of course neither the flux coming from alpha particles nor the one caused by Edge Localized Modes (ELMs, see [15]) or disruptions are considered here. The distribution of particle losses (Fig. 3.8, left) is more peaked than the energy one (Fig. 3.8, right). Although the ripple degrades the suprathermal ion confinement, it does not affect so strongly the distribution of escape points.

3.3.3 Outward Fluxes and Velocity Distribution

The average outward particle $(\Gamma(\rho))$ and energy $(Q(\rho))$ flux profiles (Figs. 3.9 and 3.10) are also calculated. Both are normalized to the number of particles and all the measurements take place in two times: before the ripple influences the ion motion and around one ion confinement time (around one second, according to Fig. 3.5). In order to increase the statistics and save memory, ISDEP averages the flux profile in the magnetic surface, neglecting any toroidal and poloidal asymmetry. Since in the innermost part of ITER there is no ripple, the fluxes tend to smooth and reduce the local effect of the ripple. The global result is that both fluxes become appreciably larger with the ripple at $t=1.0\,\mathrm{s}$, causing the enhancement of particle losses. The particle flux grows monotonically with ρ for long times due to the fact that no particle sources or sinks are considered inside the plasma. A flattening of the flux is observed

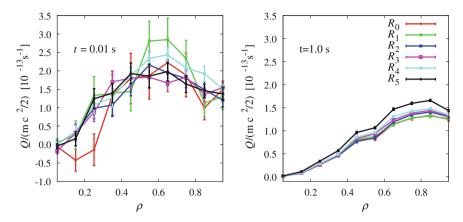


Fig. 3.10 Radial energy fluxes at t = 0.01 s (*left*) and t = 1.0 s (*right*). This quantity shows the scaling of the energy losses with the toroidal ripple

at $\rho \sim 0.5$ due to the combination of the gradients at this plasma zone, where the potential and temperature driven fluxes produce a constant flux. The heat flux is not monotonic showing that the kinetic energy of the particles is modified by the presence of the electric field.

In addition, the features of the velocity distribution of the surviving particles are characterized with the cumulants of the distribution function. The cumulants are normalized moments of the distribution which can be used to explore the non-Maxwellian features. In particular, the Binder cumulant is defined as

$$\kappa = \langle v^4 \rangle / \langle v^2 \rangle^2. \tag{3.13}$$

It measures deviations from the Maxwellian distribution ($\kappa_{\text{Max}} = 5/3$): an excess of supra-thermal particles is indicated by $\kappa > 5/3$, while a lack of them by $\kappa < 5/3$. A deviation of the Maxwellian is observed in all the cases, as can be seen in Fig. 3.11. We identify two causes: the effect of the electric field that tends to accelerate faster particles, since their collisionality is smaller; and particle losses, which depend on the velocity. It can be seen in Fig. 3.11 that κ is reduced close to the plasma edge when the ripple becomes larger. This effect is not surprising, since it means that the low ripple configurations confine better the fast particles than the ones with enhanced ripple. Although alpha particle confinement has not been studied here, indeed the effect of the ripple on these fast particles will be non-negligible.

3.3 Numerical Results 59

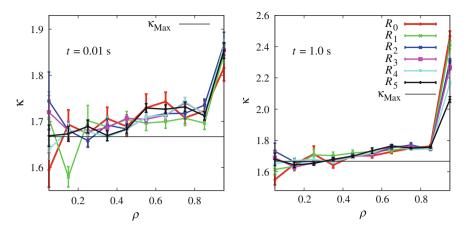


Fig. 3.11 Binder cumulant at t = 0.01 s and t = 1.0 s, showing the deviation from the Maxwellian distribution

3.3.4 Influence of the Electric Potential.

It is well known that the ambipolar condition is satisfied automatically in axysimmetric systems. This means that the electron and ion fluxes are equal, and implies that the electric field is given by diamagnetic effects [16].

In this last section we check the approximation $V[V] \approx T[eV]$ used in Sect. 3.2 and the independence of V with respect to the ripple. Several simulations are performed scanning the $V(\rho)$ profile for the 5% ripple case.

Firstly, a non flat density profile is considered with the expression $\nabla V = \nabla P/n$, being P the plasma pressure [7]. This estimate is valid in the axisymmetric case, in which the collisional transport is ambipolar [17]. Then, the influence of the ripple in the electric potential is studied assuming that V is expressed by:

$$V(R,\rho) = V_0(\rho) \left(1 + \alpha \left(\frac{R}{R_r} \right)^{N_C} \right). \tag{3.14}$$

The profile $V_0(\rho)$ is the original potential and α is a parameter which gives the perturbation intensity. Assuming that the parallel transport is very fast is equivalent to consider that the electrostatic potential is constant on the magnetic surface. So we must take the average in the surface: $V(\rho) = \frac{1}{2\pi} \int d\theta \ V(\theta, \rho)$. Moreover, the circular plasma approximation is supposed to be valid. Then:

$$V(\rho) = V_0(\rho) \left(1 + \alpha \cdot 0.00039 + \alpha \cdot 0.00292 \cdot \rho^2 \right). \tag{3.15}$$

Equation (3.15) is valid up to second order in $a\rho/R_c << 1$, with $a \sim 2$ m the minor radius. The parameter α is varied in the range $\alpha \in [-100, 100]$, considered

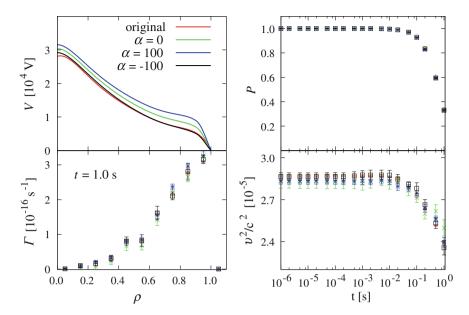


Fig. 3.12 Electrostatic potential, particle flux profile, persistence and kinetic energy time evolution for different potential profiles. The original one is taken from Sect. 3.2. Those labeled with α correspond to Eq. (3.15). In particular, $\alpha=0$ is the original potential profile, but taking into account density variations. As can be seen in the pictures, no significant differences are observed at this level of accuracy

reasonable, but no difference have been found in the transport parameters of the device (see Fig. 3.12). On the whole, we conclude that at this level of accuracy the approximation V[V] = T[eV] is valid, provided that $\partial n/\partial \rho \approx 0$.

3.4 Conclusions

The influence of the toroidal magnetic ripple on the ITER collisional transport has been studied using the kinetic Monte Carlo code ISDEP. We have taken into account the 3D ion collisional transport, starting with a 2D magnetic configuration and introducing the ripple as a sinusoidal perturbation. These studies have shown the enhancement of the radial fluxes and the non-negligible deterioration of the confinement time. At times of the order of the confinement time, the surviving test particles no longer represent the plasma, but they still give a general idea of the evolution of the whole system. The conclusion is that the 3D geometry affects the transport in ITER in an appreciable way.

Even though the modification is not very large, for long pulses it may have a strong influence on the behavior of the plasma. The confinement time is reduced

3.4 Conclusions 61

about 20 % when the ripple reaches 10 %. Large ripples have been studied because, from Eq. (3.1), suppressing half of the coils in the device with 1 % ripple will produce a ripple intensity of \sim 10 %. The effect of the ripple is especially relevant for high energy ions, therefore we expect that the alpha particle confinement will be affected. In this configuration, the fusion alpha particles will have Larmor radius \sim 10 cm, still smaller than the typical scale lengths of the plasma profiles. So the scheme presented in this paper would be valid for these test particles, provided that no steeper gradients appears or narrow island chains or turbulent structures are significant.

Beyond the global confinement features, ISDEP is used to calculate other transport properties. Remarkably, the study of particle losses in a 3D geometry is within reach and the computation of flux asymmetries on the wall will be then a simple matter. Besides, this work is a demonstration of the computing opportunities that volunteer computing platforms, such as Ibercivis, offer to Fusion Science.

The use of a code with the ISDEP characteristics is mandatory because the considered ITER plasmas are in the banana regime and, moreover, we are able to estimate the importance of asymmetries and deviations from the Maxwellian distribution caused just by collisional transport.

References

- 1. Shimada M et al (2007) Nucl Fusion 47:S1
- 2. Gormezano C et al (2007) Nucl Fusion 47:S285
- 3. Benito D et al (2008) In: Proceedings for 2008 ibergrid meeting, Porto, p 273
- Huysmans (G) CP90 conference conference on computational physics. World Scientific, Singapore, p 371
- 5. Basiuk V et al (2003) Nucl Fusion 43:822
- 6. Boozer AH (2005) Rev Mod Phys 76:1071
- 7. Goldston RJ, Rutherford PH (1995) Introduction to plasma physics. Taylor and Francis, London
- 8. Hazeltine RD, Meiss JD (2003) Plasma confinement. Dover Publications, USA
- 9. Velasco J, Castejón F, Tarancón A (2009) Phys Plasmas 16:052303
- Kloeden PE, Platen E (1992) Numerical solution of stochastic differential equations. Springer-Verlag, Berlin
- Press WH, Teukolsky SA, Vetterling WT, Flannery BP (1992) Numerical Recipies in C. Cambridge University Press, Cambridge
- 12. Huba J (2009) NRL plasma formulary. Taylor and Francis, USA
- 13. Federici G et al (2001) Nucl Fusion 41:1967
- 14. Eckstein W (1997) J Nucle Mater 248:1
- 15. Pankin AY et al (2006) Nucl Fusion 46:403
- 16. Hirshman SP et al (1986) Phys Fluids 29:2951
- 17. Hinton FL, Hazeltine RD (1976) Rev Mod Phys 48:239

Chapter 4 Simulations of Fast Ions in Stellarators

4.1 Stellarators

In Chap. 1 we introduced stellarators as the second major family of fusion devices. Their main features are their current-less plasmas and good stability. They were invented by L. Spitzer in the 50s and the first stellarator was built at the Princeton Plasma Physics Laboratory in the USA.

In stellarators, the whole magnetic field is created by external coils, so there is no need of any external inductor to create the poloidal magnetic field. In this sense they overcome a limitation of the tokamaks, but they do not present toroidal symmetry at all, they always have 3D configurations. Nevertheless, they present a reduced symmetry called the stellarator symmetry. In a stellarator, if (R, φ, Z) is a point on a given magnetic surface and $\varphi \in (0, T/2)$, being T the period of the machine, then the point $(R, T - \varphi, -Z)$ is equivalent to the former. Using this property, the computing requirements of ISDEP are reduced substantially. Additionally, there have been proposed some stellarators that present extra symmetries, like helical or poloidal symmetry, but we will not consider them in this thesis.

Figure 4.1 shows several instances of stellarators, illustrating their symmetry as well as their complexity. Figure 4.2 depicts the stellarator symmetry in a stellarator particularly relevant for us: TJ-II. Along the present Chapter we will use various 2D figures to plot 3D quantities. We represent physical quantities in the usual X and Y axis, and the Z values according to the color-scale located at the right edge of the plot.

Usually stellarators are more stable than tokamaks. The twist of the plasma column along the toroidal circle and the lack of confining plasma current makes ELMS and other instabilities much weaker than in tokamaks. In addition there are no disruptions in stellarators. Density and pulse length are potentially much larger in a stellarator than in a tokamak and the steady state operation is much easier. On the other hand, their 3D nature makes the physics, design, construction and simulation much more difficult than for 2D devices. Because of this, development in stellarators has been slower than in tokamaks.

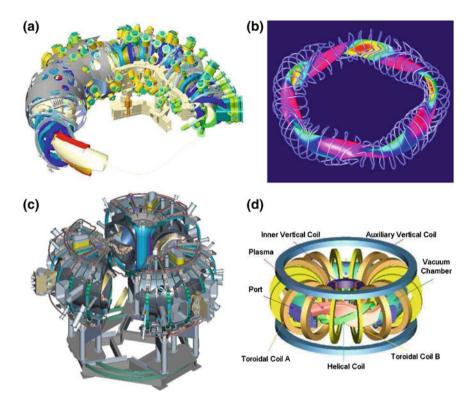


Fig. 4.1 Examples of stellarators: Wendelstein 7-X, currently under construction at the Max Planck Institute, Garching, Germany **a**; coils and plasma scheme of Wendelstein 7-X **b**; NCSX, Princeton Plasma Physics Laboratory, canceled before finished its construction in 2008 **c**; and Heliotron J, Kyoto University **d**. *Source* www.ipp.mpg.de, www.s-ee.t.kyoto-u.ac.jp, http://ncsx.pppl.gov

There exist several kinds of stellarators, depending on the coil configuration. Torsatrons have continuous helical coils, which produce the magnetic field. Heliotrons have, in addition, circular coils to create the vertical magnetic field. Heliacs have circular coils, but their magnetic centers forms a helix around a planar circular coil. Flexible heliacs have a helical coil around the central circular coil, increasing the twist of the plasma column. Finally, helias are the most advanced and optimized stellarators, built with modular (non-planar) coils.

In this chapter we present the improvement and adaptation of ISDEP to calculate the distribution function of high energy ions injected by NBI heating in two different stellarators: LHD and TJ-II. NBI (Neutral Beam Injection) is a plasma heating system that injects a high energy neutral beam ($E \sim 10^4\,\mathrm{eV}$) into the plasma. The fast neutrals are ionized very quickly and become part of the plasma, but with energies one or two orders of magnitude larger than the thermal energy. Fast ions suffer friction with the thermal particles (electrons and ions), losing energy and increasing the temperature of the plasma bulk. In addition, NBI is also a reliable method for

4.1 Stellarators 65

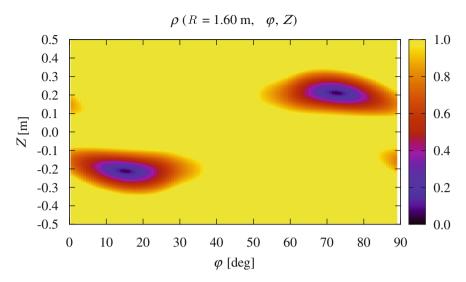


Fig. 4.2 Illustration of the stellarator symmetry in the magnetic surfaces for TJ-II in cylindrical coordinates. In terms of the effective radius ρ , this symmetry is expressed as: ρ (R, φ , Z) = ρ (R, $T-\varphi$, -Z), $\forall \varphi \in (0,T/2)$, $T=90^\circ$. In the figure, R=1.60 m is kept constant. The two big ellipses in the plot appear to be cut, but they are continuous due to the toroidal periodicity of the device. As an example, the magnetic axis ($\rho=0$) is located at $Z\approx-0.2$ m for $\varphi\approx15^\circ$ and in $Z\approx+0.2$ m for $\varphi\approx75^\circ$

plasma fueling, but this can be a disadvantage because the rising of the density could produce plasma collapses [1] if one does not control the plasma recycling. Figure 4.3 shows the basic components of an NBI line.

The remaining part of this Chapter is organized as follows. First we end this Section introducing the two stellarators used for this study. Then, in Sect. 4.2.1, the LHD and TJ-II plasmas and the NBI initial conditions are described. In Sect. 4.2.2 the steady state distribution function is calculated for the fast ion population in the two devices. Sections 4.2.3 and 4.2.4 are devoted to the study of rotation, slowing down and escape points of the test particles. In Sect. 4.3 we present comparisons between the simulations of fast ions and experimental results from fusion devices. Finally we present our conclusions in Sect. 4.4.

4.1.1 LHD

The Large Helical Device (LHD) [2] is a heliotron built in 1998 at the National Institute for Fusion Science in Toki, Gifu, Japan. Nowadays is the largest stellarator in the world, with superconducting coils that confine high density plasmas for long pulses, reaching several minutes. The 10 period magnetic field (\sim 3 T) is created by

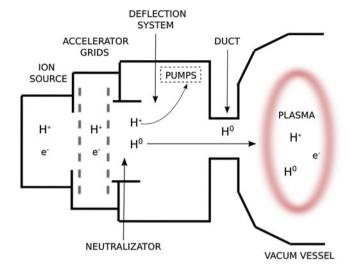


Fig. 4.3 NBI line scheme for positive ions. Ions are generated in the ion source at the beginning of the line and, with an acceleration grid, they increase their energy to tens of keV. Then the ions are partially neutralized and the charged particles deflected to the ion pumps. The high energy neutrals penetrate the vacuum vessel through the duct and then are ionized via collisions with the existent plasma. Other kind of injectors may use H^- in the ion source, with the advantage that the neutralization process is much more effective

two helical coils and six circular vertical field coils. The magnetic axis is almost a circle located at $R_0 \sim 3.6$ m, depending on the configuration, and the plasma minor radius is $a_0 \sim 0.6$ m. Other plasma magnitudes are the temperature $T \sim 10^3$ eV, and density $n \sim 10^{19}-10^{20}$ m⁻³. Figure 4.4 shows the coil configuration and the plasma shape of LHD. In Fig. 4.5 the three components of **B** are plotted for toroidal angle $\varphi = 0^o$ for the R = 3.60 m configuration. Also in Fig. 4.6 we plot the effective radius ρ and the plasma profiles for a Hydrogen equilibrium. The equilibrium is provided by the VMEC code [3], using the vacuum magnetic field. The toroidal variation of the plasma column and the vacuum vessel is sketched in Fig. 4.7.

4.1.2 T.J-II

TJ-II (Tokamak de la Junta-II) [4, 5] is a stellarator built at CIEMAT under the collaboration EURATOM-CIEMAT that started operation in 1998. Its main features can be summarized as follows:

• This flexible heliac has 32 toroidal field coils, four vertical field coils and two central coils that bend the magnetic surfaces. This complex set of coils allows TJ-II to explore distinct magnetic configurations (see Fig. 4.8), usually with a strong magnetic ripple (\sim 20%).

4.1 Stellarators 67

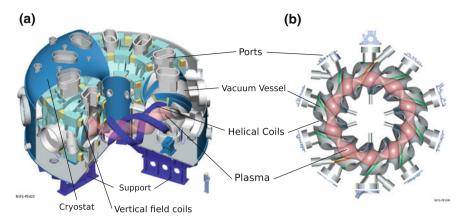


Fig. 4.4 LHD schematic representation. The device (**a**) is surrounded by a cryostat where the helical and circular coils create the magnetic field. The ten period plasma can be appreciated in the picture on the right (**b**)

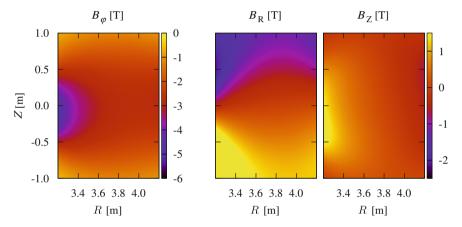


Fig. 4.5 LHD magnetic field $\mathbf{B} = (B_R, B_\varphi, B_Z)$ for $\varphi = 0^\circ$. The magnetic field is counter-clockwise directed and its module can reach $B \sim 3\,\mathrm{T}$ in the plasma column. The regions with $B > 3\,\mathrm{T}$ are located outside the vacuum vessel, very close to the superconducting coils (see Fig. 4.7 for the shape of the vacuum vessel)

- It is a 4-period medium size device ($R_0 = 1.5 \,\mathrm{m}$, $a_0 \sim 0.2 \,\mathrm{m}$) with $B \sim 1 \,\mathrm{T}$ and almost flat rotational transform profile. Figure 4.9 shows the magnetic field in this device and Fig. 4.10 the effective radius and the plasma profiles. In TJ-II the magnetic axis presents strong helical excursions of $\sim 25 \,\mathrm{cm}$. The plasma bean shape and the vacuum vessel shape can be seen in Fig. 4.11.
- The heating power in TJ-II is 2 × 300 kW with ECRH and 2 × 500 kW in the two NBI lines.

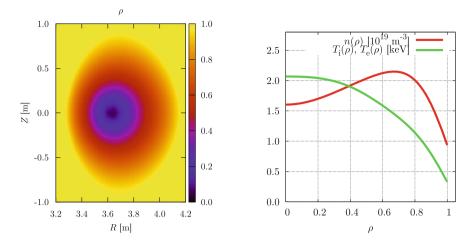


Fig. 4.6 Effective radius in LHD for $\varphi = 0^{\circ}$ (*left*) and 1D plasma density and temperature profiles (*right*). The scrape-off-layer profiles are estimated with an extrapolation of the equilibrium profiles. An exponential decay outside the plasma is assumed for density and temperature profiles

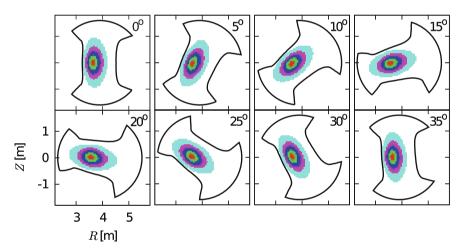


Fig. 4.7 VMEC equilibrium and vacuum vessel for LHD, at different toroidal angles. The corresponding toroidal angle for each chart is indicated on the *upper right corner*. The period in LHD is $T=36^{\circ}$

• In a typical ECRH discharge the temperatures are $T_i \sim 80-100\,\mathrm{eV},\ T_e \sim 1\,\mathrm{keV}$ and densities $n \sim 5 \cdot 10^{18}\,\mathrm{m}^{-3}$, whereas in an NBI discharge the ion temperature may reach 140 eV and the density $\sim 7\dot{1}0^{19}\,\mathrm{m}^{-3}$.

TJ-II discharges are characterized by a high recycling rate because the plasma is very close to the vacuum vessel in the groove (see Fig. 4.11). The recycling and the presence of impurities have been significantly reduced covering the vacuum vessel

4.1 Stellarators 69

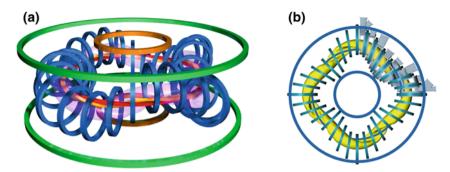


Fig. 4.8 TJ-II schematic. **a** TJ-II Coils and plasma. *Red* central circular. *Yellow* central helical. *Blue* toroidal. *Green* and *Brown* vertical. *Violet* plasma. **b** Upper view of the coils (*blue*), plasma (*yellow*) and one period of the vacuum vessel (*grey*)

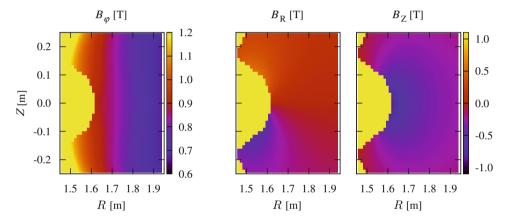


Fig. 4.9 TJ-II magnetic field in cylindrical coordinates for the standard configuration (100_44_64) at $\varphi=0$ °. The yellow half circle near R=1.5 is outside the vacuum vessel

with a lithium layer [6]. The Li wall allowed TJ-II to enter in H-mode regime in 2009 (see below).

Table 4.1 summarizes the main parameters of the two devices.

4.2 Fast Ions in Stellarators

NBI heating plays a very important role in the physics of most fusion devices. The NBI system creates a small population of suprathermal particles in the plasma that have strong influence in the global behavior of the device. If they are confined for sufficient time then they transfer their energy to slower particles and the plasma temperature and density rise. It is indeed a useful method for plasma heating and

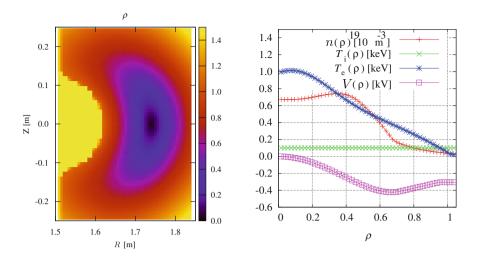


Fig. 4.10 Effective radius in TJ-II for $\varphi=0^\circ$ (*left*) and 1D plasma density, temperature and potential profiles (*right*). These profiles are usual in an ECRH discharge in TJ-II. Note the characteristic bean shape of the TJ-II magnetic surfaces

fueling and can be used for current and momentum drive. The heating and the current drive efficiency depend strongly on the fast ion transport characteristics, determined by the plasma profiles and the magnetic configuration. Most of the plasma transitions from Low confinement regime to High confinement regime (L-mode to H-mode) are driven by the NBI heating system [7]. This transition is not completely understood yet, and it is characterized by a sudden increase of the confinement properties of the device accompanied by a reduction of the turbulence in the plasma edge.

Hence a numerical study of the fast ion distribution function can help to optimize the performance of the NBI heating in a fusion reactor. In the present section, the NBI fast ion distribution function is calculated numerically for LHD and TJ-II stellarators using ISDEP.

The fast ion population is considered as a small perturbation to a static plasma background and its dynamics given by the guiding center motion and collisions with thermal ions and electrons. Chapter 1 summarizes these equations of motion.

Even though fast ions are in the low collisionality regime, the complexity of the magnetic field in 3D devices implies that a numerical solution of the fast ion transport is mandatory. The steady state distribution function is calculated assuming a stationary source with the method described in Sect. 2.2.5. This is a good approximation for the NBI heating in which the injectors launch an almost constant input of neutrals with constant energy spectrum. Two different experimental settings are considered: perpendicular beam injection for LHD and tangential injection for TJ-II.

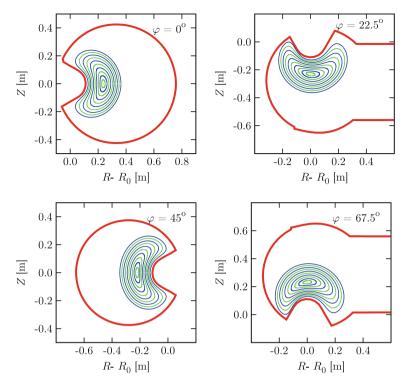


Fig. 4.11 TJ-II magnetic surfaces (green and blue lines) and vacuum vessel (red line). The magnetic axis is a circular helix with $R_0 \approx 1.5$ m. The vertical excursion of the plasma column is quite large in TJ-II, $\Delta Z \sim 50$ cm $\approx 2a$

Table 4.1 Main parameters of LHD and TJ-II: major radius of the magnetic axis, magnetic field at the axis, average minor radius, rotational transform at the plasma boundary and Larmor radius of the fast ions

	LHD	TJ-II
R_0	\sim 3.6 m	~1.5 m
$B(R_0)$	∼3 T	~1 T
a	0.60 m	0.22 m
$\iota(\rho=1)$	1.56	1.46
r_L	0.7 cm	1.7 cm

The Larmor radius corresponds to a proton with energy equal to 30 keV. For LHD the GC approximation is valid since $r_L << a$, but for TJ-II it is uncertain because r_L is only one order of magnitude smaller than a. In discharges with steep plasma profiles finite Larmor radius effects must be included in ISDEP, but if the profile gradients gradients are small it will not be necessary

4.2.1 Ion Initial Conditions

NBI lines inject a neutral beam into the vacuum vessel of the machine. Then the neutrals travel a certain distance in the plasma before being ionized, spreading in space due to collisions with other particles. Since the neutrals energy is very high and the ionization time is very short, their energy is not modified in the ionization process. All these processes are not taken into account in ISDEP, therefore another code must do this task and calculate the initial condition for the fast ion population.

ISDEP was modified to initialize the trajectories according to the output of two fast neutral transport codes, namely HFREYA [8] and FAFNER2 [9]. They are two Monte Carlo codes that estimate the dynamics of fast neutrals inside the plasma, including propagation, ionization and charge exchange. They provide a list of fast ion birth points in the 5D phase space (we use around 10^5 initial points). ISDEP chooses randomly the initial condition $(x_0, y_0, z_0, E_0, \lambda_0)$ from that list. This procedure is known as the bootstrap method in Monte Carlo studies.

The bootstrap method is very useful in orbit codes, like ISDEP, although it only provides a limited number of initial conditions. it is useful because the stochastic evolution of the orbit and the high non-linearities of the equations of motion tend to decorrelate orbits with the same initial point. This decorrelation implies that we can obtain many statistically significant trajectories that start from the same point in phase space.

Although in LHD most of the NBI heating power comes from tangential injection, in this work we simulate fast ions injected perpendicularly by NBI line number 4 (6 MW power). Line 4 is especially valuable for future comparisons with experimental data. The ions are initialized following the distribution function provided by the code HFREYA. The distribution function provided by HFREYA presents three peaks in energy at \sim 36, 18 and 12 keV, as can be seen in Fig. 4.12. The pitch angle distribution function is roughly Gaussian centered close to 0.

In the LHD simulations the electric field is neglected since it is too small to have consequences on the orbits of such fast ions. Figure 4.12 also shows the plasma equilibrium profiles. The main parameters of the device can be found in Table 4.1 for a Hydrogen plasma.

TJ-II is equipped with two tangential injectors that launch neutrals in co and counter directions. We simulate here the neutrals injected tangentially with line number 1 (co-directed to the magnetic field). The birth point locations in phase space are estimated with FAFNER2. TJ-II simulations with ISDEP do take into account the electric field because it is not negligible. Figure 4.13 shows the distribution of the fast ions created from the fast neutrals. In this case the pitch angle distribution is peaked at $\lambda=1$, since we are dealing with co tangential injection. The plasma background (Fig. 4.10) corresponds to the standard magnetic configuration and typical ECRH discharge profiles: $T_i \sim 100 \, \mathrm{eV}$, $T_e \sim 1 \, \mathrm{keV}$, $n \sim 0.6 \cdot 10^{19} \, \mathrm{m}^{-3}$. These conditions are representative of the initial phase of an NBI discharge.

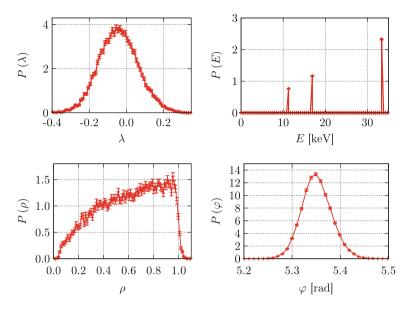


Fig. 4.12 The fast ion initial distribution in LHD for pitch angle, energy, effective radius and toroidal angle, given by HFREYA. The pitch distribution is centered near 0 and the energy presents three peaks. In position space, the distribution grows with ρ and is located toroidally in a small layer \sim 0.1 radians wide

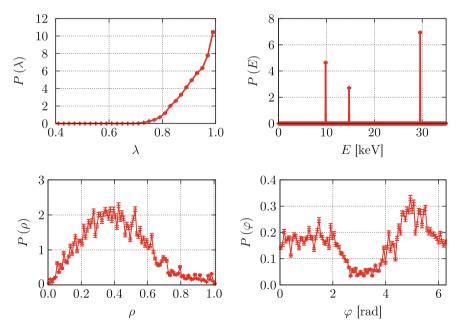


Fig. 4.13 Same as Fig. 4.12, for the case of the TJ-II plasma considered in this work. In this situation, the code FAFNER2 provides the initial fast ion distribution

4.2.2 Steady State Distribution Function

The most general result presented here is the calculation of the fast ion distribution function with ISDEP. Computing the whole distribution function $f(x, y, z, v^2, \lambda, t)$ is very expensive in terms of memory and CPU time, so we average in the poloidal and toroidal angles obtaining $f(\rho, v^2, \lambda, t)$. Then, using the techniques shown in Sect. 2.2.5, the steady state distribution function, $f(\rho, v^2, \lambda)$, is calculated.

The steady state distribution function of the LHD fast ions is plotted in Fig. 4.14 for four radial positions: $\rho=0.15,~\rho=0.45,~\rho=0.65$ and $\rho=0.95$. A sample of the magnitude of the errors can be seen in Fig. 4.15. Around $5\cdot 10^4$ CPU-hours have been needed to achieve errors of $\sim 1\,\%$ in the distribution function. From Fig. 4.14 it is seen that the ions tend to thermalize and spread in velocity space almost symmetrically in $v_{||}$, although some asymmetry is still present due to the initial condition in which $\langle \lambda \rangle < 0$. Traces of the continuous injection of high energy ions are visible at all positions.

In TJ-II the situation is different, as can be seen in Fig. 4.16. The birth points of test particles are located close to the magnetic axis due to the fact that the background plasma density is too low in the edge. Hence there are not many trajectories of fast ions in the outermost part of the plasma. The injection is tangential to the direction of **B**, therefore there are not high negative parallel velocities in the distribution and almost all the fast particles appear for positive pitch. A strong dispersion in the pitch

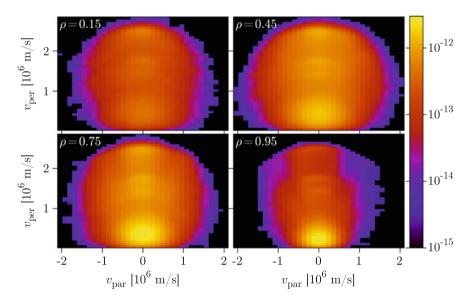


Fig. 4.14 $J(\rho, v_\perp) \cdot f(\rho, v_\parallel, v_\perp)$ for four different radial positions in the steady state for LHD. The statistical errors are small (< 5%) in the maximum and become higher at the tails of the distribution (see Fig. 4.15). $J(\rho, v_\perp)$ is the Jacobian of the transformation from real coordinates to magnetic coordinates

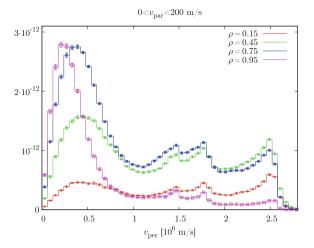


Fig. 4.15 Fast ion distribution function and its statistical error in LHD for $0 < v_{||} < 200 \, \text{m/s}$: $J(\rho, v_{\perp}) \cdot f(\rho, 0 < v_{||} < 200 \, \text{m/s}, v_{\perp})$ for four different radial positions for LHD. Statistical errors are plotted, but they turned out to be smaller than the symbol size, being typically $\sim 5 \, \%$

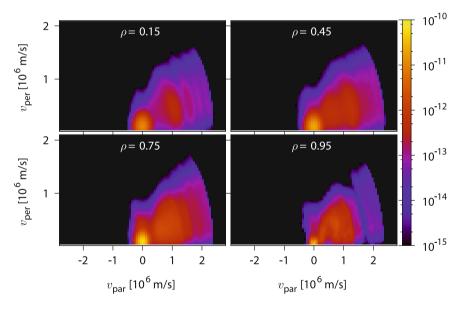


Fig. 4.16 $J(\rho, v_{\perp}) \cdot f(\rho, v_{||}, v_{\perp})$ for four different radial positions in the steady state for TJ-II

angle appears due to deflections with background particles. The thermalization of particles is much less effective in TJ-II than in LHD. Thus, the distribution function significantly departs from the Maxwellian in TJ-II. It is also necessary to consider the effects of radial transport that are taken into account in the code in a natural way. As an example, most of the fast ions that appear at outer positions of TJ-II come from the center of the plasma. Finally, the strong decrease of fast ion density observed at the outermost magnetic surfaces can be understood just considering the direct losses.

4.2.3 Fast Ion Dynamics: Rotation and Slowing Down Time

The study of the toroidal rotation is important because it has strong influence on the confinement. This is specially relevant in tokamaks where the toroidal rotation can play a crucial role for MHD stabilization (see [10] for a review on this topic) and where spontaneous rotation, without any external input of angular momentum, is observed [11]. The current caused by fast ions may contribute significantly to the total plasma current, modifying then the confining magnetic field. Despite of the fact that the toroidal rotation is especially relevant in tokamaks, it is very useful to perform this study in a stellarator where the toroidal rotation is limited and the fast ions are in principle the only momentum source, so it is possible to validate the presented models with experimental data. Moreover, the toroidal rotation in stellarators can also play a relevant role in the plasma stabilization, as has been discussed in Ref. [12], and can also appear spontaneously [13]. The poloidal rotation profile is relevant for the transport, since it has been demonstrated that poloidal sheared flows can be beneficial for the confinement, both in tokamaks and stellarators. This mechanism was predicted theoretically in 1990 [14] and was confirmed experimentally in the DIII-D tokamak [15].

The radial transport, and hence the fast particle confinement, is closely related to the particle average radial velocity. The toroidal, poloidal and radial velocity profiles in the steady state are plotted in Fig. 4.17 for both LHD and TJ-II.

Even though the injection is almost perpendicular for LHD, the toroidal rotation (v_{φ}) is nonzero and presents a strong shear, changing sign twice while moving along the radial direction. The mechanisms that determine this velocity are the initial conditions, the structure of the background magnetic field and the collisionality profiles, in a similar way as the bootstrap current is generated. The poloidal velocity v_{θ} is almost zero in most of the plasma column and becomes negative for $\rho>0.8$. The radial velocity v_{ρ} , proportional to the outward particle fluxes, clearly presents three regions of interest. In the inner region of the plasma it is zero or negative, meaning a very good confinement of fast ions. In the region defined by $0.4 < \rho < 0.8$, $v_{\rho} \sim 1$ m/s so the confinement gets worse. Near the border of the plasma where $\rho>0.8$ the radial transport is higher, showing the effects of ion loses at these positions and a worse confinement of fast ions in the plasma edge.

In the case of TJ-II the results are quite different due to the different characteristics of the device and to the tangential injection. As expected, the average toroidal velocity

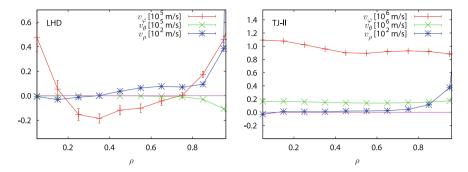


Fig. 4.17 Fast ion toroidal and poloidal rotation and radial velocity profiles for LHD and TJ-II. The toroidal rotation is defined as the velocity component in the azimuthal angle in cylindrical coordinates, whereas the radial and poloidal rotation refer to Boozer coordinates. The two fast ion populations rotate in a different way due to the distinct initial conditions

of the fast ions, v_{φ} , is much higher in TJ-II than in LHD, as can be seen in Fig. 4.17. In this case the high initial parallel velocity is so large that the influences of the structure of the magnetic field and the collisonality are not enough to reduce it substantially. The poloidal rotation v_{θ} is almost constant and the relative change of v_{ρ} along the radius is much smaller than in the LHD case, except in the plasma edge.

The energy decay or slowing down time of the NBI ions is a very important quantity because it is related to the efficiency of the heating system. The shorter the slowing down time, the more efficient the power absorption by the plasma background and the more reduced the fast ion losses. It is defined as the exponential decay time of the initial fast ion energy. After 2–3 slowing down times the beam is thermalized and can be considered as a part of the bulk plasma. The energy slowing down time profile is calculated with the data of $f(t, \rho, v_{||}, v_{\perp})$ from Sect. 4.2.2. An integration gives the average energy profile:

$$E(t,\rho) = \int dv_{||} dv_{\perp} J(\rho, v_{\perp}) f(t, \rho, v_{||}, v_{\perp}) \frac{m(v_{||}^2 + v_{\perp}^2)}{2}.$$
 (4.1)

Assuming that the energy follows an exponential law in time, the slowing down time profile can be found with a fit to the expression:

$$E(t, \rho) = E_{\infty}(\rho) + B(\rho)e^{-t/\tau(\rho)}.$$
(4.2)

In these calculations a standard χ^2 test of fit-goodness shows that the decay is only approximately exponential. Hence we have turned to a model-independent integral estimator of the decay time as we did for the particle lifetime in ITER (Chap. 3). Firstly, the asymptotic energy $E_{\infty}(\rho) = \lim_{t \to \infty} E(t, \rho)$ is found with a fit to Eq. (4.2). Then, the slowing down time profile is given by:

$$\tau(\rho) = \frac{\int dt \left(E(t, \rho) - E_{\infty}(\rho) \right) \cdot t}{\int dt \left(E(t, \rho) - E_{\infty}(\rho) \right)}.$$
 (4.3)

It can be easily shown that if the energy follows an exponential decay law, Eqs. (4.2) and (4.3) provide the same slowing down time. Figure 4.18 also shows the slowing down time profile for the two devices. In order to compare our results with the estimations of the neoclassical theory, we follow [16, 17] to calculate the Spitzer slowing down time:

$$\tau_S = \frac{t_S}{3} \ln \left(\frac{W_b^{3/2} + W_c^{3/2}}{W_f^{3/2} + W_c^{3/2}} \right), \tag{4.4}$$

where W_b and W_f are the beam initial and final energy, and t_S and W_c are:

$$W_{\rm c} = 16.0 \, T_e, \qquad t_S = 6.27 \cdot 10^{14} \frac{T_e^{3/2}}{n_e \ln \Lambda},$$
 (4.5)

with T_e in eV, n_e in m⁻³ and the times in seconds. W_c is known as the critical energy, defined as the energy for which the same energy is transferred from the beam to the background ions and electrons. For beam energies above W_c , more power is transferred to the electrons than to the ions and vice-versa. The time t_S is proportional to the inverse of the collision frequency and $\ln \Lambda$ is the Coulomb logarithm [18]. In LHD the beam energy is close to W_c , but in TJ-II is $\sim 2 W_c$, so electron friction is quite important in TJ-II. The beam final energy is taken to be $W_f = e^{-1}W_b$. In Fig. 4.18 the slowing down time calculated with ISDEP and Eq. (4.4) are plotted. The time τ_S gives the slowing down time for an homogeneous plasma, just taking into account collisions.

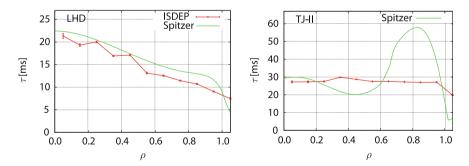


Fig. 4.18 Slowing down time, calculated with Eq. (4.3) and with the Spitzer formula (4.4). The sudden increase of τ_S in TJ-II near $\rho=0.6$ is due to the shape of the density and temperature profiles (Fig. 4.13), which present a strong gradient in that region. The discrepancies are larger in TJ-II, due to the fact that the quotient of the banana width and the minor radius is higher than in LHD

Discrepancies between the two pairs of time profiles can be observed in Fig. 4.18, being stronger for TJ-II than for LHD. These discrepancies can be understood by considering the effect of ion transport in the complex 3D geometry of the devices, especially of TJ-II, which is not taken into account in Spitzer formula. In the ISDEP calculation, the energy slowing down time is computed including all the fast ion dynamics: transport between magnetic surfaces, particle losses and geometrical features, apart from the collisional processes with thermal particles. Specifically, radial transport implied that a fast ion *feels* different plasma temperatures and densities, so the Spitzer local approximation is not valid anymore. This is due to the fact that in TJ-II the relation between the typical banana width and the minor radius is much higher than in LHD, making non-local effects relevant [19].

We may anticipate from Fig. 4.19 (left) that the slowing down process occurs in a similar time scale as fast ion confinement time, meaning that the above referred processes are relevant.

4.2.4 Escape Distribution and Confinement

The main properties of the confinement of fast ions are estimated and shown in this section. The confinement is described by the persistence of the particles, which is a global magnitude, and by the loss cone in velocity space. The persistence of particles is defined as the probability of finding a particle in the plasma after a given time (see [20]), so it provides a measurement of the confinement time of particles. The loss cone is defined as the region of the velocity space where the ions are lost for a given time interval. The reader should notice that the steady state calculations are not needed to obtain these two important characteristics of the confinement of fast ions. The persistence and the loss cones are plotted in Figs. 4.19 and 4.20 for both LHD and TJ-II.

Figure 4.19 shows the time evolution of the persistence and average energy of fast ions in LHD and TJ-II. It is checked again that the curve cannot be fitted by an exponential function according to standard χ^2 test. This means that the confinement presents a strong time dependence (as happened in ITER, Sect. 3.3.1, and in the energy slowing down Sect. 4.2.3), showing at least two different time scales. The big slope in the persistence P(t) at $t \sim 10^{-4}$ s for LHD that is observed in Fig. 4.19 is caused by prompt losses and corresponds to the first part of ion dynamics. Prompt losses are fast ion losses that occur very early because their initial points are in a badly confining region in phase space. Then a second stage appears, when ions suffer the slowing down process, which increases the bulk of the distribution function (see Fig. 4.14). It can also be seen that the prompt losses have not a strong effect in the average kinetic energy. For times $t > 10^{-2}$ s the confinement is severely degraded for the majority of fast ions. The loss cone (Fig. 4.20) evolves in time and becomes wider as the dispersion of fast ions increases. Despite the perpendicular injection, the loss cone presents a strong asymmetry at every time scale. This must be attributed to the particular magnetic structure of the device. The asymmetry is, nevertheless,

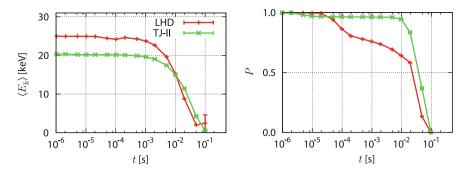


Fig. 4.19 Average energy and persistence of the fast ion population. The persistence is defined as the fraction of surviving ions at a given time. The particle confinement and energy slowing down occur in a similar time scale. The big change in the persistence at $t \sim 10^{-4}$ s is due to prompt losses, larger in LHD due to the perpendicular injection of the neutral beam

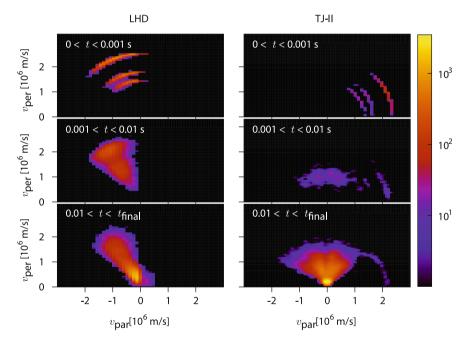


Fig. 4.20 Particle escape analysis for LHD (*left column*) and TJ-II (*right column*). The rows correspond to different time intervals. For each device, histograms of hit points with the vacuum vessel in velocity space are plotted, showing the spreading of the loss cone with time. The relative error in the histograms is $N^{-1/2}$, being N the number of events in the bin. The minimum error in the maximum of the histogram is around 0.5 %

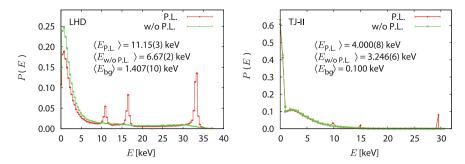


Fig. 4.21 Energy distribution of losses for LHD and TJ-II. The energy spectra is plotted with and without considering prompt losses of the devices. The three peaks above 10 keV make prompt losses important in LHD. In TJ-II the peak near 30 keV is the only non negligible contribution to this effect. Note that all distributions are normalized

softened by diffusion processes in phase space. Due to the different initial conditions (remember the tangential injection in TJ-II), prompt losses are much higher in LHD than in TJ-II. In fact, the former ones represent about 20 % compared with 5 % found in TJ-II. This makes that, differently to what is found in LHD, the persistence in TJ-II presents roughly a single time scale.

The loss cone in TJ-II shows clearly the different character of the injection. Figure 4.20 shows that the effect of pitch angle scattering starts being significant for times of the order of $10^{-3} - 10^{-2}$ s. For longer times the dispersion caused by pitch-angle scattering is much stronger. It is also shown in Fig. 4.20 that the loss cone is extended also to the region of negative parallel velocity due to this effect, showing the appearance of a non negligible amount of ions with negative parallel velocity that finally escape from the plasma.

The energy distribution of losses is plotted in Fig. 4.21. Two probability densities are calculated for each device: taking into account all escaping particles (with subscript P. L.) and removing the prompt losses (w/o P. L). In agreement with the former results, it is seen that the energy prompt losses are much more important for LHD. Moreover, the average energy of the lost particles is almost three times larger in LHD than in TJ-II.

Prompt losses are a wasted fraction of the input power and may damage the device walls if they are concentrated in space. Indeed ISDEP can help to predict and minimize this effect, with the subsequent optimization of the heating system.

4.3 Comparison with Experimental Results

In this section we present a comparison of the numerical results obtained in this Chapter with experimental results from actual fusion devices. A detailed reconstruction of the Compact Neutral Particle Analyzer (CNPA) energy spectra is done in TJ-II

for different plasma profiles of those in Sect. 4.1.2. Then we will compare briefly the slowing down time calculated with ISDEP in Sect. 4.2.3 and the one given by the Fast Neutral Analyzers (FNA) in LHD [21, 22] and the CNPA [23, 24] in TJ-II. Let us start describing the fast particle diagnostics in TJ-II.

4.3.1 Neutral Particle Diagnostics in TJ-II

In all fusion plasmas there is a small amount of neutral atoms or molecules due to atomic reactions between the different plasma species. Plasma-wall interaction (recycling and diffusion in the SOL) and charcge exchange reactions are common causes of the presence of the neutrals. Usually the neutral density is several orders of magnitude below the plasma ions or electron density. Even though the neutral population is neglected in most situations, neutral particle diagnostics are based on charge exchange (CX) reactions of plasma ions with these neutrals. In particular, a fast proton in the plasma can be neutralized with a Hydrogen atom:

$$H_{\text{fast}}^+ + H^0 \to H_{\text{fast}}^0 + H^+.$$
 (4.6)

This is an elastic process, so we can consider that the fast ion velocity is not modified during the neutralization. Thus, the fast ion becomes a fast neutral carrying important information about the original fast ion. Since the fast neutral is not affected by the confining magnetic field, it quickly leaves the plasma and can be detected in the SOL region. This event occurs continuously, leading to a flux of fast neutrals leaving the plasma with the same velocity distribution function as the fast ion population inside the plasma. The outgoing flux of neutral can be attenuated by atomic reactions with the plasma and should be considered in the calculations.

CNPAs are neutral particle diagnostics which measure the incoming neutral flux espectrum as a function of the energy. CNPAs detect the fast neutral flux in the solid angle defined by its line of sight (LOS), so all the physical information that they provide is integrated along this line. We focus on the tangential CNPA system of TJ-II [23]. It is formed by an array of 16 detectors or channels, each one corresponding to a particle energy between $\sim 1 \, \text{keV}$ and $40 \, \text{keV}$. Each channel has a particular width and efficiency associated, which must be considered to reconstruct the fast ion spectra. Figure 4.22 shows the energy channels together with their width and efficiency.

The LOS of the CNPA can be seen in Fig. 4.23 (right). Several quantities of interest are plotted as a function of the distance to the CNPA: effective radius of the plasma, neutral density and inclination of the field lines. The inclination of the field lines, defined as $\cos \xi = -\mathbf{B} \cdot \mathbf{D}/(BD)$, is important to determine the ratio of $v_{||}$ and v_{\perp} of the particles that reach the detector. The vector \mathbf{D} determines the direction and distance along the LOS, starting in the CNPA array. The CNPA array is located approximately tangential to the magnetic field and the LOS passes near the magnetic

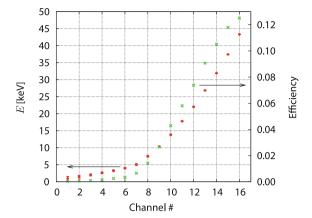


Fig. 4.22 CNPA channels and energy width (errorbars in the *red plot*, usually smaller than the symbols) and efficiency (*green points*). Measurements in the low energy channels should not be trusted because these channels overlap in energy

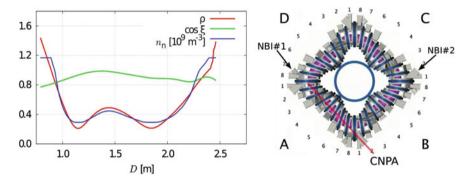


Fig. 4.23 Geometrical scheme of the line of sight of the CNPA in TJ-II and plasma parameters (effective radius, inclination of the *field lines* and neutral density) as a function of the distance from the CNPA along the LOS (D). The LOS is the *red line* that passes through the plasma in the right plot, pointing to NBI#1. In TJ-II the plasma column has a vertical excursion of $\Delta Z \sim 50$ cm every period (90°), so the CNPA LOS does not look straight to NBI#1. For TJ-II, the neutral density profile is obtained from the EIRENE code [25]

axes. Due to its location, it can only measure when NBI line number one (NBI#1) is working.

From Ref. [24], the particle flux to the detector per unit of time in the energy interval ΔE is, for energetic particles with source $S(x, \mathbf{v})$:

$$F(E)\Delta E = A\Omega_s \int_0^{D_{\text{max}}} \exp\left(-\int_0^x \alpha(l) \, dl\right) S(x, \mathbf{v}) \, dx. \tag{4.7}$$

The CNPA array is supposed to be at x=0 and the LOS crosses the plasma in the interval $x \in (0, D_{\text{max}})$. The factors A and Ω_s are the area and solid angle viewed. The integrand in the exponential is called the attenuation factor and will be explained below. Let us start discussing the source term $S(x, \mathbf{v})$. It depends on the fast ion distribution, the Jacobian of the transformation and the fast neutrals birth rate:

$$S(x, \mathbf{v}) = f(x, \mathbf{v}) J(x, \mathbf{v}) n_{\mathbf{n}}(x) \sigma_{CX}(v) v. \tag{4.8}$$

The product $f(x, \mathbf{v}) J(x, \mathbf{v})$ is the fast ion distribution, n_n is the neutral particle density, σ_{CX} is the charge-exchange cross section and v is the fast ion velocity.

The neutral density profile is obtained using EIRENE code [25] for a discharge similar to the ones considered in the experiment. The 1D neutral density profile is obtained by averaging the local three dimensional neutral density in the flux surfaces. The EIRENE code calculates this neutral density, in combination with the transport code Proctr [26]. It takes into account all the relevant atomic physics phenomena together with neutral transport. This estimation implies some uncertainty in the neutral density profile since the local neutral density can vary mainly poloidally due to the presence of the groove of the vacuum chamber. EIRENE is run varying the input parameters in the range defined by their errorbars until the averaged neutral density profile is consistent with the H_{α} emission [27]. Especially, the particle confinement time introduced by EIRENE must be similar to the experimental time.

The exponential factor in Eq. (4.7) is the attenuation coefficient, which takes into account possible reionizations of the fast neutrals before they leave the plasma. It depends on the plasma density and reionization cross sections with protons and electrons in the following way:

$$\alpha(l) = n(l) (\sigma_p + \sigma_e). \tag{4.9}$$

The cross sections σ_{CX} , σ_p and σ_e are functions of the energy and are plotted in Fig. 4.24.

In addition to the standard ion loss mechanisms implemented in ISDEP, Charge Exchange (CX) losses have been introduced for these simulations. We assume that CX processes are represented locally by a Poisson distribution with typical time τ_{CX} and kill the ions according to this distribution. The average lifetime τ_{CX} of an ion moving with speed v in a plasma with neutral density n_n is:

$$\tau_{CX} = \frac{1}{n_n \, \sigma_{CX} \, v},\tag{4.10}$$

The charge exchange cross section σ_{CX} is a function of the ion energy (see [28] and Fig. 4.24). The τ_{CX} profile can be seen in Fig. 4.25 as a function of the fast ion energy and the effective radius. We will see in Sect. 4.3.2 that the typical lifetime of a fast ion is of the order of a milisecond. This implies that CX processes are not negligible only for low energies and in the external part of the plasma. During their lifetimes

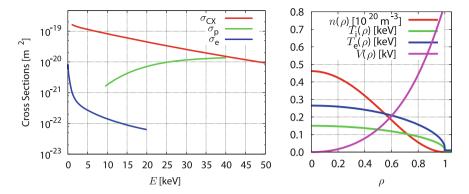


Fig. 4.24 Left plot Cross sections for the relevant atomic processes in the fast ion detection: charge exchange (σ_{CX}) , ionization by protons (σ_p) and ionization by electrons (σ_e) as functions of the NBI ion energy. Note that σ_e is included in the calculation even though it is much smaller than σ_p . Source www-amdis.iaea.org/ALADDIN. Right plot plasma profiles used in ISDEP for the comparison with the CNPA, similar to the experimental profiles

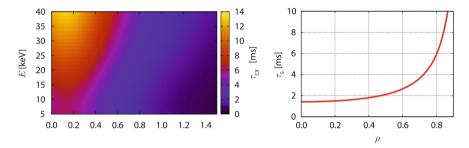


Fig. 4.25 Left plot charge exchange time in TJ-II, according to Eq. (4.10), in the conditions considered in this discharge. It turns out that CX processes are not negligible only in the external part of the plasma and for low energies, where $\tau_{\rm CX}$ is short enough. Since ISDEP deals with orbits in the Scrape-Off-Layer (SOL) too, where $\rho > 1$, $\tau_{\rm CX}$ is also calculated in the SOL, assuming that the profiles of plasma parameters are constant and equal to the value that take at $\rho = 1$. Right plot Spitzer slowing down time [16], showing that the typical timescale of this system is a few milliseconds, much smaller than the typical CX time in the plasma bulk

the fast ions explore the whole magnetic surface and thus the surface averaging of $n_n(\rho)$ is valid.

4.3.2 Reconstruction of the CNPA Flux Spectra

We perform a set of simulations with ISDEP aiming to calculate the fast ion flux spectrum and compare it with the flux measured by the CNPA diagnostic in TJ-II. We must estimate numerically the steady state distribution function in the conditions

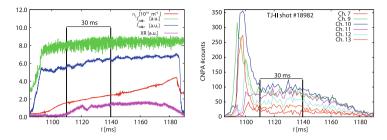


Fig. 4.26 Left plot line density, X-rays and NBI traces for shot #18982. Right plot CNPA raw data for selected channels (see Fig. 4.22 for the energy associated to each channel and its width). For this shot, a 30 ms plateau is found in the signals. We can obtain a low error flux spectrum averaging each channel in time and taking the mean with similar shots

of the experiment and then calculate the neutral flux that reaches the CNPA using Eq. (4.7).

Usually the signal of each CNPA channel is very noisy, so we have to apply statistical techniques to diminish the dispersion of the measurements. We choose a set of five reproducible discharges with a plateau in the CNPA signals that lasts several tens of milliseconds. These plasmas correspond to shots #18982-86 and were performed in the standard magnetic configuration (100_44_64). The experimental traces of the discharge #18982 are shown in Fig. 4.26 (left), where line density, X-rays and NBI traces are plotted. The CNPA signals for shot #18982 can be seen in Fig. 4.26 (right). In this shot, the plateau in the signals lasts for 30 ms. A time average is performed for each channel in the plateau time interval, and the final spectrum is the mean of the five shots chosen. This flux spectrum is representative as long as the plasma is stationary.

The plasma density and temperature profiles are needed to run ISDEP, FAFNER2 and EIRENE, while the electric potential is required by ISDEP. The density and electron temperature profiles are the average of the Thomson Scattering signals for these discharges. Ion temperature is taken to have the same shape as T_e , but scaled to have a maximum value of 150 eV, as is suggested in [29]. The plasma potential is obtained from the Heavy Ion Beam Probe (HIBP) for a typical NBI discharge [30]. Figure 4.24 shows these profiles and the neutral density.

The numerical simulations have been carried out with the same procedure as in Sect. 4.1.2. The combination of temperature and density profiles leads to a high collisionality regime (high n and low T_e), so the energy slowing down time (or thermalization time) is small and the steady state is reached in few milliseconds.

Figures 4.27 and 4.28 show the ISDEP results for the fast ion steady state distribution function and its statistical error in %. It is seen that only the values of f smaller than 10^{-13} in Fig. 4.27 are affected by a 10 % error. With these plasma profiles, thermalization occurs much faster than in the case previously studied in Sect. 4.1.2 because of the higher collisionality of the present discharges. The population of particles in the high energy region of the phase space is much smaller here and the thermalization timescale is also smaller. In this high collisionality range the

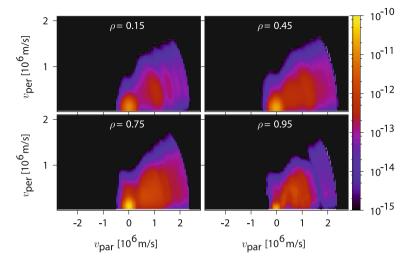


Fig. 4.27 Steady state distribution function for TJ-II with the profiles shown in Fig. 4.24 for $\rho=0.15$ (top, left); $\rho=0.45$ (top, right); $\rho=0.75$ (bottom, left) and $\rho=0.95$ (bottom, right). Traces of the injected ions at 10, 15 and 30 keV can be seen. The results are presented normalized in the sense $\int d\rho \ dv_{||} \ dv_{\perp} \ f(\rho, v_{||}, v_{\perp}) \ J(\rho, v_{||}, v_{\perp}) = 1$. The statistical error in f depends on the value of f, see Fig. 4.28

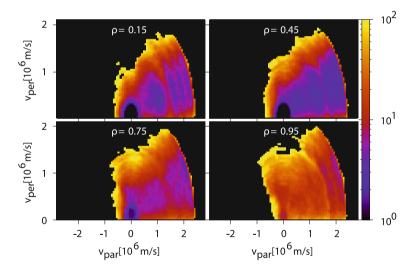


Fig. 4.28 Relative statistical errors in f (see Fig. 4.27), in %

simulated slowing down time is $\tau_S \sim 3$ ms versus $\tau_S \sim 20$ ms in Ref. [31]. This fact ensures the validity of the time average in the CNPA signals because τ_S is one order of magnitude smaller than the time integration interval.

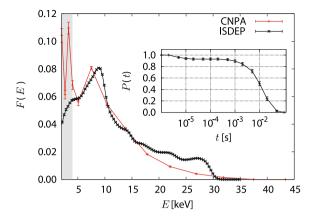


Fig. 4.29 Comparison of the flux spectrum measured by the CNPA and the one calculated with ISDEP. Both flux spectra are normalized to one. In the CNPA spectrum the error bars are the standard deviation of the measurements while in the ISDEP curve they are the statistical errors. The error bars are smaller than the symbol size for many points in the spectrum. The persistence of fast ions P(t) is shown in the small chart indicating the existence of two timescales: NBI direct losses around $t = 10^{-5}$ s and CX or hits to the vacuum vessel at larger times. Notice that the errorbars in the experimental data are the statistical dispersion in the set of reproducible discharges and no noise or instrumental error are considered. The gray shaded area indicates the region in the spectra that is affected by thermal ions from the plasma, so it must not be trusted

Once the calculations are done and $f(\rho,v_{||},v_{\perp})$ is found, we must simulate the particle flux that reaches the CNPA array. Then we apply the jack-knife technique to solve the integral in Eq. (4.7), using the data for the LOS (Fig. 4.23) and the cross sections (Fig. 4.24). From the whole $f(\rho,v_{||},v_{\perp})$ calculated with ISDEP, only the parts that satisfy $\rho=\rho_{\rm LOS}$ and $v_{||}/v=\cos\xi$ are used for the integral. The neutral fluxes, measured and simulated, are plotted in Fig. 4.29 as functions of the energy. Figure 4.29 also shows the persistence of test particles (defined as the fraction of surviving particles) as a function of time.

Figure 4.29 presents a general good agreement between theory and experiment. Note that the energy resolution in CNPA is not enough to distinguish the peaks at 10, 15, 30 keV of the injection energy. It is also seen in this plot that in the high energy range ISDEP overestimates the real flux of neutrals. This could be attributed to a particular kind of losses that are not taken into account in ISDEP: Alfvén resonances [32].

Alfvén waves are MHD perturbations that propagate along the magnetic field with a wide range of poloidal and toroidal modes, called the *Alfvén zoo*. They may interact with plasma particles when a resonance condition is satisfied, usually increasing the perpendicular energy and moving then to a bad confinement region in phase space.

In TJ-II, Alfvén resonances are important only for suprathermal ions, perturbing their orbits and worsening their confinement. Ions may destabilize an Alfvén mode when its velocity is similar to the Alfvén velocity. In terms of the energy:

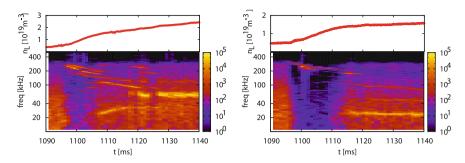


Fig. 4.30 Line density and Mirnov coil power spectra as a function of time for shots #18982 (*left*) and #18997 (*right*). The Alfvénic activity can be identified for frequencies $f \sim 100$ –200 kHz showing that $f_{\rm Alfvén} \sim 1/\sqrt{n}$

$$E_A = \frac{mv_A^2}{2}, \qquad v_A = \frac{B}{\sqrt{n\,m\,\mu_0}}.$$
 (4.11)

In the case of interest, the Alfvén energy has a minimum of $E_A \approx 50\,\mathrm{keV}$ for the highest density and $B=1\,\mathrm{T}$, well above the NBI injection energy, so resonances with the first harmonic are, in principle, impossible. In spite of this fact, it has been experimentally shown in [33] that in TJ-II Alfvén destabilization may occur for velocities $v \gtrsim v_A/3$, corresponding to different toroidal and poloidal modes. Figure 4.30 (left) shows the line density and the Mirnov coil #5 power spectra as a function of time. Clear traces of Alfvén activity can be seen for frequencies $f \sim 100-200\,\mathrm{kHz}$ due to the scaling of the Alfvén frequency with the density: $f_{\rm Alfven} \sim 1/\sqrt{n}$.

This overestimation of the distribution function in the high energy region might also be due to the presence of impurities in TJ-II [34]. We have made extra simulations in order to assess the impact, by means of larger pitch-angle-scattering frequency and stronger isotropization, of Z_{eff} . Our calculations show no strong dependence on Z_{eff} for the values estimated at TJ-II, around 1.3 for these discharges [35], within the error bars (see Fig. 4.31). Thus, since the effects of the impurities may be neglected, the discrepancy in the high energy tail of Fig. 4.29 could be attributed to Alfvén losses.

The peak near 7–9 keV and the hollow in 5 keV are well reproduced by ISDEP and are due to the geometrical properties of the detector because they do not appear if the integration is not done along the LOS. At low energies (shaded area in Fig. 4.29) the discrepancies are very important, but this is not surprising since the CNPA signal contains information of bulk ions, not only of those that were injected with the NBI system. The statistical distribution of 150 eV ions contains a few number of suprathermal ions [36] of energies of some keV that cannot be distinguised from the NBI fast ions by the CNPA. These bulk ions are not considered in the ISDEP simulations. Usually each CNPA channel recieves $\sim 10^2$ counts per milisecond, so a very small aditional flux can perturb the measurements.

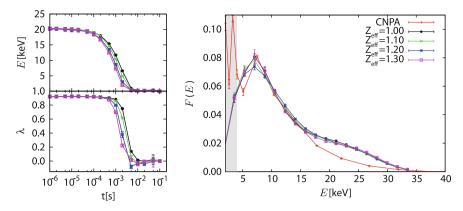


Fig. 4.31 Left plot Average fast particle energy and pitch as functions of time for $Z_{eff} = (1.0, 1.1, 1.2, 1.3)$. Right plot CNPA flux spectra calculated with ISDEP for several values of Z_{eff} . The higher Z_{eff} the lower the slowing down and deflection times, but the flux spectrum is not altered notably. We reduced the energy resolution in the ISDEP simulations in order to save computing time for this test

In order to show that the structure of $f(\rho,v_{||},v_{\perp})$ calculated by ISDEP as well as the LOS description are crucial to reproduce the experimental flux spectrum, we solve again Eq. (4.7) modifying $f(\rho,v_{||},v_{\perp})$ and the line of sight. First we calculate the flux changing the value of $\cos\xi$ along the CNPA LOS, i.e., we fix v_{\perp} to a certain value and reconstruct the flux spectrum. Also we calculate F(E) keeping f constant in ρ and making it Gaussian in velocity space, with the same $\langle v \rangle$ and $\langle v^2 \rangle$ as the original distribution function. Figures 4.32 and 4.33 show that none of these curves fits the experimental data, hence the final result is very sensitive to $f(\rho,v_{||},v_{\perp})$ as well as to the geometry of the LOS.

In order to explore the properties of the fast ions in a different set of plasma parameters we perform another simulation of the CNPA signal for low density NBI shots (#18997–98) in the configuration 101_42_64 . This configuration is very close to the standar configuration (100_44_64) and the main differences can be seen in Table 4.2. The profiles used are plotted in Fig. 4.34 (left). Figure 4.34 (right) shows the comparison between the CNPA data and the numerical simulations for these shots. Since the neutral density increases when the plasma density decreases, CX effects are stronger and the average lifetime of the fast ions is smaller. The difference in the neutral flux F(E) is important in the high energy region, pointing again to the possible influence of Alfvén modes on the fast ion confinement (see Fig. 4.30 right for the spectrogram). A discrepancy between the measurement and the simulation can be seen at $E = 10 \, \text{keV}$, but it is not clear how important it is due to the limited energy resolution of the CNPA.

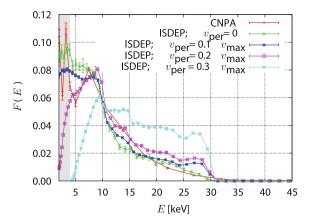


Fig. 4.32 Neutral flux spectra calculated modifying artificially the geometry of the system and the fast ion distribution function. The red curve is the experimental flux, same as in Fig. 4.29, while in the other curves a fixed v_{\perp} is considered. In the chart, $v_{max} = 3 \cdot 10^6 \text{m/s}$

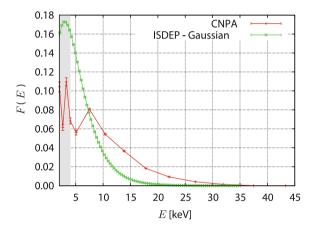


Fig. 4.33 Experimental and recalculated flux spectrum, assuming that f is constant in ρ and Gaussian in velocity space. It is clear then that the detailed calculation of f with ISDEP is essential to reproduce the experimental results (see Fig. 4.29)

Table 4.2 Plasma volume, average minor radius and iota range for the two magnetic configurations considered

Configuration	$V[m^3]$	a[cm]	Iota range
100_44_64	1.098	19.254	1.551-1.650
101_42_64	1.079	19.085	1.534-1.630

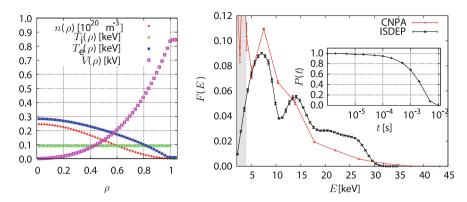


Fig. 4.34 Plasma profiles for a low density NBI shot (*left*). CNPA spectra and ISDEP simulation (*right*)

4.3.3 Neutral Flux and Slowing Down Time

In this Section we show the comparison of two experimental decay times with the ISDEP predictions: the neutral flux decay time in NBI-Blip experiments in LHD and the energy slowing down time in TJ-II.

For LHD we base our comparison on the experimental results presented in [22], which shows the decay time of the FNA count number during an NBI-blip experiment. An NBI-blip experiment consists of short NBI pulses applied to a base plasma. These disgnostics were sensitive to energies between 29 and 36 keV and the decay time is evaluated at several radial positions for $\rho > 0.55$. The count decay time is what we have calculated using ISDEP and shown in Fig. 4.18 (left), because it includes thermalization, particle transport and loss effects. The distribution function for the NBI-Blip scenario is calculated following the procedure shown in Sect. 2.2.6. In this simulation the NBI-Blip time is $T_B = 10$ ms and ions are considered lost when they reach the lower energy limit (29 keV). The agreement between simulations and experiments (see Fig. 4.35) is good, but only a limited range in ρ is provided by the FNA detector in LHD plasmas.

In TJ-II we choose shot #15470 because it presents almost static plasma profiles and is suitable to be simulated with ISDEP. In this discharge the NBI heating ends before the end of the discharge and the plasma is maintained with the electron cyclotron resonance heating. The plasma profiles of this discharge are shown in Fig. 4.36. When the neutral beam injection stops we measure the time that takes each channel to go down to zero. The delay time between channels would be the time needed for the ions to slow from the high to the low energy. We neglect the channels with energies bellow half NBI maximum energy because the neutral beam source would mask the data. With the delay times between some energy channels we calculate the Spitzer time t_S Eq. (4.4). With this Spitzer time now we can calculate the experimental slowing down time. Figure 4.36 shows the profile of slowing down time

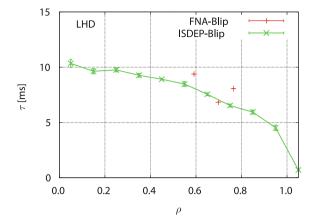


Fig. 4.35 Comparison of the neutral flux decay time (Sect. 4.2.3) and NBI-Blip experiments in LHD

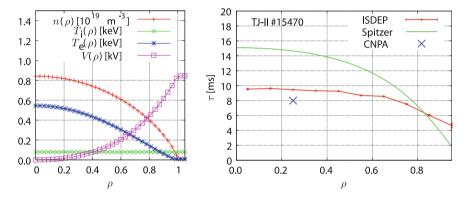


Fig. 4.36 *Left plot*: profiles of density, ion and electron temperatures and plasma potential for shot #15470 in TJ-II. The density and temperatures are obtained from the Thomson Scattering system and the potential from the Heavy Ion Beam Probe. The magnetic configuration is the TJ-II standard configuration, same as in Sect. 4.9. *Right plot*: slowing down time for discharge #15470 in TJ-II calculated with ISDEP (red) and with the Spitzer formula (green). The experimental measurement gives $\tau_{\text{CNPA}} \sim 8 \, \text{ms}$ for $\rho \sim 0.3$ ($blue \ cross$ in the picture), in good agreement with ISDEP simulations

estimated with ISDEP for shot #15470 and with the Spitzer formula Eq. (4.4). CNPA can measure the slowing down time integrated in its whole line of sight, roughly in $\rho \sim 0.25$, giving $\tau_{\text{CNPA}} \sim 8$ ms. This time simulated with ISDEP is $\tau = 9.45$ (2) ms for $\rho \in (0.2, 0.3)$ (see Fig. 4.36). The two times are in good agreement, but still $\tau_{\text{CNPA}} < \tau$. This can be attributed to the fact that τ_{CNPA} has contributions all along the line of sight of the CNPA array, which covers a wide range in ρ . As τ decreases with ρ , the contributions to the CNPA signal from $\rho > 0.5$ tend to diminish the final

value of τ_{CNPA} . In addition, since the error in the experimental values is very difficult to obtain, the 1.5 ms difference could be due to the experimental error.

Dedicated experiments to measure the slowing down time in TJ-II with higher precision will be performed as a continuation of this work.

4.4 Conclusions

The confinement properties of the NBI fast ions are studied for stellarators using the global Monte Carlo guiding center orbit code ISDEP. The main result of this chapter is the calculation of the fast ion distribution function $f(\rho,v_{||},v_{\perp})$, both time dependent and in the steady state, for two different NBI lines and plasmas: perpendicular injection for LHD and tangential for TJ-II. All the relevant quantities can be estimated as moments of such distribution. The steady state profiles of toroidal and poloidal rotation and radial velocity are calculated in this way. Since momentum conservation is not satisfied in ISDEP, these rotation profiles of the beam ions are not a measure of the whole plasma rotation, only to the maximum capability of NBI rotation driving. The interest of the calculation of poloidal rotation relies particularly on its capability for creating shear flows, which could help to reduce the turbulence and to create transport barriers.

The slowing down time is also computed and compared with Spitzer's formula, showing the effect of ion transport in a particular magnetic configuration and injection properties on such quantity. This effect is specially important in low density plasmas in TJ-II. The loss cones in the two devices are also estimated with ISDEP as functions of time, showing the different time scales of the loss processes. The slowing down time appears to be of the same order of the fast ion confinement time in the two studied cases.

Comparison with experimental data [21, 23] measured with NPAs (Neutral Particle Analyzers) has been be done for both devices. In TJ-II we have successfully reconstructed the CNPA spectra for two discharges with very different plasma density. We have concluded that the discrepancies between simulation and experiment at high energies are probably due to the Alfvén activity in TJ-II. An estimation of the fast ion slowing down time has also been done in this machine in a time dependent scenario.

The decay time (in the $E > 29 \,\mathrm{keV}$ energy range) during NBI-Blip experiments in LHD have also been well reproduced by the code. Unfortunately, experimental data are available only in a limited region of the plasma.

On the whole, we may conclude that ISDEP is a useful simulation tool to study fast ion dynamics in 3D magnetic fusion devices.

¹ After the realization of this report, further investigations clarified this issue. They were published in A. Bustos *et al.*, Physics of Plasmas **20** (2) p. 022507.

References 95

References

- 1. Ochando M, Castejon F, Navarro A (1997) Nucl Fusion 37:225
- 2. Komori A et al (2010) Fusion Sci Technol 58(1):11
- 3. Hirshman S, Whitson J (1983) Phys Fluids 26:3553
- 4. Alejaldre C et al (1990) Fusion Technol 17:131
- 5. Sánchez J et al (2011) Nucl Fusion 51:094022
- 6. Sánchez J et al (2009) Nucl Fusion 49:104018
- 7. Wagner F (2007) Plasma Phys Controlled Fusion 49:B1
- 8. Murakami S, Nakajima N, Okamoto M (1995) Trans. Fusion Technol 27:256
- 9. Teubel J (1994) Monte Carlo simulations of NBI into the TJ-II helical axis stellarator (Max Planck Institute fur Plasmaphisik), 4/268, Germany
- 10. Terry PW (2000) Rev Mod Phys 72:109
- 11. Rice J et al (2007) Nucl Fusion 47:1618
- 12. Helander P, Simakov AN (2008) Phys Rev Lett 101:145003
- 13. Yoshinuma M et al (2009) Nucl Fusion 49:075036
- 14. Biglari H, Diamond PH, Terry PW (1990) Phys Fluids B 2:1
- 15. Groebner RJ, Burrell KH, Seraydarian RP (1990) Phys Rev Lett 64:3015
- 16. Stix TH (1972) Plasma Phys 14:367
- Wesson J (2004) Tokamaks (The international series of monographs on physics). Oxford University Press, Oxford
- 18. Huba J (2009) NRL plasma formulary. Taylor and Francis, USA
- 19. Velasco J, Castejón F, Tarancón A (2009) Phys Plasmas 16:052303
- 20. Castejón F et al (2007) Plasma Phys Controlled Fusion 49:753
- 21. Osakabe M et al (2008) Rev Sci Instrum 79:10E519
- 22. Osakabe M et al (2010) Plasma Fusion Res 5:S2029
- 23. Balbin R et al (2005) EPS 2005 meeting, Tarragona, D5.001
- Hutchinson IH (2002) Principles of plasma diagnostics. Cambridge University Press, Cambridge
- 25. www.eirene.de/html/relevant_reports.html
- 26. Castejón F et al (2002) Nucl Fusion 42:271
- 27. de la Cal E et al (2008) Nucl Fusion 48:095005
- 28. http://www-amdis.iaea.org/ALADDIN
- 29. Fontdecaba J et al (2010) Plasma Fusion Res 5:2085
- 30. Melnikov A et al (2006) Fusion Sci Technol 51(1):31
- 31. Bustos A et al (2011) Nucl Fusion 51:083040
- 32. Heidbrink W (2008) Phys Plasmas 15:055501
- 33. Jiménez-Gómez R et al (2011) Nucl Fusion 51:033001
- McCarthy K, Tribaldos V, Arévalo J, Liniers M (2010) J Phys B Atomic Mol Opt Phys 43:144020
- 35. Baiao D et al (2011) Submitted to PPCF
- 36. Jimenez-Rey D et al (2008) Rev Sci Instrum 79:093511

Chapter 5 Simulations of NBI Ion Transport in ITER

In this Chapter we will deal with NBI ion transport properties in the ITER geometry introduced in Chap. 3. If the injectors are installed in ITER as planned, ITER should have a total of 50 MW of NBI input power [1], that will contribute to reach steady state fusion reactions. The importance of the NBI transport calculations to foresee the influence of the heating system in the plasma is then clear. We will compute the distribution function in the steady state and the rotation and thermalization time profiles, as we did for stellarators in Chap. 4.

We start discussing the fast ion initial distribution, followed by the numerical results and the conclusions.

5.1 Fast Ion Initial Distribution

The initial distribution of the fast ions is calculated in the same way as we did in Chap. 4 for the TJ-II stellarator. We use the FAFNER2 code, adapted to the ITER magnetic field and plasma profiles, given by the equilibrium calculations, described in Figs. 3.3 and 3.4. The inclusion of new equilibriums in FAFNER2 is out of the scope of this thesis. In fact, we benefit from the work carried out by M. Tereschenko at BIFI in the spring of 2011.

The energy spectrum of the neutral beam is different from those considered previously because it has only one component at $E_0 = 1$ MeV instead of three components at E_0 , $E_0/2$ and $E_0/3$. Actually ITER injectors are based on negative ions, instead of the positive ion technology like in TJ-II.

We plot the FAFNER2 output in Figs. 5.1 and 5.2. Figure 5.1 is a scatter plot in (ρ, λ) space, showing the ionization points. From this picture it is possible to deduce the path followed by the neutrals. Since the neutral beam crosses the magnetic axis, the pitch angle distribution is rather complex. In Fig. 5.2 we plot $f(t = 0, \rho, \lambda)$ to clarify this point, observing a broader distribution in pitch than the distributions in the stellarators previously shown (compare with Figs. 4.12 and 4.13). It is also seen

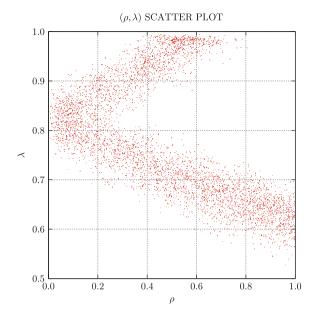


Fig. 5.1 Scatter plot of the fast ion initial distribution in (ρ, λ) space. The neutral beam enters the plasma in $\rho = 1$, crosses the magnetic axis and is completely ionized before leaving the plasma

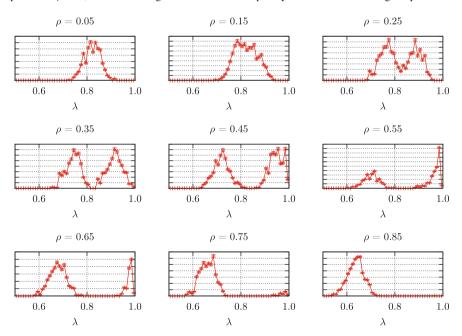


Fig. 5.2 Probability distribution functions of the pitch for several radial positions. The plots with two maxima point out that the beam crosses some magnetic surfaces twice, with different inclination with respect to the field lines

that two maxima of the pitch appear on given magnetic surfaces, showing that the beam crosses twice such surface, with different angles with respect to the magnetic field.

5.2 NBI Ion Dynamics in ITER

Once the input data are determined, we run ISDEP and calculate the steady state of the distribution function, the rotation profiles and the average energy profile using the same mathematical methods as in Chap. 4. Since we are interested in the high energy ion transport, we will consider that any fast ion that reaches 20 keV (approximately the plasma temperature) is killed in our simulation. This allows us to save CPU time because thermal particles are usually better confined than fast ions. Globally, the numerical results presented in this Chapter requires around 15,000 CPU hours, provided by the EULER cluster at CIEMAT.

Figures 5.3 and 5.4 show global averages and radial profiles of the fast ion population. We can see the typical timescales of the system, around 0.1–1 s in confinement time and a bit shorter in thermalization time. The confinement time, obtained from

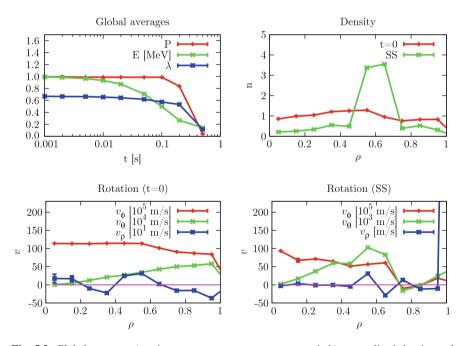


Fig. 5.3 Global averages (persistence, average energy, average pitch), normalized density and rotation profiles for the fast ions in ITER. We can see that the typical timescale of transport and thermalization of the NBI ions is 0.1–1s and that they tend to accumulate in $\rho \in (0.55, 0.75)$, according to $v_{\rho}(\rho)$. The steady state profiles are denoted by SS

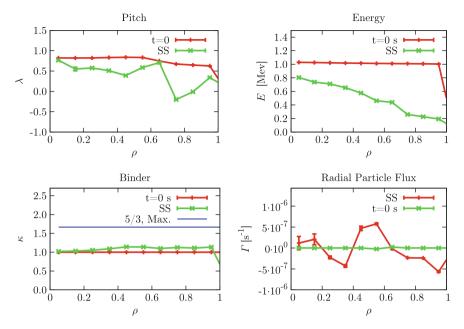


Fig. 5.4 Pitch, energy, Binder cumulant and particle flux profiles, both in the initial time and in the steady state

the persistence is 144.1(2) ms and the global slowing down time, taken form the evolution of the average energy is 90.0(1.1) ms, smaller than the confinement time. The slowing down time is calculated from the curve E(t) in Fig. 5.3 in the energy range indicated in the picture: $E \in (1 \text{ MeV}, \sim 140 \text{ keV})$. This means that, in average, the ions deposit most of their energy in the plasma bulk before escaping.

The right top panel of Fig. 5.3 shows the normalized density profile. It can be seen that the density profile at the initial time is almost flat, but in the steady state particles tend to accumulate in $\rho \in (0.5, 0.7)$. The NBI velocity components in toroidal coordinates, $(v_{\rho}, v_{\varphi}, v_{\theta})$, are also depicted in the bottom panels of Fig. 5.3, both at t=0 and in the steady state. Except for v_{φ} and v_{θ} at t=0, the velocity profiles present strong gradients, in particular $v_{\rho}(\rho)$ in the steady state, which changes sign four times. This makes possible the accumulation of ions in $\rho \in (0.5, 0.7)$ because $v_{\rho}(\rho=0.55)>0$ and $v_{\rho}(\rho=0.65)<0$, creating a kind of trapped region. Of course, the random effect of collisions eventually expels the ions, but it is clear that fast ions spend most of their lifetime in that part of the plasma.

It should be noted that the steady state profiles of v_{φ} and v_{θ} are similar to the initial profiles for $\rho < 0.6$, showing that characteristics of the rotation of the beam are qualitatively conserved. This means that the NBI will be efficient to drive a uniform toroidal rotation for $\rho < 0.6$.

In Fig. 5.4 we can see the radial profiles of the pitch, energy, Binder cumulant and radial particle flux at the initial time and in the steady state. Although the initial

pitch profile is close to $\lambda=1$, in the steady state we can observe an inversion of the NBI-induced current because $\lambda(\rho=0.65)<0$. This is a very interesting result and we will discuss it deeply in the following sections.

The initial energy profile is flat because the ionization process is elastic. In the steady state the energy decreases with ρ , following roughly the collisionality profile $(\sim nT^{-3/2})$.

The binder cumulant can be seen in the bottom right panel of Fig. 5.4. It takes values of $\kappa \approx 1$ in the steady state, much lower than the Binder cumulant for the Maxwellian distribution $\kappa = 5/3$. Thus, according to this ITER model, the test particle distribution remains far from the Maxwellian. This feature can be also seen in the steady state distribution function $f(\rho, v_{||}, v_{\perp})$.

The fast ion radial flux is also shown in the bottom right panel of Fig. 5.4. The flux changes sign several times, showing zones of very good fast ion confinement that alternate with worse confinement regions.

Figures 5.5 and 5.6 show the distribution function in the steady state with its statistical error in % at eight radial positions:

$$\rho = (0.15, 0.25, 0.35, 0.45, 0.55, 0.65, 0.75, 0.85).$$
 (5.1)

The accumulation of particles in $\rho \in (0.5, 0.7)$ can be seen in Fig. 5.6 (note that f has different scales). This function presents clear deviations from the Maxwellian because it does not decrease monotonically when the energy increases. These figures reveal two interesting features of f: the inversion of the NBI current and oscillations in the energy distribution, that will be studied at the end of this section.

We calculate the slowing down time in the same way as we did for stellarators in Sect. 4.2.3. Figure 5.7 displays the Spitzer time profile [2] and the slowing down time determined with ISDEP. In this system the radial transport homogenizes the thermalization profile like in TJ-II (recall Fig. 4.18). This strong difference observed between the two time profiles is an indication that the slowing down time must be estimated carefully in ITER when the plasma is in the banana regime. Radial transport and particle losses must be considered in this calculation.

Finally we have estimated the fraction of prompt losses in this NBI system. It turns out that only ~ 1.3 % of the total incoming flux of fast ions is lost with energy larger than 20 keV. All other ions are lost artificially when they reach E=20 keV. As expected, the NBI heating system in ITER will be very efficient.

Nevertheless, even with a high efficiency the prompt losses may cause damage because the lost particles have energies around 1 MeV. Figure 5.8 is a scatter plot of the spatial distribution of the direct losses in the LCFS. We observe a clear tendency to accumulate in the upper part of the device, being the top of the plasma the main escaping region. The average kinetic energy of these prompt losses is $\langle E \rangle = 0.859(3)$ MeV. A rough estimation considering an input power of P = 50 MW and a loss area of $S \sim 50$ m² gives a heat flux of $P/S \sim 10-15$ kW/m². This is lower than the typical power flux of 1 MW, which is the target of the ITER walls. Consequently, the inner wall of ITER must be able to resist this heat load.

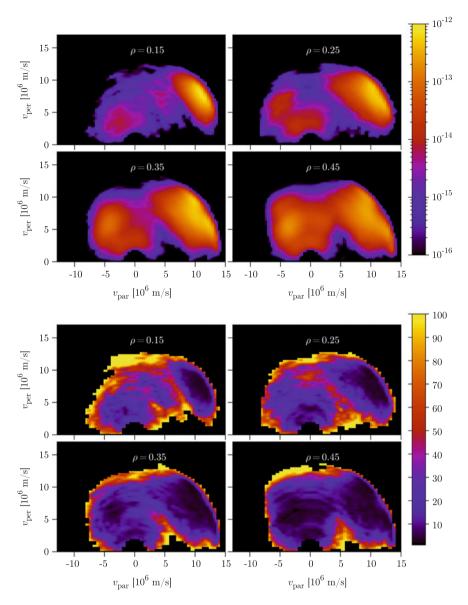


Fig. 5.5 Steady state distribution function $f(\rho, v_{||}, v_{\perp})$ and relative error for the NBI ions in ITER in the inner part of the plasma. The appearance of two spots in some charts is due to the initial condition (see Fig. 5.2)

In spite of what preceded, these fast ions losses can cause sputtering and impurity release and should be taken into account.

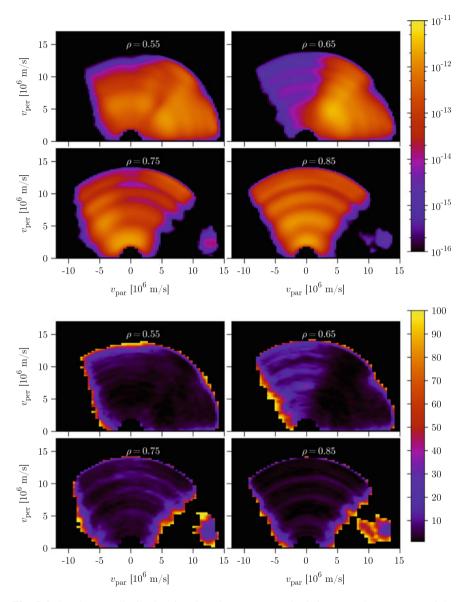


Fig. 5.6 Steady state distribution function $f(\rho, v_{||}, v_{\perp})$ and relative error the outer part of the plasma. Specifically, $f(\rho = 0.75, v_{||}, v_{\perp})$ presents two interesting features studied in this report: the inversion of the NBI current and the appearance of several maxima and minima in the energy distribution

Note that this result is an approximated estimation because neither the SOL or the divertor have been considered.

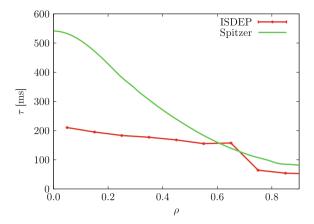


Fig. 5.7 Slowing down or thermalization time, calculated with ISDEP and with the Spitzer formula. Both *curves* agree in order of magnitude, but the Spitzer time is larger than our calculation in most of the plasma. In our case transport across magnetic surfaces tends to homogenize the profile

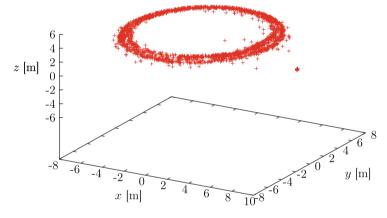


Fig. 5.8 Scatter plot of the direct losses for the NBI ions in ITER. he losses accumulate in the upper part of the device in an area of $\sim 50\,\mathrm{m}^2$. he magnetic axis is a horizontal circle in a plane $z\approx 0.4\,\mathrm{m}$. It must be pointed that an inclusion of a divertor in the ITER model may change this distribution drastically

5.2.1 Inversion of the Current

As it can be seen in Fig. 5.4 and in the distribution function (Figs. 5.5 and 5.6), the λ profile changes sign with ρ . This is a surprising result because the fast neutrals are injected in a well defined direction with a net toroidal moment. Figure 5.6 also shows an accumulation of particles in the region $v_{||} < 0$ for $\rho = 0.75$. We demonstrate that this is due to the deterministic evolution of the pitch. Let us perform a rough analysis of the pitch evolution. The SDE for λ , taken from Sect. 1.3.3 is:

$$d\lambda = \left(\frac{1 - \lambda^{2}}{2} \left(\frac{2ev_{||}}{mv^{3}} \mathbf{E} \cdot \mathbf{v}_{||} - \frac{\lambda}{B^{3}} \mathbf{E} \cdot (\mathbf{B} \times \nabla B)\right) + \frac{2}{B^{3}} \mathbf{E} \cdot \left(\frac{\mathbf{B} \times \mathbf{R}_{c}}{R_{c}^{2}}\right)\right) - \frac{v_{||}}{vB} \nabla B \cdot \mathbf{v}_{||} - \frac{m\lambda v^{2}}{eB^{3}} \nabla B \cdot \left(\frac{\mathbf{B} \times \mathbf{R}_{c}}{R_{c}^{2}}\right)\right) dt - \sum_{b} \lambda v_{d}(b) dt + \sqrt{\sum_{b} (1 - \lambda^{2}) v_{d}(b)} dW^{\lambda},$$
 (5.2)

We study in detail the behavior of the dominant terms in $\dot{\lambda}(\lambda)$. Therefore we just take the terms proportional to the particle velocity, assumed to be dominant. This just leaves the 4th and 5th term in 5.1. From the $\dot{\lambda}(\lambda)$ plots (Fig. 5.9) we can identify the stable and unstable points. The results is that for $\rho>0.6$ there is an accumulation point in $\lambda=-1$, because $\dot{\lambda}<0$ for $\lambda<-0.5$. It means that the fast ion current inverts in the outer regions of ITER. This also explains the appearance of an important population of particles with $v_{||}<0$ in $\rho\sim0.4$ in Fig. 5.5.

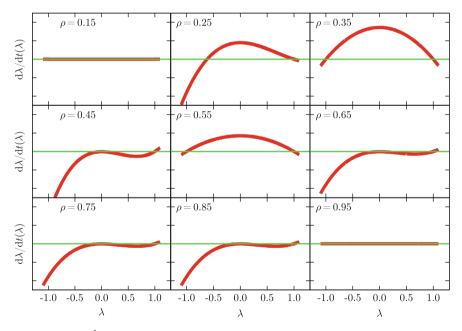


Fig. 5.9 We plot $\dot{\lambda}(\lambda, \rho)$ for several radial position, finding that for $\rho > 0.6$ the fast particles tend to move to the region of $\lambda < 0$. The derivative $\dot{\lambda}(\lambda, \rho)$ is calculated using the routines implemented in ISDEP and averaging over the magnetic surfaces. The *green line* indicates the $\dot{\lambda} = 0$ line

5.2.2 Oscillations in E

The distribution function of Figs. 5.5 and 5.6 present an oscillating behavior in E for several effective radius. Now we calculate $f(\rho, E)$ transforming $f(\rho, v_{||}, v_{\perp})$ into $f(\rho, E, \lambda)$ and integrating in λ . The coordinate transformation is:

$$v_{||} = \sqrt{E}\lambda,$$

$$v_{\perp} = \sqrt{E}\sqrt{1 - \lambda^2}.$$
(5.3)

Thus, the matrix of partial derivatives is:

$$\begin{pmatrix}
\frac{\partial v_{||}}{\partial E} & \frac{\partial v_{||}}{\partial \lambda} \\
\frac{\partial v_{\perp}}{\partial E} & \frac{\partial v_{\perp}}{\partial \lambda}
\end{pmatrix} = \begin{pmatrix}
\frac{\lambda}{2\sqrt{E}} & \sqrt{E} \\
\frac{1}{2\sqrt{E}\sqrt{1-\lambda^2}} & -\frac{\sqrt{E}\lambda}{\sqrt{1-\lambda^2}}
\end{pmatrix}, (5.4)$$

and the Jacobian:

$$J = \frac{\lambda^2 + 1}{2\sqrt{1 - \lambda^2}}.\tag{5.5}$$

We perform the integration obtaining $f(\rho, E)$. Figure 5.10 shows these results. The oscillations in the energy can be seen for $\rho \geq 0.75$. These are very surprising and unwelcome results. They are not good for the confinement because they may give rise to kinetic instabilities [3]. A resonant wave can grow out of control when the energy distribution function has positive slope, so it is not desirable. In order to check that these oscillations are not a purely numerical effect, we perform the following tests with ISDEP:

- First of all, we have suppressed the collision operator, finding that the oscillations disappear. This demonstrates that those oscillations are a collisional effect.
- If we remove the electric field in the dynamics the oscillations hardly change. So, the electric field **E** has not a strong influence on them.
- If we do not evolve the particles in position space but in velocity space ($\dot{\mathbf{r}} = \vec{0}$ and \dot{E} , $\dot{\lambda} \neq 0$) the oscillation appear, but in different positions and with much smaller amplitude, almost negligible. Thus, transport is a crucial factor.
- Using different numerical methods and times step do not change the results. We have used an order 2+2 method and a Runge-Kutta 4+1 with Δt from $2 \cdot 10^{-8}$ to $2 \cdot 10^{-9}$ finding no difference.
- Idem with the magnetic grid discretization. We usually take $N_R \times N_Z = 400 \times 600$ points in the 2D equilibrium. Changing to $N_R \times N_Z = 600 \times 1000$ does not change the results.

Thus, we conclude that the maxima and minima of $f(E, \rho)$ are due to the combined effect of particle drifts and collisions with the background.

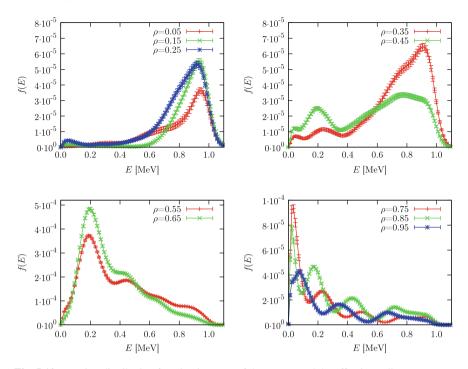


Fig. 5.10 Fast ion distribution function in terms of the energy and the effective radius

5.3 Heating Efficiency

One of the advantages of the combination of FAFNER2 and ISDEP is that we can change the input parameters at will. In this last section we perform a scan in the injected neutral energy and study the energy and power deposition profiles. The neutral energy values chosen are:

$$E_0 = (0.8, 0.9, 1.0, 1.1, 1.2) \,\text{MeV}.$$
 (5.6)

As usual, we use FAFNER2 to estimate the initial fast ion distribution in ITER at those energies. The first interesting parameter in this power scan is shine trough losses, defined as the fraction of incoming neutrals that are not ionized in the plasma and are consequently lost. Each simulation has different shine through losses depending on the initial energy. This losses take place because some neutrals from the NBI line may not be ionized and leave the plasma. Shine though losses should be minimized because they are a waste of energy and may cause damage to the reactor wall. Table 5.1 shows the fraction of neutrals that leave the plasma for each initial energy, which increases monotonically with the energy. They are, in all cases, smaller or equal than 3 % of the beam, so in this case they are not very relevant. In other device geometries,

Table 5.1	Shine through
losses for	each initial energy,
estimated	with FAFNER2

Energy	Shine through loss (%)
0.8 MeV	0.84
0.9 MeV	1.32
1.0 MeV	1.76
1.1 MeV	2.51
1.2 MeV	3.00

like perpendicular injection in LHD, shine though losses can be an important fraction of the NBI input power.

The energy (power) absorption profile is the fraction of energy (power) released by the NBI system at each magnetic surfaces. We use ISDEP to calculate the energy absorption or deposition profile. It is also possible to calculate the power deposition profile dividing by the time. Figure 5.11 shows these two profiles and the average energy and persistence of the test particle ensemble for each beam energy.

The slowing down time and the confinement time decrease monotonically with the energy of the beam, as can be deduced from the top panels of Fig. 5.11. The power deposition profile becomes more centered as the beam energy increases. So it is necessary to have a compromise between this two characteristics of the NBI absorption: decrease as much as possible the slowing down time and, on the other hand, have a centered power deposition profile.

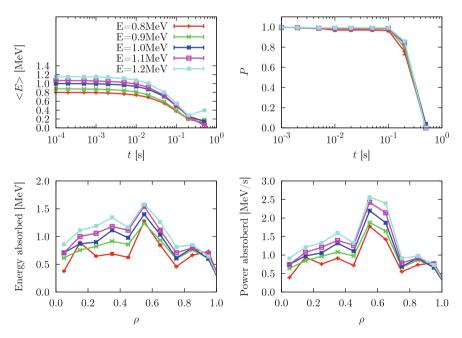


Fig. 5.11 Average energy (up, left), persistence (up, right), energy absorbed (down, left) and power absorber (down, right) for the NBI fast ions in ITER

5.4 Conclusions 109

5.4 Conclusions

We have calculated the NBI ion transport in ITER for a mono-energetic beam of $E_0 = 1 \,\text{MeV}$ in the banana regime. The main physical result is, as in Chap. 4, the steady state distribution function.

A important feature of the function is the appearance of oscillations of the function $f(E,\rho)$ with energy is the existence of maxima and minima in the region $\rho>0.75$. Zones with positive slopes in f(E) could create or increase kinetic instabilities which worsen the ion confinement. We have discarded that it is due to a numerical effect, but to the combined effect of collisions and electric field. Further investigation is needed to clarify and identify the trigger of this point.

The ion velocity profiles show that the radial velocity causes an accumulation of particles in the zone of the plasma around $\rho \in (0.5, 0.7)$. The toroidal velocity profile shows areas of inverted velocities at $\rho \sim 0.75$. The cause is the deterministic evolution of λ , due to the confining magnetic field.

The slowing down time is also calculated showing a separation of the Spitzer one caused by the banana orbits. This shows that this important quantity must be estimated carefully in the banana regime.

References

- 1. Hemsworth R et al (2009) Nucl Fusion 49:045006
- 2. Stix TH (1972) Plasma Phys 14:367
- 3. Goldston RJ, Rutherford PH (1995) Introduction to plasma physics. Taylor and Francis, London

Chapter 6 Overview and Conclusions

This PhD thesis report contains the research work done by the author with the ISDEP code in the context of kinetic theory of plasmas. Starting from a well-established version of ISDEP, we have improved the code and applied it to several realistic cases, like the 3D transport in ITER, the largest tokamak in the world, or the study of fast ions in the LHD and TJ-II stellarators. Finally, the code has been applied to NBI ion transport in ITER.

ISDEP can be classified in the Monte Carlo Orbit codes category. Although there are a number of codes which solve the same problem, ISDEP tries to avoid approximations and limitations that these codes usually present. The use of a full 3D spatial description of the system employing Cartesian coordinates, the lack of *a priori* conserved quantities and the detailed representation of the particle dynamics make ISDEP more realistic and flexible than many existing simulation codes. The most important features of ISDEP, from a physical point of view are:

- It calculates the test particle distribution function in a fusion device, considering the actual 3D geometry, collisions with several species and the static radial electric field.
- Test particles (usually ions) interact with a static plasma background via the Boozer and Kuo-Petravic collision operator.
- It makes use of the guiding center approximation, reducing the dimensionality of the system and getting rid of a small scale and fast gyromotion.
- Indeed, it takes into account the parallel movement and the drift velocities: $\mathbf{E} \times \mathbf{B}$, $\nabla B \times \mathbf{B}$ and $\mathbf{R}_C \times \mathbf{B}$.
- It uses Cartesian coordinates, allowing the description of the SOL region and any magnetic field topology.
- The particle movement is represented by a 5D stochastic differential equation system.
- ISDEP uses the Jack-Knife technique to analyze the Monte Carlo results and calculate the statistical errors.
- Due to its architecture, it has a very good performance in distributed computing platforms like grids and desktop grids.

The main improvements included in ISDEP during the elaboration of this thesis are, in chronological order:

- Inclusion of a test tokamak geometry, to benchmark the code with the MORH code.
- Inclusion of an H-mode ITER equilibrium and plasma profiles.
- A BOINC version of the code, used in the Ibercivis calculations.
- Inclusion of any LHD vacuum magnetic configuration, although only the one labeled with $R_{axis} = 3.60$ m is used in this thesis.
- The coupling between ISDEP and FAFNER2/HFREYA to obtain the fast ion initial distribution.
- The measurement of the distribution function $f(t, \rho, v_{||}, v_{\perp})$.
- Calculations of the steady state and NBI-Blip distribution functions, using Green's function formalism.
- Introduction of charge exchange and thermalization losses.
- Reconstruction of the CNPA neutral flux spectrum in TJ-II considering the geometry of the detector.

The numerical results obtained in this work can be divided in three groups: studies of the 3D transport in ITER geometry, calculation of the distribution function of fast ions in stellarators and comparison of the latter with experimental results.

The influence of the magnetic ripple on the ITER collisional transport has been studied as a first work in Chap. 3. These studies have shown the increase of the radial particle and energy fluxes and the deterioration of the confinement with the toroidal magnetic ripple. The conclusion is that the 3D geometry affects the transport in ITER and should be considered for detailed simulations of the device. Even though the modification is not extremely high, for long pulses or steady state operation it may have a strong influence on the behavior of the plasma.

Beyond the global confinement features, ISDEP is used to calculate other transport properties like the distribution of particle losses in this 3D geometry. With additional input data, ISDEP can provide the total fluxes that reach the device walls and can be used to optimize the divertor system and minimize sputtering and recycling.

The effect of the ripple is especially relevant for high energy ions because the $\nabla B \times \mathbf{B}$ and $\mathbf{R}_c \times \mathbf{B}$ drift velocities are proportional to the ion energy. Therefore we expect that the alpha particle confinement is affected in fusion D-T plasmas. Since alpha particles carry an important fraction of the fusion reactions energy and are supposed to heat the plasma, the studies presented here are relevant for future simulations in fusion devices. All these results were published in [1].

Later, the confinement properties of the NBI fast ions are studied for stellarators in Chap. 4 and published in [2]. The main result of this chapter is the calculation of the fast ion distribution function $f(\rho, v_{||}, v_{\perp})$, both time dependent and in the steady state. We have considered two different NBI cases: perpendicular injection for LHD and tangential for TJ-II. This is a more general result than those presented in Chap. 3 because the relevant quantities of the test particles can be estimated as moments of the distribution.

The steady state profiles of toroidal and poloidal rotation and radial velocity are calculated in this way. Since momentum conservation is not satisfied in ISDEP because the plasma background is static, the rotation profiles of the beam ions are not a precise measure of the whole plasma rotation, only an estimation of the NBI rotation and current drive. The calculation of poloidal rotation profiles is important because they may be able to create shear flows. Shear flows may help to reduce the turbulence and create transport barriers, improving the plasma global confinement [3].

Fast ion thermalization is a basic measurement of the NBI efficiency in the device. The slowing down time is computed and compared with the standard Neoclassical formula, showing the effect of the particular magnetic configuration and injection properties on such quantity. The ion transport and the device geometry happen to be a key factor in the slowing down process. The loss cones in the two devices are also estimated with ISDEP as functions of time, showing the different time scales of the loss processes. The slowing down time appears to be of the same order of the fast ion confinement time in the two cases.

With this numerical tool working we proceeded to compare the computational results with actual experimental data, mainly in TJ-II. The experimental data are provided, in both cases, by the Neutral Particle Analyzers (NPAs) installed in the machines. In TJ-II we have successfully reconstructed the CNPA energy spectra for two characteristic discharges with different plasma density. The agreement is satisfactory although some discrepancies are observed, mainly in the high energy region of the spectra. We have concluded that the discrepancies between simulation and experiment can be attributed to the Alfvén activity in TJ-II.

The NBI-Blip experiments in LHD have also been well reproduced by the code calculating the decay time in the $E>29\,\mathrm{keV}$ energy range, but only in a limited region of the plasma and for one magnetic configuration.

Finally, we have presented our results concerning NBI ion transport in the ITER geometry. We have calculated the characteristic confinement and thermalization times and have found a radial accumulation region located around $\rho=0.6$. The calculations also predicted an inversion of the NBI toroidal current in the outer regions of ITER and the appearance of several maxima and minima in the spectrum f(E). The former is due to the deterministic evolution of the pitch angle while the latter is cause by the combined action of collisions and radial transport. The onset of this non-monotonic distribution function could be a concern, since it might produce the appearance of kinetic instabilities.

Finally, the slowing down time is calculated and compared with the Spitzer estimation. The differences are due to the banana regime, which causes ion transport to be non-local.

On the whole, the ISDEP code has become a valuable simulation instrument for the study of collisional transport in fusion devices. But still there is a lot of work to do in the near future. Here we list a few research lines:

- Simulation of Ion Cyclotron Resonance Heating (ICRH) in ITER, scanning the antenna power and studying the heating efficiency. This task requires the inclusion of the quasi-linear wave-particle interaction equations [4] in ISDEP.
- Improving the comparison with the NBI-Blip discharges in LHD, using different magnetic configurations and plasma profiles.
- Include 3D effect of the fast ion transport in ITER in the same way as in Chap. 3.
- Study of the impurity effect in the NBI ions in TJ-II using a non flat Z_{eff} profile [5].
- Introduction of Alfvén wave effects on fast ion orbits.
- Calculations for the ASDEX-U tokamak and comparison with experiments [6, 7].

References

- Bustos A et al (2010) Nucl Fusion 50:125007
- 2. Bustos A et al (2011) Nucl Fusion 51:083040
- 3. Bigliari H, Diamond PH, Terry PW (1990) Phys Fluids B 2:1
- 4. Castejón F, Eguilior S (2003) Plasma Phys Controlled Fusion 45:159
- McCarthy K, Tribaldos V, Arévalo J Liniers M (2010) J Phys B Atomic Mol Opt Physi 43:144020
- Garcia-Munoz M, Fahrbach H, Zohm H (2009) and the ASDEX upgrade team. Rev Sci Instrum 80:053503
- 7. Garcia-Munoz M et al (2011) Nucl Fusion 51:103013

Appendix A Index of Abbreviations

BIFI Instituto de Biocomputación y Física de los Sistemas Complejos

BOINC Berkeley Open Infastructure of Network Computing

CIEMAT Centro de Investigaciones Energéticas, Medio-Ambientales y Tecnologicas

CNPA Compact neutral particle analyzer

CX Charge exchange DKE Drift kinetic equation

ECRH Electron cyclortron resonance heating

FP Fokker planck

HPC High performance computer ICRH Ion cyclortron resonance heating

ITER International tokamak experimental reactor

ISDEP Integrator of stochastic differential equations for plasmas

GC Guiding center
LHD Large helical device
LHS Left hand side
LOS Line of sight

NBI Neutal beam injection

NC Neoclassical

(C)NPA (Compact) neutral particle analyzer

MHD Magneto hydro dynamics
ODE Ordinary differential equation

RHS Right hand side

SDE Stochastic differential equation

SOL Scrape-off-layer TJ-II Tokamak JEN II

UCM Universidad Complutense de Madrid

Appendix B

Guiding Center Equations

In this appendix we work in detail the deduction of the Guiding Center equations of motion for a charged particle in a strong magnetic field.

B.1 Guiding Center Lagrangian

In this section we deduce the expression of the Guiding Center Lagrangian, which reduces the dimensionality of our system and deals with the gyromotion. The equations obtained here represent the movement of a charged particle in an external electromagnetic field where the dominant force is given by the magnetic component. The interaction of the particle with other plasma particles is shown in Sect. 1.3.2 we use the Einstein summation convention and we may denote partial derivatives with a comma subscript. As usual, the index rising and lowering is done with the metric tensor [1]. Let us start with the classical Lagrangian for a charged particle [2]:

$$\mathcal{L}(\mathbf{r}, \dot{\mathbf{r}}, t) = \frac{m\dot{\mathbf{r}}^2}{2} + Ze\mathbf{A}(\mathbf{r}, t) \cdot \dot{\mathbf{r}} - Ze\Phi(\mathbf{r}, t), \tag{B.1}$$

where m and Ze are the particle mass and charge; \mathbf{r} and $\dot{\mathbf{r}}$ the particle position and velocity; and \mathbf{A} and Φ the magnetic and electric potentials, with $\mathbf{B} = \nabla \times \mathbf{A}$, $\mathbf{E} = -\nabla \Phi - \frac{\partial \mathbf{A}}{\partial t}$. The particle equations of movement are given by the Euler-Lagrange equations:

$$\frac{\mathrm{d}}{\mathrm{d}t} \left(\frac{\partial \mathcal{L}}{\partial \dot{r}^i} \right) = \frac{\partial \mathcal{L}}{\partial r^i}.$$
 (B.2)

Then:

$$\frac{\mathrm{d}}{\mathrm{d}t}(m\dot{r}_i + ZeA_i) = ZeA_{j,i}\dot{r}^j - Ze\Phi_{,i} \Rightarrow \tag{B.3}$$

$$m\ddot{r}^{i} = Ze\left(A_{j}^{i}\dot{r}^{j} - \Phi^{,i} - \dot{A}^{i}\right). \tag{B.4}$$

In components, the magnetic field is $B^i = \epsilon^{ijk} A_{k,i}$, so:

$$(\mathbf{B} \times \dot{\mathbf{r}})^{i} = \epsilon^{i}_{jk} B^{j} \dot{r}^{k}$$

$$= \epsilon^{i}_{jk} \epsilon^{j}_{pq} A^{q,p} \dot{r}^{k}$$

$$= -\epsilon^{i}_{jk} \epsilon^{j}_{pq} A^{q,p} \dot{r}^{k}$$

$$= -(\delta^{i}_{p} \delta_{kq} - \delta^{i}_{q} \delta_{pk}) A^{q,p} \dot{r}^{k}$$

$$= A^{i}_{\nu} \dot{r}^{k} - A^{i}_{\nu} \dot{r}^{k}, \tag{B.5}$$

$$\Rightarrow A_j^{,i}\dot{r}^j = -\left(\mathbf{B}\times\dot{\mathbf{r}}\right)^i + A_{,k}^i\dot{r}^k. \tag{B.6}$$

With this:

$$m\ddot{r}^{i} = Ze\left(-\left(\mathbf{B} \times \dot{\mathbf{r}}\right)^{i} + A_{,k}^{i}\dot{r}^{k} - \Phi^{,i} - \dot{A}^{i}\right),\tag{B.7}$$

$$m\ddot{\mathbf{r}} = Ze\left(\dot{\mathbf{r}} \times \mathbf{B} + \mathbf{E}\right). \tag{B.8}$$

This is the classical Lorentz force for a charged particle. In particular, the solution of this second order ODE in a uniform magnetic field is:

$$\mathbf{r} = \mathbf{R} + \frac{1}{\Omega} \mathbf{b} \times \dot{\mathbf{r}}. \tag{B.9}$$

With: $\Omega = ZeB/m$, $\mathbf{b} = \mathbf{B}/B$ and \mathbf{R} the position of the center of rotation or GC position. The frequency Ω is known as the Larmor frequency and it is the rotation frequency of a charged particle of mass m and charge Ze moving in a uniform magnetic field. Moving to a coordinate system where $\mathbf{B} = B\mathbf{z}$, we define the Larmor radius $\vec{\rho}$:

$$\mathbf{R} = \mathbf{r} - \vec{\rho}, \quad \vec{\rho} = \rho \left(\hat{\mathbf{x}} \cos \theta + \hat{\mathbf{y}} \sin \theta \right), \quad \rho = \frac{\dot{r}_{\perp}}{\Omega},$$
 (B.10)

with \dot{r}_{\perp} being the velocity component perpendicular to \mathbf{B}, θ the rotation angle around \mathbf{R} , and $\hat{\mathbf{x}}$ and $\hat{\mathbf{y}}$ unitary vectors. Note than in this section, and only in this section, the Greek character ρ does not refer to the plasma effective radius but to the Larmor radius.

In order to get rid of the fast and small scale movement of gyration around **R**, the Guiding Center approach is introduced. It is assumed that the Larmor radius is much smaller than any other characteristic length of the system so the plasma parameters and fields do not vary much in one gyro-orbit. In such a case the 6D phase space can be reduced to a 5D phase space whose coordinates are **R**, the Guiding Center position, and two coordinates for velocity space, disregarding the gyroangle coordinate. In this approximation the zeroth order movement is given by the magnetic field lines. Electric field and inhomogeneities of the magnetic field give rise to the first order

correction: the *drift velocities*. With this procedure we can get rid of the fast gyration time scale ($\sim 10^8 \ Hz$) and the small spatial scale ($\sim 10^{-3} \ m$).

The procedure to reduce the dimensionality of the system is the following. First the Lagrangian is expanded in Taylor series around the Guiding Center position in the Larmor radius. Then we must average in the rotation angle or gyroangle θ around the field line. The gyroangle average is defined as:

$$\langle g(\theta) \rangle = \frac{1}{2\pi} \int_0^{2\pi} g(\theta) d\theta.$$
 (B.11)

We proceed in this way for each term in the Lagrangian from Eq. (B.1):

$$\langle \frac{m\dot{r}^{2}}{2} \rangle \approx \frac{m}{2} \langle (\dot{\mathbf{R}} + \dot{\bar{\rho}})^{2} \rangle$$

$$= \frac{m}{2} \langle \dot{R}^{2} + \dot{\rho}^{2} + 2\dot{\mathbf{R}} \cdot \dot{\bar{\rho}} \rangle$$

$$= \frac{m}{2} \left(\langle \dot{R}^{2} \rangle + (\rho \dot{\theta})^{2} \right)$$

$$= \frac{m}{2} \left((\dot{\mathbf{R}} \cdot \mathbf{b})^{2} + (\rho \dot{\theta})^{2} \right). \tag{B.12}$$

$$\langle \Phi(\mathbf{r}, t) \rangle \approx \Phi(\mathbf{R}, t). \tag{B.13}$$

$$\langle \mathbf{A}(\mathbf{r}, t) \cdot \dot{\mathbf{r}} \rangle \approx \langle \left(\mathbf{A}(\mathbf{R}) + \mathbf{A}_{,x}\rho\cos\theta + \mathbf{A}_{,y}\rho\sin\theta \right)$$

$$\cdot \left(\mathbf{R} + \rho \dot{\theta} \left(-\mathbf{x}\sin\theta + \mathbf{y}\cos\theta \right) \right) \rangle$$

$$= \mathbf{A}(\mathbf{R}) \cdot \mathbf{R} + \frac{\rho^{2}\dot{\theta}}{2} \left(A_{y,x} - A_{x,y} \right)$$

$$= \mathbf{A}(\mathbf{R}) \cdot \mathbf{R} + \frac{B\rho^{2}\dot{\theta}}{2}, \tag{B.14}$$

where we have made use of: $\vec{\rho} \cdot \mathbf{b} = \dot{\vec{\rho}} \cdot \mathbf{b} = 0$, $\langle \cos \theta \rangle = \langle \sin \theta \rangle = 0$ and $\langle \dot{\mathbf{R}}^2 \rangle = (\dot{\mathbf{R}} \cdot \mathbf{b})^2$.

With all the simplified terms, the GC Lagrangian is:

$$\mathcal{L}(\mathbf{R}, \rho, \theta, \dot{\mathbf{R}}, \dot{\rho}, \dot{\theta}, t) = \frac{m\dot{R}^2}{2} + \frac{m\rho^2\dot{\theta}^2}{2} + Ze\mathbf{A}(\mathbf{R}) \cdot \dot{\mathbf{R}} + \frac{Ze\rho^2\dot{\theta}^2}{2}B(\mathbf{R}) - Ze\Phi(\mathbf{R}).$$
(B.15)

Now let us calculate the Euler-Lagrange equations for ρ and θ . The equation for ρ is:

$$\frac{\mathrm{d}}{\mathrm{d}t} \left(\frac{\partial \mathcal{L}}{\partial \dot{\rho}} \right) = \frac{\partial \mathcal{L}}{\partial \rho}.$$
 (B.16)

$$\frac{\partial \mathcal{L}}{\partial \dot{\rho}} = 0 \Rightarrow m\rho \dot{\theta}^2 + Ze\rho \dot{\theta} B = 0, \tag{B.17}$$

$$\dot{\theta} = -\frac{ZeB}{m} = -\Omega. \tag{B.18}$$

This result is obvious, the particle rotates uniformly around the field line with frequency $\pm \Omega$, depending on the sign of the charge. The equation for the gyroangle implies that θ is a cyclic variable in \mathcal{L} , so a conserved quantity is obtained:

$$\frac{\partial \mathcal{L}}{\partial \theta} = 0 \Rightarrow \frac{\mathrm{d}}{\mathrm{d}t} \left(\frac{\partial \mathcal{L}}{\partial \dot{\theta}} \right) = \frac{\mathrm{d}p_{\theta}}{\mathrm{d}t} = 0. \tag{B.19}$$

Then $\rho^2 \Omega = C$, constant, $\rightarrow v_{\perp}^2/\Omega = C$. We call this constant of motion the magnetic moment and, using the definition of Ω :

$$\mu = \frac{mv_{\perp}^2}{2B}.\tag{B.20}$$

We will see later that this conserved quantity is necessary to find the evolution equations in velocity space. Finally, the equations for the G.C. coordinates are:

$$\frac{\mathrm{d}}{\mathrm{d}t} \left(\frac{\partial \mathcal{L}}{\partial \dot{R}^i} \right) = \frac{\partial \mathcal{L}}{\partial R^i}.$$
 (B.21)

Ignoring the terms in the Lagrangian that do not depend on \mathbf{R} or $\dot{\mathbf{R}}$ (irrelevant for the present purposes), we get

$$\mathcal{L}(\mathbf{R}, \dot{\mathbf{R}}, t) = \frac{m}{2} \left(\mathbf{b}(\mathbf{R}) \cdot \dot{\mathbf{R}} \right)^2 + Ze\mathbf{A}(\mathbf{R}) \cdot \dot{\mathbf{R}} + \mu B(\mathbf{R}) - Ze\Phi(\mathbf{R}).$$
 (B.22)

Naming $v_{||} = \dot{\mathbf{R}} \cdot \mathbf{b}$, the LHS of Eq. (B.21) is:

$$\frac{\mathrm{d}}{\mathrm{d}t} \left(\frac{\partial \mathcal{L}}{\partial \dot{\mathbf{R}}} \right) = \left(\frac{\partial}{\partial t} + \dot{\mathbf{R}} \cdot \nabla \right) \left(m(\mathbf{b} \cdot \dot{\mathbf{R}}) \mathbf{b} + Ze\mathbf{A} \right)$$

$$= m\dot{v}_{||} \mathbf{b} + mv_{||} \left(\frac{\partial}{\partial t} + \dot{\mathbf{R}} \cdot \nabla \right) \mathbf{b}$$

$$+ Ze \frac{\partial \mathbf{A}}{\partial t} + Ze(\dot{\mathbf{R}} \cdot \nabla) \mathbf{A}.$$
(B.23)

Using the vector identity $\nabla(\mathbf{C} \cdot \mathbf{X}) = (\mathbf{C} \cdot \nabla)\mathbf{X} + \mathbf{C} \times (\nabla \times \mathbf{X})$, valid for a constant vector \mathbf{C} , we find:

$$(\dot{\mathbf{R}} \cdot \nabla)\mathbf{A} = \nabla(\dot{\mathbf{R}} \cdot \mathbf{A}) - \dot{\mathbf{R}} \times (\nabla \times \mathbf{A}) = \nabla(\dot{\mathbf{R}} \cdot \mathbf{A}) - \dot{\mathbf{R}} \times \mathbf{B}, \tag{B.24}$$

the RHS of Eq. (B.21) leads to:

$$\frac{\partial \mathcal{L}}{\partial \mathbf{R}} = mv_{||} \nabla (\mathbf{b} \cdot \dot{\mathbf{R}}) + Ze \nabla (\mathbf{A} \cdot \dot{\mathbf{R}}) + \nabla (\mu B) - Ze \nabla \Phi
= mv_{||} \left((\dot{\mathbf{R}} \cdot \nabla) \mathbf{b} + \dot{\mathbf{R}} \times (\nabla \times \mathbf{b}) \right)
+ Ze \left((\dot{\mathbf{R}} \cdot \nabla) \mathbf{A} + \dot{\mathbf{R}} \times \dot{\mathbf{B}} \right) - \mu \nabla B - Ze \nabla \Phi.$$
(B.25)

Adding up both equations, the terms with $\nabla(\dot{\mathbf{R}} \cdot \mathbf{A})$ and $(\dot{\mathbf{R}} \cdot \nabla)\mathbf{b}$ cancel out. Then, the equation for the GC position becomes:

$$m\dot{v}_{||}\mathbf{b} = -mv_{||}\frac{\partial \mathbf{b}}{\partial t} + Ze(\mathbf{E} + \dot{\mathbf{R}} \times \mathbf{B}) + mv_{||}(\dot{\mathbf{R}} \times (\nabla \times \mathbf{b})) - \mu\nabla B. \quad (B.26)$$

It is assumed that $\frac{\partial \mathbf{b}}{\partial t} = 0$ or that is very small compared with Ω and is neglected. The triple cross product term may be simplified introducing the curvature of the magnetic field lines: $\vec{k} = (\mathbf{b} \cdot \nabla)\mathbf{b}$.

$$\dot{\mathbf{R}} \times (\nabla \times \mathbf{b}) = v_{||} \mathbf{b} \times (\nabla \times \mathbf{b}). \tag{B.27}$$

$$\nabla (\mathbf{b} \cdot \mathbf{b}) = 0 \Rightarrow \mathbf{b} \times (\nabla \times \mathbf{b}) + (\mathbf{b} \cdot \nabla)\mathbf{b} = 0.$$
 (B.28)

$$\mathbf{b} \times (\nabla \times \mathbf{b}) = -(\mathbf{b} \cdot \nabla)\mathbf{b} = -\vec{\kappa}. \tag{B.29}$$

Finally:

$$m\dot{v}_{||}\mathbf{b} = Ze(\mathbf{E} + \dot{\mathbf{R}} \times \mathbf{B}) - \mu \nabla B - mv_{||}^2 \vec{\kappa}.$$
 (B.30)

If we do the scalar product with **b**, we can obtain the parallel dynamics of the GC:

$$m\dot{v}_{||} = ZeE_{||} - \mu\nabla_{||}B. \tag{B.31}$$

The two terms in this equation represent the influence of the electric field and the magnetic mirrors on the dynamics along a field line. We may perform the cross product with $\bf b$ to obtain perpendicular dynamics. Usually the perpendicular component of the GC velocity is called *drift velocity*, $\bf v_D$:

$$0 = -ZeB\mathbf{v}_{D} + Ze\mathbf{E} \times \mathbf{b} - \mu \nabla B \times \mathbf{b} - mv_{\parallel}^{2} \vec{k} \times \mathbf{b}. \tag{B.32}$$

$$\mathbf{v}_{\mathrm{D}} = \frac{\mathbf{E} \times \mathbf{B}}{R^{2}} + \frac{v_{\perp}^{2}}{2\Omega} \mathbf{b} \times \nabla \ln B + \frac{v_{\parallel}^{2}}{\Omega} \mathbf{b} \times \vec{\kappa}. \tag{B.33}$$

Usually the drift velocity is expressed in terms of the curvature radius of the magnetic field lines \mathbf{R}_c instead of the curvature itself:

$$\frac{\mathbf{R}_c}{R_c^2} = \vec{\kappa}.\tag{B.34}$$

Table 1.1 in Sect. 1 shows the notation used in this thesis for the physical quantities.

B.2 Higher Order Corrections in the Electric Field

It is possible to obtain more accurate GC equations of motion retaining more therms in the Taylor expansion in $\vec{\rho}$ around the GC position Eqs. (B.14) and (B.13). This is necessary when the Larmor radius is not sufficiently small compared with the other lengths of the system. Although ISDEP is limited to the first order, we illustrate this method obtaining higher order corrections in the electrostatic field.

The order zero expansion is $\langle \Phi(\mathbf{r}, t) \rangle^0 = \Phi(\mathbf{R})$. The order one correction is zero because it is proportional to $\cos \theta$ or $\sin \theta$, whose average in θ is zero: $\langle \Phi(\mathbf{r}, t) \rangle^1 = 0$. In the second order Taylor expansion we can find terms proportional to $\cos^2 \theta$ or $\sin^2 \theta$. The only surviving terms after gyroangle average are:

$$\langle \Phi(\mathbf{r}, t) \rangle^2 = \frac{\rho^2}{4} \left(\frac{\partial^2 \Phi}{\partial x^2} + \frac{\partial^2 \Phi}{\partial y^2} \right)$$
$$= \frac{\rho^2}{4} \nabla^2 \Phi(\mathbf{R}). \tag{B.35}$$

The the electric potential is, up to the second order:

$$\Phi(\mathbf{r}) \approx \Phi(\mathbf{R}) + \frac{\rho^2}{4} \nabla^2 \Phi(\mathbf{R}).$$
(B.36)

This substitution should be done when the electric field is intense or when the Larmor radius is not small compared with $\Phi/|\nabla\Phi|$. Usually this correction is not required, but the procedure can be applied to any term in the Lagrangian if needed.

B.3 Explicit Equations for Tokamaks and Stellarators

In this section we present the GC equations for the two most advanced kinds of fusion devices: tokamaks and stellarators. A description of the geometry and coil distribution of these devices can be found in Sects. 3 and 4. The important feature on account to the equations of movement is the terms with $\nabla \times \mathbf{B}$, which can be neglected in a stellarator in contrast to the tokamak case, where the electric current can be important.

The most general case in GC dynamics for fusion plasmas is the **tokamak** (see Sect. 3.1). None of the terms in the parallel and drift velocities are negligible due to the coil configuration, the plasma characteristics and the geometry. Equations B.31 and B.33 read:

$$\frac{\mathrm{d}\mathbf{r}}{\mathrm{d}t} = v\lambda \frac{\mathbf{B}}{B} + \frac{mv^2(1-\lambda^2)}{eB^3} \left(\mathbf{B} \cdot (\nabla \times \hat{\mathbf{b}}) \right) \cdot \mathbf{B} + \mathbf{v}_D = \mathbf{v}. \tag{B.37}$$

$$\mathbf{v}_{D} = \frac{\mathbf{E} \times \mathbf{B}}{B^{2}} + \frac{mv^{2}}{2eB^{3}}(1 - \lambda^{2})\left(\mathbf{B} \times \nabla B\right) + \frac{mv^{2}\lambda^{2}}{eB^{2}}\left(\frac{\mathbf{B} \times \mathbf{R}_{c}}{R_{c}^{2}}\right). \tag{B.38}$$

Let us derive the equations for v^2 and λ from the energy and magnetic moment conservation in the absence of collisions with the background plasma. The energy conservation is expressed as:

$$\frac{\mathrm{d}E}{\mathrm{d}t} = 0, \qquad E = \frac{mv^2}{2} + e\Phi. \tag{B.39}$$

Then the equation for dv^2/dt is obtained:

$$\frac{\mathrm{d}v^2}{\mathrm{d}t} = -\frac{2e}{m}\frac{\mathrm{d}\Phi}{\mathrm{d}t} = -\frac{2e}{m}\left(\nabla\Phi\frac{\mathrm{d}\mathbf{r}}{\mathrm{d}t}\right) = \frac{2e}{m}\mathbf{E}\cdot\mathbf{v}.$$
 (B.40)

The pitch angle evolution $d\lambda/dt$ can be deduced in the same way using the conservation of $\mu = m(1 - \lambda^2)v^2/2B$:

$$\frac{\mathrm{d}\mu}{\mathrm{d}t} = 0 \Rightarrow \frac{m(1-\lambda^2)}{2B} \frac{\mathrm{d}v^2}{\mathrm{d}t} - \frac{2\lambda mv^2}{2B} \frac{\mathrm{d}\lambda}{\mathrm{d}t} - \frac{\mu}{B} \left(\nabla B \cdot \mathbf{v}\right) = 0. \tag{B.41}$$

Hence

$$\frac{\mathrm{d}\lambda}{\mathrm{d}t} = \frac{2B}{2\lambda m v^2} \left(\frac{m(1-\lambda^2)}{2B} \frac{\mathrm{d}v^2}{\mathrm{d}t} - \frac{\mu(\nabla B \cdot \mathbf{v})}{B} \right)
= \frac{(1-\lambda^2)}{2\lambda v^2} \frac{\mathrm{d}v^2}{\mathrm{d}t} - \frac{mv^2(1-\lambda^2)}{2B\lambda m v^2} (\nabla B \cdot \mathbf{v})
= \frac{(1-\lambda^2)}{2\lambda v^2} \frac{\mathrm{d}v^2}{\mathrm{d}t} - \frac{(1-\lambda^2)}{2B\lambda} (\nabla B \cdot \mathbf{v}).$$
(B.42)

This expression is mathematically correct, but λ 's in the denominator cause numerical instabilities when $\lambda \approx 0$. A more stable formula can be obtained recalling Eq. (B.40) and using the decomposition $\mathbf{v} = \mathbf{v}_{\parallel} + \mathbf{v}_{D}$.

$$\frac{\mathrm{d}\lambda}{\mathrm{d}t} = \frac{1 - \lambda^{2}}{2\lambda v^{2}} \frac{2e}{m} \left(\mathbf{E} \cdot (\mathbf{v}_{||} + \mathbf{v}_{D}) \right) - \frac{1 - \lambda^{2}}{2B\lambda} \left(\nabla B \cdot (\mathbf{v}_{||} + \mathbf{v}_{D}) \right) =
= \frac{1 - \lambda^{2}}{2\lambda} \left(2 \frac{e \mathbf{E} \cdot \mathbf{v}_{||}}{m v^{2}} + 2 \frac{1 - \lambda^{2}}{2B^{3}} \mathbf{E} \cdot (\mathbf{B} \times \nabla B) + 2 \frac{\lambda^{2}}{B^{2}} \mathbf{E} \cdot \left(\frac{\mathbf{B} \times \mathbf{R}_{c}}{R_{c}^{2}} \right)
- \frac{\nabla B \cdot \mathbf{v}_{||}}{B} - \frac{\nabla B \cdot (\mathbf{E} \times \mathbf{B})}{B^{3}} - \frac{m v^{2} \lambda^{2}}{e B^{3}} \nabla B \cdot \left(\frac{\mathbf{B} \times \mathbf{R}_{c}}{R_{c}^{2}} \right) \right).$$
(B.43)

We can get rid of λ in the denominator using that

$$\frac{\mathbf{E} \cdot \mathbf{v}_{||}}{\lambda} = E_{||}v, \qquad \frac{\nabla B \cdot \mathbf{v}_{||}}{\lambda} = \nabla B_{||}v, \tag{B.44}$$

and with some more simplification we get:

$$\frac{\mathrm{d}\lambda}{\mathrm{d}t} = \frac{1 - \lambda^{2}}{2} \left(\frac{2e}{mv} E_{||} - \frac{\lambda}{B^{3}} \mathbf{E} \cdot (\mathbf{B} \times \nabla B) + \frac{2\lambda}{B^{2}} \mathbf{E} \cdot \left(\frac{\mathbf{B} \times \mathbf{R}_{c}}{R_{c}^{2}} \right) - \frac{v}{B} (\nabla B)_{||} - \frac{m\lambda v^{2}}{eB^{3}} \nabla B \left(\frac{\mathbf{B} \times \mathbf{R}_{c}}{R_{c}^{2}} \right) \right). \tag{B.45}$$

Stellarators (see Sect. 4.1) are fusion devices in which almost all the magnetic field is created by external coils. Usually the plasma current is neglected so $\nabla \times \mathbf{B} = \mathbf{0}$. The previous orbit equations can be simplified to:

$$\frac{\mathrm{d}\mathbf{r}}{\mathrm{d}t} = v\lambda \frac{\mathbf{B}}{B} + \mathbf{v}_D,\tag{B.46}$$

$$\frac{\mathrm{d}v^2}{\mathrm{d}t} = \frac{2e}{m} \left(\mathbf{E} \cdot \mathbf{v}_D \right),\tag{B.47}$$

$$\frac{\mathrm{d}\lambda}{\mathrm{d}t} = -\frac{\mu}{mv} (\nabla B)_{||} - \frac{e\lambda}{mv^2} (\mathbf{E} \cdot \mathbf{v}_D) + \lambda \frac{(\mathbf{B} \times \nabla B) \cdot \mathbf{E}}{B^3}, \quad (B.48)$$

where

$$\mathbf{v}_D = \frac{\mathbf{E} \times \mathbf{B}}{B^2} + \frac{mv^2}{2eB^3} (1 + \lambda^2) \left(\mathbf{B} \times \nabla B \right). \tag{B.49}$$

It can be easily checked that energy and magnetic moment conservation are satisfied:

$$\frac{\mathrm{d}E}{\mathrm{d}t} = \frac{\mathrm{d}}{\mathrm{d}t} \left(\frac{mv^2}{2} + e\Phi \right) = e(\mathbf{E} \cdot \mathbf{v}_D) - \mathbf{E}e(\mathbf{v}_{||} + \mathbf{v}_D) = 0, \tag{B.50}$$

$$\frac{\mathrm{d}\mu}{\mathrm{d}t} = 0. \tag{B.51}$$

The energy conservation is valid as long as the electric field is perpendicular to the magnetic field. Usually the electric potential is constant on a flux surface (neglecting toroidal and poloidal asymmetries). So its gradient is perpendicular to the magnetic surface and, thus, to the magnetic field.

References

- 1. Hazeltine RD, Meiss JD (2003) Plasma confinement. Dover Publications, USA
- Helander P, Sigmar DJ (2001) Collisional transport in magnetized plasmas. Cambridge University Press, Cambridge

Personal Information

• Full name: Andrés de Bustos Molina

• Citzenship: Spanish

• Date of Birth: 6-June-1982

• email: andres.bustos@gmail.com

Academic Data

- March 2012—present day. Postdoctoral position at the Max Planck Institute fuer Plasmaphysik, Garching bei Muenchen, Germany. TOK division, Frank Jenko's group.
- February 2012—PhD in Physics at Complutense University, Madrid: *Kinetic Simulations of Ion Transport in Fusion Devices*. Qualification: Sobresaliente Cum Laude por unanimidad. Supervisors: Francisco Castejón Magana (CIEMAT) and Víctor Martin-Mayor (Departamento de Física Teórica I, Complutense University, Madrid).
- October 06'—June 07'. Master in Fundamental Physics by Complutense University (UCM), Madrid. Modules: High Energy Physics, Complex systems and Mathematical Physics. Master thesis: Aplicaciones del Cálculo Estocástico al Calentamiento Iónico en Plasmas de Fusión (Applications of Stochastic Analysis to Ion Heating in Fusion Plasmas). Supervisors: Luis Antonio Fernández Pérez and Víctor Martin-Mayor, Dep. of Theoretical Physics I, UCM. Final average mark: 9.66/10.
- October 06'—Dec. 06'. BIFI's (Institute for Biocomputation and Physics of the Complex Systems, Zaragoza, Spain. http://www.bifi.unizar.es) Young Researchers Grant.
- June 06'. Physics degree, UCM. Orientation: Fundamental Physics. Average mark: 2.55
- October 05'—June 06'. Collaboration grant in the Theoretical Physics Department, UCM.

 June 06'. Undergraduate Thesis: Ecuaciones de Langevin en Plasmas Confinados Magnéticamente (Langevin Equations in Magnetic Confined Plasmas). Supervisors: Luis Antonio Fernández Pérez and Víctor Martin-Mayor, Dep. of Theoretial Physics I, UCM.

- April 05'. Undergraduate Thesis: Ultra High Energy Cosmic Rays: the GZK cutoff.
 Supervisor: Konstantin Zarembo, Dept. of Theoretical Physics, Uppsala University, Sweden.
- June 2000: Secondary School Graduation in the Cardenal Cisneros High School, Madrid. Average Mark: 9.6/10 (Graduated with Honors).
- Student Grant by the Fundaciones César Rodríguez y Ramón Areces in the years: 1998, 1999, 2000, 2003, 2004 and 2005.

Scientific Publications

- A. Bustos, J. M. Fontdecaba, F. Castejón, J. L. Velasco, M. Tereschenko, J. Arévalo, Studies of the Fast Ion Energy Spectra in TJ-II, Physics of Plasmas 20, 022507 (2013).
- J. L. Velasco, A. Bustos, F. Castejón, L. A. Fernández, V. Martin-Mayor, A.Tarancón, ISDEP: Integrator of Stochastic Differental Equations for Plasmas, Computer Physics Communications 183, (2012).
- J. Sánchez et al, Overview of TJ-II experiments, Nucl. Fusion 51, 94022 (2011).
- A. Bustos, F. Castejón, M. Osakabe, L. A. Fernández, V. Martin-Mayor, J. L. Velasco, J. M. Fontdecaba, *Kinetic Simulations of Fast Ions in Stellarators*, Nuclear Fusion **51**, 83040 (2011).
- R. Jiménez-Gómez, A. Koenies, E. Ascasíbar, F. Castejón, T. Estrada, L. G. Eliseev,
 A. V. Melnikov, J. A. Jiménez, D. G. Pretty, D. Jiménez-Rey, M. A. Pedrosa,
 A. de Bustos, S. Yamamoto, *Alfvén eigenmodes measured in the TJ-II stellarator*,
 Nuclear Fusion 51, 033001 (2011).
- A. Bustos, F. Castejón, L. A. Fernández, J. García, V. Martin-Mayor, J. M. Reynolds, R. Seki and J. L. Velasco, *Impact of 3D features on ion collisional transport in ITER*, Nuclear Fusion 50, 125007 (2010).
- J. Sánchez et al, Confinement transitions in TJ-II under Li-coated wall conditions, Nucl. Fusion 49, 10 (2009).
- T. Happel, T. Estrada, E. Blanco, V. Tribaldos, A. Cappa, and A. Bustos, *Doppler reflectometer system in the stellarator TJ-II*, Rev. Sci. Instrum. **80**, 073502 (2009)
- F. Castejón, A. Gómez-Iglesias, A. Bustos, I. Campos, Á. Cappa, M. Cárdenas, L. A. Fernández, L. A. Flores, J. Guasp, E. Huedo, D. López-Bruna, I. M. Llorente, V. Martin-Mayor, R. Mayo, R. S. Montero, E. Montes, J. M. Reynolds, M. Rodríguez, A. J. Rubio-Montero, A. Tarancón, M. Tereshchenko, J. L. Vázquez-Poletti, J. L. Velasco, IBERGRID Proceedings. Santa Cristina: NETBIBLO S.L., 2009. Vol. 3, pp. 291-302. ISBN: 9788497454063.

Contribution to Conferences

• Studies of the Fast Ion Energy Spectra in TJ-II, A. Bustos, J.M. Fontdecaba, F. Castejón, J. L. Velasco and M. Tereshchenko, 33nd Bienal de la RSEF, September 2011, Santander, Spain.

- More efficient executions of Monte Carlo Fusion codes by means of Montera: the ISDEP use case, M. Rodríguez-Pascual, A.J. Rubio-Montero, R. Mayo, I. M. Llorente, A. Bustos, F. Castejón, PDP 2011 - The 19th Euromicro International Conference on Parallel, Distributed and Network-Based Computing, February 2011, Cyprus.
- Kinetic simulations of fast ions in stellarators, A. Bustos, F. Castejón, L.A. Fernández, V. Martin-Mayor, M. Osakabe. V National BIFI Conference, February 2011, Zaragoza, Spain.
- Kinetic simulations of fast ions in stellarators, A. Bustos, F. Castejón, L.A. Fernández, V. Martin-Mayor, M. Osakabe. 23rd IAEA Fusion Conference, October 2010, Daejon, Republic of Korea.
- Fast Ion simulations in Stellarators, A. Bustos, F. Castejón, L.A. Fernández, V. Martin-Mayor, M. Osakabe. 37th EPS Conference, June 2010, Dublin, Ireland.
- *ISDEP, a fusion application deployed in the EDGeS project*, A. Rivero, A. Bustos, A. Marosi, D. Ferrer, F. Serrano. 3rd AlmereGrid Grid Experience Workshop and 4th EDGeS Grid training event and Annual Gridforum.nl meeting, March 2010, Almere, The Netherlands.
- Fast Ion simulations in LHD, A. Bustos, F. Castejón, L.A. Fernández, V. Martin-Mayor, M. Osakabe. 19th Toki International Conference, 8-11th December 2009, Toki, Gifu, Japan.
- Comparison between 2D and 3D transport in ITER using a Citizen Supercomputer, A. Bustos, F. Castejón, L.A. Fernández, V. Martin-Mayor, A. Tarancón, J.L. Velasco. Oral contribution to the 32nd Bienal de la RSEF, September 2009, Ciudad Real, Spain.
- Comparison between 2D and 3D transport in ITER using a Citizen Supercomputer, A. Bustos, F. Castejón, L.A. Fernández, V. Martin-Mayor, A. Tarancón, J.L. Velasco. 36th EPS Conference, 29th June 3rd July 2009, Sofia, Bulgaria.
- Grid Computing for Fusion Research, F. Castejón, A. Gómez-Iglesias, A. Bustos, I. Campos, Á. Cappa, Cárdenas-Montes, L. A. Fernández, L. A. Flores, J. Guasp, E. Huedo, D. López-Bruna, I.M. Llorente, V. Martin-Mayor, R. Mayo, R.S. Montero, E. Montes, J. M. Reynolds, M. Rodríguez, A.J. Rubio-Montero, A. Tarancón, M. Tereshchenko, J. L. Vázquez-Poletti and J. L. Velasco. Ibergrid Meeting, May 2009, Valencia, Spain.
- Kinetic simulation of heating and collisional transport in a 3D tokamak, A. Bustos, F. Castejón, L.A. Fernández, V. Martin-Mayor, A. Tarancón, J.L. Velasco. 18th Toki International Conference, 9-12th December 2008, Toki, Gifu, Japan.
- Kinetic simulation of heating and collisional transport in a 3D tokamak, A. Bustos, F. Castejón, L.A. Fernández, V. Martin-Mayor, A.Tarancón, J.L. Velasco. 22nd IAEA Conference, 13-18th October 2008, Geneva, Switzerland.

 Kinetic simulation of heating and collisional transport in a 3D tokamak, A. Bustos, F. Castejón, L.A. Fernández, V. Martin-Mayor, A. Tarancón, J.L. Velasco. 35th EPS Conference, June 2008, Crete, Greece.

• *Kinetic simulation of heating and collisional transport in a 3D tokamak*, A. Bustos, F. Castejón, L.A. Fernández, V. Martin-Mayor, A.Tarancón, J.L. Velasco. Third BIFI International Congress, 6-8th February 2008, Zaragoza, Spain.

Participation in Projects

ISDEP has been involved in several national and international research projects. Besides being part of a long term series of projects focused in plasma kinetic theory at CIEMAT, it has been used in Computing Science projects as a test code for grid infrastructures. All these projects are summarized as follows:

• Project name: Proyecto TJ-II

Project leader: Joaquín Sánchez Sanz (CIEMAT)

Duration: 1986-2012

• Project name: Fusion-GRID (EGEE-III (NA4))

Project leader: Bob Jones (CERN)

Fusion coordinator: Francisco Castejón (CIEMAT)

Duration: 1-1-2008-31-12-2009

• Project name: EUFORIA

Project leader: Par Strand (Chalmers, Sweeden) JRA1 leader (Grid Codes): Francisco Castejón

Duration: 1-2008–31-12-2010
• Project name: EGI-Inspire

Project leader: Steven Newhouse (EGI)

Fusion coordinator: Francisco Castejón (CIEMAT)

Duration: 1-1-2011-31-12-2014

• Project name: Métodos Cinéticos en Plasmas de Fusión, #ENE2008-06082

Project leader: Francisco Castejón Duration: 1-1-2009–31-12-2011

• Project name: Complejidad en Materiales y Fenómenos de Transporte, #FIS2006-

08533-C03-01.

Project leader: Víctor Martín Mayor.

Duration: 2007-2009.

• Project name: Simulación y Modelización de Materiales Complejos, #FIS2009-

12648-C03-01

Project leader: Víctor Martín Mayor.

Duration: 2010-2012.